Infinity Jet

AIAA Aircraft Design Competition

2024-2025

LIÈGE université
Sciences Appliquées

AIAA
SHAPING THE FUTURE OF AEROSPACE

INFINITY TEAM

Name	AIAA N°	Photo	Signature
AZOUAR Mohamed	1763121		
BULON Luca	1763044		
COLSON Téo	1773288		
DELREE Clément	1773274		
OGER Basile	1762539		

FACULTY MEMBERS

Professors	Assistants
ANDRIANNE Thomas	BUDO Arnaud
NOELS Ludovic	DECHAMPS Paul

Contents

The Infinity Jet

MTOW

= 113 881 lb

Cruise speed

= Mach 0.9

L/D

= 18.2

Range max

= 9455 nmi

Take off distance

= 4194 ft

Landing distance

= 3573 ft

Passengers = 8

Crew = 3

Price

= 5515.22 $ per hour

Introduction

The ultra premium private aviation industry has undergone a notable transformation over the past decade, driven by a growing demand for ultra premium business jets that offer not only fast and efficient transport but also luxury, prestige, and business success. Modern business travelers now expect their jets to act as mobile offices as well as space for relaxation, requiring configurations integrating conference rooms, lounges and rest areas. In addition to this, customers also expect state-of-the-art aircraft with the best performance on the market, enabling them to save as much time as possible on their journeys. As a result, the private aviation sector is increasingly embracing cutting-edge engineering, pushing the boundaries of what is technically and commercially possible.

It is in this demanding and increasingly technical landscape that the American Institute of Aeronautics and Astronautics (AIAA) proposed a new design challenge: to develop a next-generation ultra premium business jet capable of both short and long range missions [5]. The challenge calls for a jet that not only meets the highest expectations in range and cruise speed but also introduces innovation in terms of space utilization, fuel efficiency and overall mission versatility. The *Infinity Jet* team responded with a bold concept featuring a high-aspect-ratio, high-wing configuration powered by high bypass ratio engines. This design aims to deliver competitive performance, reduced fuel consumption, and unmatched cabin volume, while raising the standards of luxury and functionality in the premium jet market. With these innovations, the team has developed an aircraft capable of fulfilling the required missions at a constant cruise speed of Mach 0.9.

Market analysis

The global market for business jets continues to grow, driven by increasing demand for flexibility, luxury and fast mobility. According to industry data, the business jet market is segmented into:

- Light and mid-size jets such as Cessna Citation CJ3+ or Embraer Phenom 100EV, for short regional travel [47, 49].
- Long-range and ultra-long-range jets such as the Global 7500 or the Gulfstream G700, targeting intercontinental travel with larger cabins and commodities [45, 50].
- Converted airliners such as Boeing Business Jet for clients prioritizing space and prestige over the rest [44].

The focus is on the ultra-premium business jet segment, positioned just below converted airliners. The design combines high performance and comfort, while innovating by creating a unique model in today's market.

However, despite their prestige, the current ultra-long-range jets show limitations in a world where clients increasingly seek both speed and utility. Most top business jets today offer either range or comfort, but rarely both in a balanced configuration. In addition, maximum cruise speeds and range capabilities remain relatively low for aircraft in these price segments as highlighted in Tab. 0.0.1. In a hyper connected world where executives may want to hold meetings or finalize deals in flight, performance and versatility are more critical than ever. Today's business aviation clients are no longer satisfied with just transportation. Their expectations have shifted toward a more complete flight experience, mixing luxury, comfort and productivity. The *Infinity jet* positions itself as a direct response to this market need by offering:

- Cabin flexibility, enabling business and relaxation on the same plane.
- High speed cruise, around Mach 0.9, across all mission profiles.
- Long-range capabilities reaching 8000 nmi.
- Reduced fuel consumption.

And it is in this absence of a solution in the market that *Infinity jet* finds its place for its development. A jet mixing luxury, comfort and productivity.

Aircraft	Mach (-)	Max range (nmi)	MTOW (lb)
Global 7500 Bombardier	0.85	7700	106 250
Gulfstream G700	0.85	7750	107 600
BBJ1	0.78	6200	171 000

Table 0.0.1: Main performance characteristics of competing aircraft.

1 Mission analysis

The *Infinity Jet* aims to offer an ultra-premium experience combining performance with comfort while reducing fuel consumption. Designed to accommodate up to 8 passengers and 3 flight crew members, the cabin includes ample space to accommodate passengers while maintaining superior short-and long- range performance compared to current competitors.

The aircraft is scheduled to enter service in 2031 and will be fully compliant with FAA 14 CFR Part 25 certification requirements [1]. The Infinity Jet has been developed to fulfill three core mission profiles, summarized in Tab. 1.0.1.

Requirements	Design Passenger Mission	Aspen Economic Mission	Napa Economic Mission
Passengers	8	4	8
Passenger weight	215 lb	215 lb	215 lb
Baggage/passenger	50 lb	100 lb	50 lb
Additional weight	/	/	480 lb
Range	8,000 nmi	700 nmi	1,700 nmi
Departure airport altitude	Sea level	800 ft	Sea level
Takeoff runway	6,000 ft	8,000 ft	5,930 ft
Takeoff temperature conditions	Sea level T	59°F	75°F
Arrival airport altitude	Sea level	7,800 ft	7,300 ft
Landing runway	6,000 ft	8,006 ft	12,966 ft
Landing temperature conditions	Sea level T	59°F	85°F

Table 1.0.1: Summary of the main requirements for the three missions requested by AIAA [5, 4, 3, 52, 51].

By analyzing the various mission profiles in Tab. 1.0.1, it is clear that the *Infinity Jet* must be capable of operating under a wide range of conditions from extreme temperatures (hot and cold) to varying payload and runway constraints. The aircraft has been developed with this versatility in mind and successfully meets the requirements of three representative mission types:

- **Standard Long-Range Mission**: The *Infinity Jet* is capable of flying a range of 8590.36 nmi at Maximum Take-Off Weight (MTOW), with a takeoff distance of 4175 ft and a landing distance of 4193.7 ft validating and even outperforming the mission requirements.
- **Napa Economic Mission**: In this demanding scenario involving high temperatures and increased payload, the *Infinity Jet* demonstrates its robustness by successfully covering the required range of 1700 nmi and being able to take off and land in the required distance.
- **Aspen Economic Mission:** The *Infinity Jet* fulfills the mission requirements by successfully covering the 700 nmi distance and operating within the required takeoff and landing distances. However, some discussion regarding the runway width is necessary and is presented below.

It is important to note that the wingspan of the *Infinity Jet* exceeds the current maximum allowed at KASE airport during the landing of the Aspen Economic Mission, where the runway width is limited to 98.42 ft. However, the Federal Aviation Administration (FAA) has approved an expansion plan that includes both the runway and overall airport infrastructure, with construction scheduled for completion by the end of 2027 or 2028. Since the *Infinity Jet* is expected to enter service in 2031, the airport's current size limitations will no longer be an issue by that time [8, 7, 28].

2 Methodology

The steps followed for the conceptual design of the *Infinity Jet* are presented in Fig. 2.0.1. Throughout the different phases, the work is carried out using empirical correlations, numerical and analytical studies performed with Python and Siemens NX, as well as results from experimental references.

The first step of the project involves analyzing the different missions the aircraft must fulfill, as well as existing aircraft that already operate in similar contexts. The goal is to study their configurations in order to identify the most suitable layout for the *Infinity Jet*. Once the configuration is fixed, it becomes possible to estimate key parameters

such as the Maximum Take-Off Weight (MTOW), wing characteristics, and required thrust. From these initial estimates, more detailed characteristics can be derived.

Static stability and performance are then assessed, and the aircraft geometry including the position of the wing and the empennage is iteratively adjusted until the stability criteria are met and optimal performance is achieved. The main objective is to design an aircraft that remains sufficiently lightweight in order to minimize fuel consumption, while still offering a range of features expected from a modern private jet with a target cruise speed of Mach 0.9. A concession on the Mach target of 0.92 in cruise has been decided. The team prioritized an aircraft capable of long ranges at Mach 0.9 rather than significantly reducing the range and increasing fuel consumption in order to reach 0.92. To limit congestion in the lower flight levels and reduce potential conflicts with commercial air traffic, it was decided that the aircraft would operate at a higher cruising altitude. A cruising altitude of 42651 ft was therefore chosen for the *Infinity Jet*.

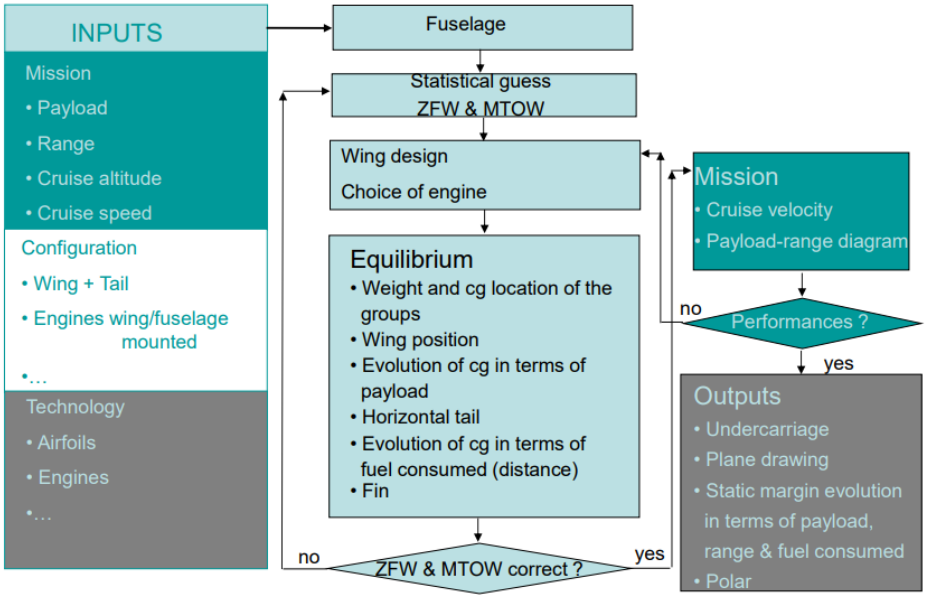

Figure 2.0.1: Summary of the conceptual design methodology [26].

Once these conditions are fulfilled, the geometry is finalized, marking the end of the conceptual design phase. The preliminary design phase then begins. At this stage, more detailed analyses are carried out using Siemens NX, Python based tools, and CFD simulations in order to evaluate the aerodynamics and drag more precisely, and to verify the aircraft's performance. The internal structural design of the aircraft is also developed during this phase.

3 Configuration

3.1 Existing configuration

In the early stages of conceptual design, it is crucial to analyze existing aircraft that perform similar missions. This approach provides reliable references for obtaining initial estimates of key parameters such as MTOW, payload capacity, range, and dimensions, which help generate the first approximations for the jet.

The targeted jets are the Bombardier Global 7500, Gulfstream G700, and Dassault Falcon 10X. These are three representative ultra-long-range jets that carry out missions similar to the target mission, with short- and long-range capabilities and cruise Mach speeds close to the objective of 0.9. The various parameters of these three jets are listed in Tab. 3.1.1, and images of the three are shown in Fig. 3.1.4 to analyze their respective configurations. This data has been used to inspire the initial estimates necessary to begin the conceptual design.

Parameter	Gulfstream G700	Global 7500 Bombardier	Dassault Falcon 10X
Range (nmi)	7750	7700	7500
MTOW (lb)	106 850	107 000	114 999
Max Payload (lb)	5985	5700	6613
Max Fuel (lb)	49 398	48 500	51 700
Passengers (-)	19	19	19
Length (ft)	109.84	110.89	109.58
Span (ft)	102.99	104	110.24

Table 3.1.1: Main characteristics of three jets validating missions close to the target missions.

Figure 3.1.1: Gulfstream G700

Figure 3.1.2: Bombardier Global 7500

Figure 3.1.3: Falcon 10X

Figure 3.1.4: Three jets validating missions close to the target missions [50, 45, 48].

3.2 Main components design

3.2.1 Wing

A high-wing configuration has been selected for the *Infinity Jet*, as it presents several advantages that align well with the design objectives:

- Higher ground clearance allowing a greater flexibility for engine placement, which is further discussed in Sect. 3.2.2.
- A shorter landing gear is required, resulting in a lighter overall aircraft.
- The landing gear can be stored in the fuselage allowing to store more fuel in the wing and thus increasing the aircraft's range.
- High-wing configuration improves lateral stability compared to mid or low wing designs.

Furthermore, the choice of a high wing configuration supports the design of long, slender wings with a higher aspect ratio than typically found on similar aircraft with low or mid wing. This design opportunity has been adopted, and an aspect ratio of 15 has been selected in order to reduce induced drag and fuel consumption.

3.2.2 Engine

The positioning of engines on an aircraft is a crucial factor that significantly impacts aerodynamic performance, noise levels, and maintenance considerations. Two primary configurations have been considered for the *Infinity Jet*, either engines mounted at the rear of the fuselage or engines placed under the wings, as illustrated in Fig. 3.2.1. Both configurations present distinct advantages and disadvantages and all relevant differences considered in the selection process are summarized in Tab. 3.2.1.

(a) Rear Fuselage Mounted

(b) Wing Mounted

Figure 3.2.1: Comparison of two engine mounting configurations.

Criteria	Rear Fuselage Mounted	Wing Mounted
Aerodynamic Considerations	Unrestricted wing design, nose-down moment	Occupies wing area, nose-up moment
Acoustic Impact	Further away from the cabin	+3–6 dB(A) in central and forward cabin
Heat Transfer Effects	No heat transfer to cabin, negligible impact on components	Possible heat transfer, reduced component lifespan
Stability Considerations	Strong nose-up moment	Minimal pitch moment
CG position	Shifted by 15%	Closer to thrust line
Design	More complex wing and fuselage structure, fan diameter is limited due to vibration constraints (BPR = 5–6)	Reduced lift moment, engine size can be larger, with ground clearance being the only limitation (BPR = 9–12)
Accessibility	Difficult engine access	Easier engine access
Engine-Out Handling	Lower yaw moment	46% higher yaw moment
Fire Hazard	Further away from fuel tanks	Closer to fuel tanks
Foreign Object Risk	Reduced risk	Higher risk of object ingestion

Table 3.2.1: Comparison of rear fuselage mounted and wing mounted engines.

After weighing all trade-offs, the wing-mounted engine configuration was deemed more suitable for the design. The main advantage being that this configuration gives the possibility to use larger engines with a higher by pass ratio than in a rear-fuselage mounted configuration. A higher bypass ratio results in a better specific fuel consumption (SFC), which in turn leads to reduced overall fuel consumption. The issue of noise generated by wing-mounted engines can be mitigated through effective fuselage insulation and the use of active noise cancellation technologies, as implemented in some modern jet aircraft [21].

3.2.3 Empennage

A T-tail configuration has been chosen for the empennage due to its better stability and control compared to other existing configurations, such as the V-tail and conventional tail. As the horizontal stabilizer is placed above the turbulent airflow from the wings, it improves stability, particularly at higher angles of attack during takeoff and landing. It also reduces aerodynamic interference by separating the horizontal stabilizer from the wing, allowing for cleaner airflow and enhancing performance. Additionally, since the engines are mounted under the wings, the T-tail configuration avoids potential flow disruption from the engine wake on the horizontal stabilizer, this placement ensuring more predictable aerodynamic behavior.

3.3 *Infinity Jet* CAD

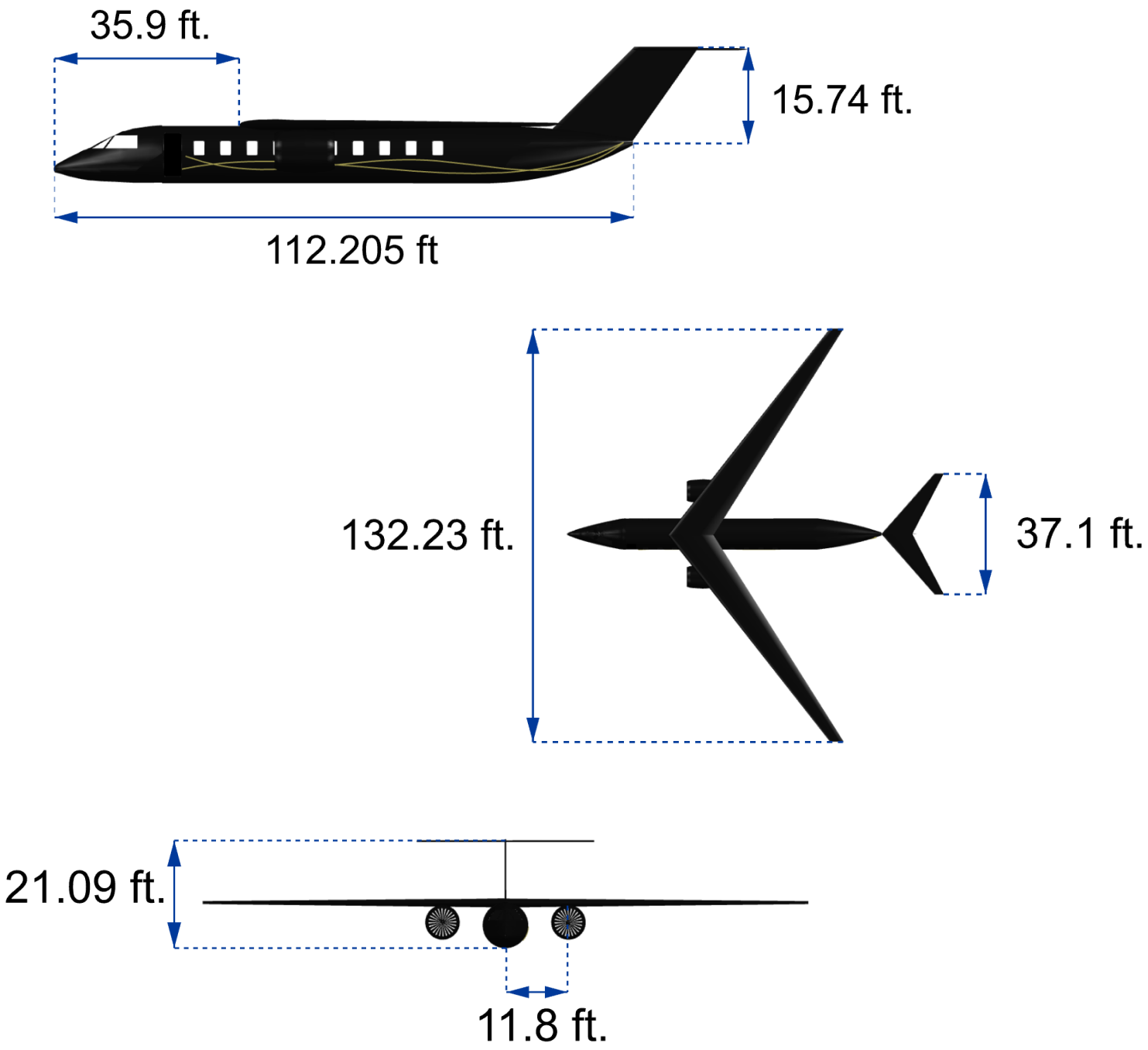

Figure 3.3.1: Three views of the *Infinity Jet*.

4 Component design

4.1 Wing

This section details the design process of the wing, involving the definition of fundamental and geometric parameters based on specific requirements. The first step is to estimate the necessary lift coefficient from an initial approximation of the cruise weight. Once this target is set, the wing geometry is adjusted to meet the AIAA Design Competition constraints. Raymer's method is applied to determine the optimal geometry [29].

4.1.1 Wing planform

In this subsection, the various values of the geometric parameters of the wings are presented. Their selection helps optimize the wing efficiency based on flight conditions and design objectives in order to reduce the drag and the fuel consumption. The wing planform is shown in Fig. 4.1.1.

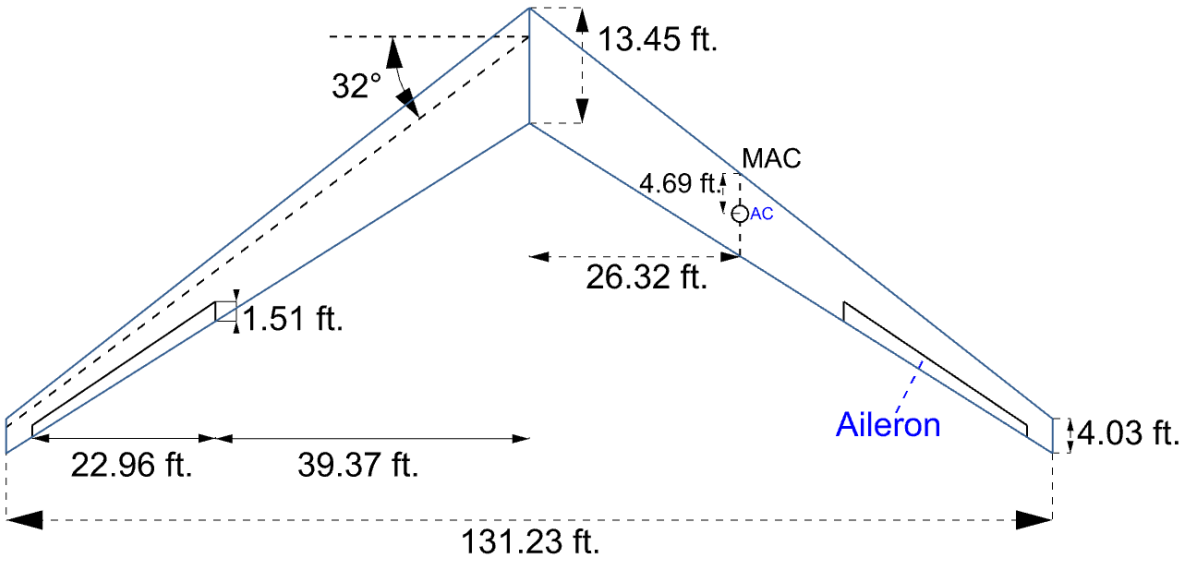

Figure 4.1.1: Wing planform of the *Infinity Jet*.

- **Span :** based on existing private jets capable of similar long-range missions, the wing span of the *Infinity Jet* is set at 131.23 ft.

- **Aspect ratio :** As explained in Sect. 3.2.1, the *Infinity Jet* has a higher aspect ratio than comparable aircraft, such as Dassault Aviation's Falcon 10X. A higher aspect ratio helps reducing induced drag and improves the lift-to-drag ratio, which is crucial for long-range aircraft as it directly impacts fuel efficiency. For this reason, the aspect ratio of the *Infinity Jet* has been set to 15.

- **Wing area** : The wing area can be determined from the aspect ratio and the span. In this case, its value is 1148.07 ft^2, which is slightly larger than similar aircraft.

- **Twist angle :** The wing twist is used to prevent tip stall before the wing root particularly during low-speed flight phases such as takeoff and landing. Typically, wing twists range between 0° and -5°, ensuring improved aerodynamic performance and stall behaviour. The twist angle is set to -1.5°, with the negative sign indicating a downward deflection of the leading edge.

- **Taper ratio :** The taper ratio is set to 0.3. This choice theoretically helps achieving an elliptical lift distribution, minimizing induced drag from wingtip vortices, as predicted by Prandtl's lifting-line theory [29]. This assumption on the distribution is verified in Sect. 5.1.1. This ratio is commonly used in high-performance subsonic aircraft, offering a good balance between drag reduction and structural considerations.

- **Chord at the root and chord at the tip :** Knowing the span, the wing area and the taper ratio the chords at root and tip can be determined [29], yielding respectively for the root and the tip : c_{root} = 13.45 ft and c_{tip} = 4.03 ft.

- **Anhedral angle:** For a high-wing configuration and for a subsonic swept swing, the dihedral angle range between -5° and -2° in order to avoid unconditional roll stability configuration. The anhedral angle is set at -2°.

- **Incidence angle :**The wing incidence angle i_w refers to the angle at which the wing is tilted relative to the fuselage. The incidence angle has been determined by equilibrium assessment in Sect. 5.3.1, yielding to i_w = 1.42°.

- **Sweep angle:** Given the flight conditions, the aircraft operates in the subsonic regime, with a cruise speed of Mach 0.9 at 42,650 feet. At such high subsonic speeds, a swept wing becomes necessary to delay the wave

drag associated with transonic flow. The sweep angle have been fixed at 32°, this value being verified in Sect. 4.1.2.

- **Position:** For reasons of static stability (see Sect. 5.3.1), the wing has been positioned at 32% of the fuselage length from the nose.
- **Aerodynamic center:** The position of the aerodynamic center has been determined using empirical correlations present in Torenbeek [39], giving an AC chord of 9.48 ft and $(x, y, z)_{AC} = (4.66, 26.32, 0)$ ft. The value of the moment coefficient has also been calculated and is $C_{m,AC} = -0.138$.

The different geometric parameters of the wing are summarized in the Tab. 4.1.1.

Parameter	Value	Parameter	Value
Span b (ft)	131.23	Wing area S (ft^2)	1148.07
Sweep angle $\Lambda_{c/4}$ (°)	32	Aspect ratio AR (-)	15
Twist angle ϕ (°)	-1.5	Chord at tip c_{tip} (ft)	4.03
Anhedral angle Γ (°)	-2	Chord at root c_{root} (ft)	13.45
Taper ratio λ (-)	0.3	Cruise AoA (°)	1.42
AC position (ft)	x= 4.66 , y = 26.32	AC chord (ft)	9.48
$C_{m,AC}(-)$	-0.138		

Table 4.1.1: Geometric parameters of the wing.

4.1.2 Airfoil selection

The choice of airfoil is dictated by the aircraft's cruise speed, as cruise represents the longest phase of flight. For high-subsonic flight, a supercritical airfoil is the most suitable choice, as it is specifically designed to minimize the side effect associated with shock formation. Unlike conventional airfoils, supercritical airfoils feature a flattened upper surface and a more pronounced aft camber, which helps increase the drag-divergence Mach number [18]. This design allows the aircraft to cruise near the critical Mach number without experiencing a sharp rise in drag, thereby improving aerodynamic efficiency.

The NASA SC(2)-XXXX supercritical airfoil family has been selected. In this naming convention, the last two digits represent the thickness-to-chord ratio as a percentage, while the first two digits correspond to the design lift

coefficient multiplied by 10.

Supercritical airfoils are designed to operate efficiently around a narrow optimal angle of attack, typically close to 0°, in order to remain within their drag bucket. Deviations from this optimal range lead to a sharp increase in drag, particularly pronounced in supercritical profiles. To minimize drag during cruise, the wing's incidence angle is therefore aligned with this optimal angle. A lift coefficient of 0.46 is required, which led to the selection of the NASA SC(2)-06XX and SC(2)-07XX airfoil series. The SC(2)-05XX series was discarded, as it does not meet the required 14% thickness-to-chord ratio, a condition which has been decided in order to to optimize both the structural efficiency and internal fuel volume of the wing.

The geometric parameters of the airfoil were determined based on data and simulations conducted with XFOIL for a first estimation (see Tab. 4.1.2) [20][22]. It is important to note the limitations of XFOIL, it only models two-dimensional airfoil sections and does not account for three-dimensional effects. Furthermore, it is designed for incompressible or slightly compressible flows, typically up to Mach 0.7. Therefore, direct performance evaluation at the cruise Mach number of 0.9 is not feasible due to significant compressibility effects. Instead, comparisons were made at Mach 0.7. These results remain valid under the assumption of a sufficiently large sweep angle, which effectively reduces the local Mach number experienced by the airfoil.

Airfoil	c_{l_α} **(1/rad)**	α_{l0} (°)	$C_{\text{L,design}}$ **(-)**	$\left(\frac{t}{c}\right)_{\text{max}}$ **(%)**	c_m **(-)**	M_{dd} **(-)**
NASA SC(2)-0714	11.5	-3.85	0.7	14	-0.15	0.76

Table 4.1.2: Geometric parameters of the NASA SC(2)-0714 at Mach 0.7 and Re = 15, 000, 000(-) [2].

In order to verify the validity of the required angle of attack α of the NASA SC(2)-0714 before the preliminary design phase, the evolution of the lift coefficient in function of α has been calculated using empirical relations [6]. Figure 4.1.2 shows that the required angle of attack to achieve the desired lift coefficient is approximately 1.42°, which is close to 0°.

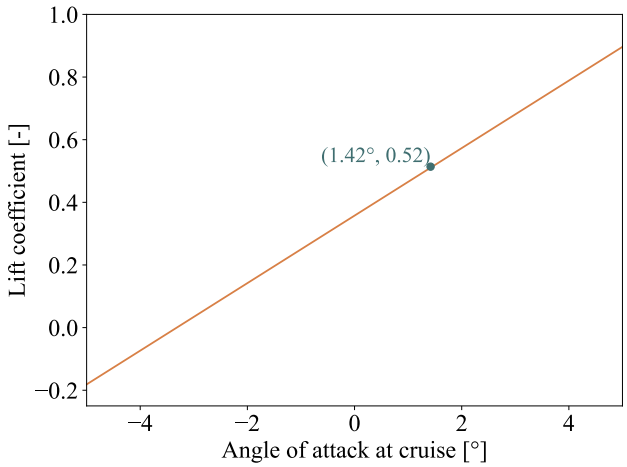

3

Figure 4.1.2: Lift coefficient as a function of the angle of attack of a NASA SC(2)-0714 airfoil, obtained through empirical relations at cruise.

- **Sweep angle :** Since the aircraft will be operating in a transonic regime, it is possible for the airflow to reach sonic speeds at certain points on the wings, which could negatively impact the aircraft's performance if the Mach number exceeds the drag-divergent Mach number. For this reason, the drag-divergent Mach number can be considered as the design Mach number and so the value of $\Lambda_{c/4} = 32°$ is verified with the airfoil NASA SC(2)-0714:

$$\cos(\Lambda_{c/4}) M_{\text{cruise}} = 0.76 \approx M_{dd} \tag{4.1.1}$$

4.2 Empennage

This section details the design process of the empennage, focusing on the definition of fundamental and geometric parameters based on specific requirements. The horizontal tail ensures trim by generating forces that counteract the moments produced by the aircraft, while also regulating pitch stability and maneuverability. The fin counteracts yawing moments, ensuring lateral stability. The objective is to minimize drag while ensuring the required stability and control. Raymer's and Sadraey's methodologies are applied to determine the optimal geometry of both the fin and the horizontal tail [29], [34].

4.2.1 Empennage planform

In this subsection, the various values of the geometric parameters of the fin and horizontal tail are presented. The fin and horizontal tail planform are shown in Fig. 4.2.1.

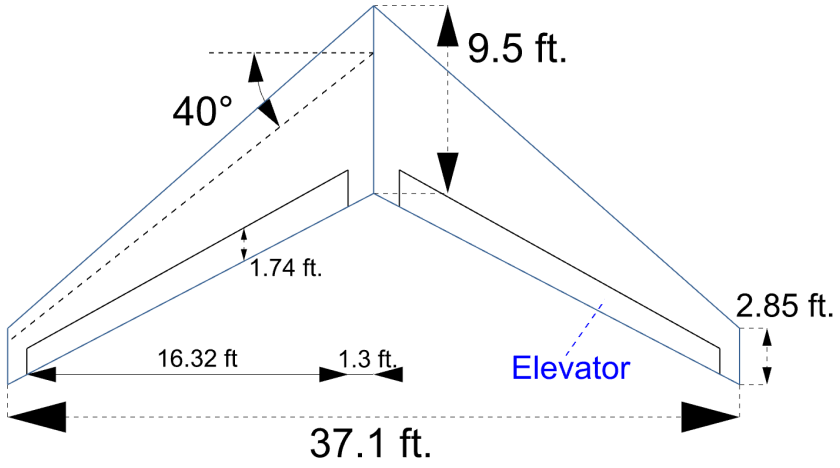

(a) Horizontal tail planform.

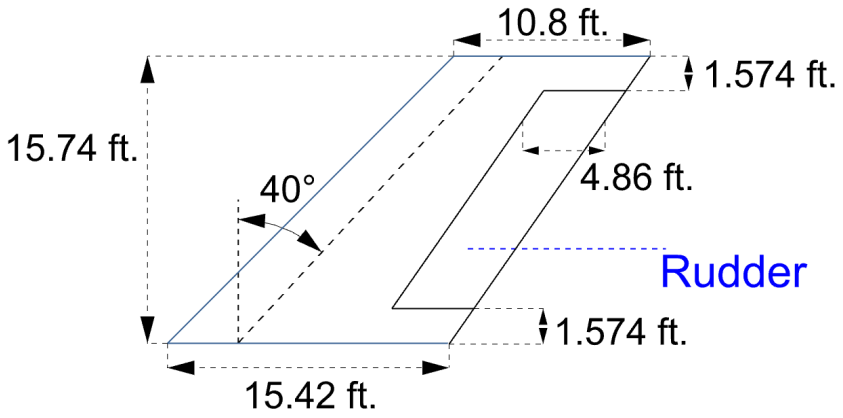

(b) Vertical tail planform.

Figure 4.2.1: Empennage planform of the *Infinity Jet*.

- **Aspect Ratio :** The aspect ratio of the fin generally ranges between 0.7 and 1.2 for a T-tail and between 3 to 6 for the horizontal tail. By taking into account all the necessary parameters and looking at what already exists, an aspect ratio of 1.2 has been selected for the fin while an aspect ratio of 6 has been chosen for the horizontal tail.

- **Taper ratio :** The taper ratio of the vertical stabilizer (fin) generally ranges between 0.6 and 1, while between 0.3 and 0.5 for the horizontal tail. In this design, the taper ratio is set to 0.7 for the fin and 0.3 for the horizontal tail, ensuring a balance between aerodynamic efficiency and structural weight.

- **Sweep angle :** The quarter-chord sweep angle is typically between 30° and 40° for a vertical stabilizer (fin).[6, 34]. As for the horizontal tail, it is typically designed with a sweep angle at least 5° greater than that of the wing to ensure favorable aerodynamic interaction and stability. In this case, both the fin and the horizontal

tail have been assigned a sweep angle of 40°.

- **Empennage volume coefficient :**

  The surface areas of the horizontal and vertical stabilizers are estimated using tail volume coefficients, which relate tail geometry to the wing's reference dimensions and tail arm lengths:

$$V_H = \frac{l_H S_H}{\bar{c} S} \quad \text{and} \quad V_F = \frac{l_F S_F}{b S} \tag{4.2.1}$$

  Typical values for V_H range from 0.5 to 1.2, while V_F usually lies between 0.03 and 0.12 [6, 34]. The selected coefficients are 1.05 for the horizontal tail and 0.075 for the vertical tail.

  The horizontal tail-to-wing surface ratio $\frac{S_H}{S}$ typically ranges from 0.2 to 0.4 and plays a significant role in longitudinal stability. Inversely,, the vertical tail-to-wing surface ratio $\frac{S_F}{S}$ is generally smaller [6, 34]. The chosen values are 0.2 and 0.18, respectively.

- **Empennage surface areas :** The surfaces of the empennage have been determined from the previously ratios of the fin and horizontal tail areas to the wing area. It yields, respectively : $S_H = 229.63\text{ft}^2$ and $S_F = 206.66\text{ft}^2$.

- **Chord at the root and chord at the tip :** These parameters have been defined in the same way than for the wing. Yielding for the fin to: $c_{root} = 15.42\text{ft}$, $c_{tip} = 10.8\text{ft}$ and for the horizontal tail: $c_{root} = 9.5\text{ft}$ and $c_{tip} = 2.85\text{ft}$.

- **Twist angle :** No twist angle is applied to the horizontal tail. For symmetry purposes, the vertical fin is also never twisted [29].

- **Dihedral angle :** Following the same reasoning as for the twist, the dihedral angle is set to 0° for both the fin and the horizontal tail.

- **Span :** Knowing the surface area and the aspect ratio of both the fin and the horizontal tail, their respective spans can be calculated. The resulting values are:

$$b_F = 15.74\text{ ft} \quad \text{and} \quad b_H = 37.1\text{ ft}.$$

The incidence angle of the horizontal tail is also determined using empirical relation, similar to the wings [6].

Yielding to $i_H = -0.53°$. The different geometric parameters of the empennage are summarized in the Tab. 4.2.1.

Parameter	Fin	Horizontal tail	Parameter	Fin	Horizontal tail
Span b (ft)	15.74	37.1	Area (ft^2)	206.66	229.63
Taper ratio λ (-)	0.7	0.3	Aspect ratio AR (-)	1.2	6
Twist angle ϕ (°)	0	0	Chord at root c_{root}(ft)	15.42	9.5
Dihedral angle Γ(°)	0	0	Chord at tip c_{tip}(ft)	10.8	2.85
Sweep angle $\Lambda_{c/4}$(°)	40	40	Tail / wing surfaces(-)	0.18	0,2

Table 4.2.1: Geometric parameters of the fin and horizontal tail.

4.2.2 Airfoil selection

The empennage geometry is significantly simpler than that of the wing. To reduce manufacturing costs and streamline production, symmetric airfoils such as those from the NACA four-digit series are typically used [6, 29]. For this design, the NACA 0012 profile has been selected for both the horizontal tail and the vertical fin.

4.3 Propulsion

4.3.1 Engine selection

Several parameters were considered to select the most suitable engine for the *Infinity Jet*. The first critical parameter is thrust. The engine must provide enough thrust to overcome drag in all flight configurations, particularly during demanding phases such as takeoff and climb. During cruise, the engine should not operate at full power when flying at the expected cruise Mach number, which is the phase that requires the least energy. To ensure suitability, the drag that the engine must be able to overcome has been initially estimated using empirical methods. But more detailed and comprehensive drag study is presented in Sect. 5.1.2. Based on these evaluations, it was determined that the engine must be capable of providing sufficient thrust to overcome approximately of a drag coefficient of 0.067 during takeoff and around 0.027 in cruise conditions.

The weight of the engine is another essential parameter. A heavier engine will consume more fuel due to the increased weight, which affects overall fuel efficiency. Therefore, while Specific Fuel Consumption (SFC) is an important metric to minimize fuel consumption, there is a trade-off with weight. Lowering SFC is desirable, but if the engine is too heavy, the advantage of reduced fuel consumption may be outweighed by the added fuel requirements for a heavier aircraft.

Given the high-wing configuration of the *Infinity Jet*, it is interesting to take advantage of it by considering engines with a high bypass ratio. This is because a high-wing configuration offers more clearance between the ground and the engine. The decision was made to opt for a turbofan engine, as turbofans are particularly efficient at high altitudes and transonic speeds, which are required for the mission profile of the *Infinity Jet* while keeping a reasonable SFC.

A comparison of five different engines used in aircraft with similar missions is provided in Tab. 4.3.1.

Engine	Static T (lbf)	BPR (-)	Fan Diameter (in)	Length (in)	Weight (lb)	SFC (lb/(lbf.s))
CF34-10	20,360	5.4	53	88.7	3,760	0.00022
GE PASS	18,900	5.8	52	102.7	3,950	0.00024
PW 1500G	19,500	12	73	125.4	4,800	0.000141
PW 1700G	15,500	9	56	113.5	3,800	0.00015
PW 1900G	18,500	12	73	125.4	4,800	0.000143
Leap 1B	23,000	9	69.4	118.1	6,128	0.000157

Table 4.3.1: Main characteristics of different turbofan engines at sea level and SFC at cruise [14], [15], [30] .

An other important factor in the selection is the **weight-to-thrust ratio**, which is a good indicator of engine performance. A lower weight-to-thrust ratio generally indicates a more powerful engine for its weight. For conventional business jets, this ratio typically ranges from 0.18 to 0.22, whereas for ultra-high bypass ratio (UHBR) turbofans, which offer better fuel efficiency and lower noise emissions, it can reach 0.25–0.27.

This higher weight-to-thrust ratio is acceptable as UHBR engines operate more efficiently at cruise, but they are less tolerant to density changes at high altitudes due to their large fan diameters and reliance on bypass air. Therefore, the engine selection process prioritized this ratio over thrust alone, while also considering cruise performance.

The **PW1900G**, with a thrust of 18,500 lbf and a weight-to-thrust ratio of 0.26, aligns well with the *Infinity Jet*'s requirements. It is already used on aircraft such as the Embraer E190-E2 and E195-E2, ensuring operational reliability. Its 73-inch fan diameter suits the high-wing configuration, providing sufficient ground clearance. It has

therefore been decided to select the **PW1900G** for the *Infinity jet*. For stability, the engines are mounted under the wings at a spanwise position of 6.56 ft, as discussed in Sect. 5.3.1.

4.3.2 Thrust Model

As an aircraft climbs, the air density (ρ) decreases significantly with altitude. This reduction in density limits the amount of mass the engine can ingest, which directly reduces the available thrust. In a first-order approximation, thrust drops proportionally with air density. However, modern turbofan engines partially compensate for this loss: colder and less dense air allows for higher pressure ratios and potentially higher engine speeds, which slightly mitigate the performance drop. Furthermore, engines with high or ultra-high bypass ratios (UHBR) have large fans that move massive quantities of air. While this is advantageous at low altitudes, it also makes them more sensitive to the density drop at altitude.

NASA studies [24, 31] confirm that at cruise altitudes such as 49,000 ft, modern high-bypass aircraft like the Boeing 737 MAX (LEAP-1B) and Embraer E190-E2 (PW1900G) operate with only about 15–20% of their maximum sea-level thrust. This considerable thrust decay highlights the need to model it accurately in performance studies.

To capture this effect, The thrust model used has been based on the method described by Jan Roskam in *Airplane Design Part VI* [32]. It recommends to approximate the thrust lapse as:

$$T \propto \left(\frac{\rho}{\rho_0}\right)^n \tag{4.3.1}$$

where the exponent n depends on the bypass ratio. For high-bypass engines, n is typically between 0.7 and 0.8. In this case, a value $n = 0.8$ have been selected in order to remain conservative, and because it matches well with observed cruise thrust levels from the PW1900G and LEAP-1B. Resulting curves are consistent with the thrust values from some references [35] [31], both of which report similar thrust retention trends.

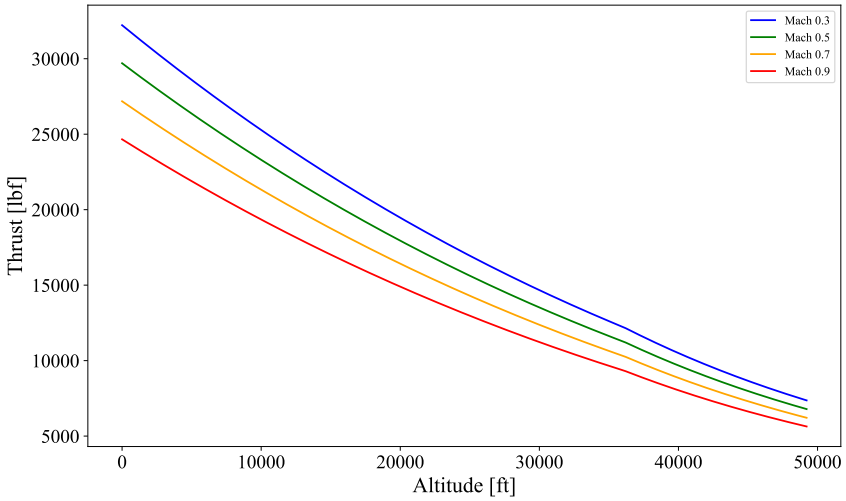

Figure 4.3.1: Estimated thrust lapse with altitude for various Mach numbers. Note: Cruise engines are typically throttled to 80% power, which is also assumed in the calculations.

4.3.3 Mach Effect on Thrust

While air density governs altitude thrust lapse, aircraft operating at transonic speeds (Mach 0.7–0.9) encounter another problem. As the aircraft's speed approaches the fan exit velocity, shock waves and increased inlet drag reduce the effective pressure recovery, degrading engine performance. This phenomenon is especially pronounced in high-bypass engines due to their large frontal area and low exhaust speeds.

To account for this additional loss, a corrective term based on the Eurocontrol BADA model and NASA Langley data [25] has been introduced

$$T_{\text{avail}} = T_0 \left(\frac{\rho}{\rho_0} \right)^{\alpha} (1 - kM) \tag{4.3.2}$$

The $(\rho/\rho_0)^{\alpha}$ term models the density-based lapse, and the $(1 - kM)$ term penalizes thrust as Mach increases. The constants $\alpha = 0.8$ and $k = 0.35$ were calibrated to match the behavior of modern high-bypass engines like the PW1900G and LEAP-1B.

4.4 Control surfaces

4.4.1 Primary Flight Control Surfaces

The primary flight control surfaces of the aircraft are the ailerons, the elevator and the rudder. These surfaces were sized based on typical area ratios found in the literature (Roskam [33], USAF DATCOM [40]), performance goals and stability requirements.

Ailerons

The ailerons are located near the wingtips and are responsible for roll control by generating differential lift between the two wings. Their position provides high roll effectiveness with small control deflection. A constant chord has been assumed for simplification. The characteristic values are summarized in Tab. 4.4.1. The span ratio indicates the fraction of the half-span at which the ailerons being and end.

Chord c_a (ft)	Area S_A (ft^2)	Span pos. (ft)	Span ratio (-)
1.5	64.58	78.74–124.67	0.60-0.95

Table 4.4.1: Aileron geometry and spanwise location on the wing.

Elevator

The elevator is mounted on a T-tail and spans nearly the full semi-span of the horizontal tail, with a small clearance near the root to avoid interference with the vertical fin. A constant chord has been assumed for simplicity. The elevator's area has been sized to ensure sufficient pitch control authority during all phases of flight. The characteristic values are summarized in Tab. 4.4.2. The span ratio indicates the fraction of the half-span at which the ailerons begin and end.

Chord c_e (ft)	Area S_e (ft^2)	Span pos. (ft)	Span ratio (-)
1.74	59.04	0.94–17.9	0.05–0.95

Table 4.4.2: Elevator geometry and spanwise location on the horizontal tail.

Rudder

The rudder is installed on the vertical tail, starting above the structural root region and ending just below the horizontal stabilizer. It has been designed with a constant chord c for simplicity of calcul and covers the central portion of the fin to ensure effective yaw control. The characteristic values are summarized in Tab. 4.4.3. The span ratio indicates the fraction of the half-span at which the ailerons begin and end.

Chord c_r(ft)	Area S_r(ft^2)	Span pos.(ft)	Span ratio(-)
4.86	68.02	1.75–15.77	0.10–0.90

Table 4.4.3: Rudder geometry and placement on the vertical tail.

4.4.2 High-Lift Devices

Several flap configurations can be used, ranked by increasing aerodynamic efficiency but also increasing mechanical complexity. Before calculating the lift with high-lift devices, $C_{L_{\max}}$ was first determined under approach conditions. This allows for a comparison of the lift increase provided by high-lift devices and help assess which high-lift devices are necessary.

$$C_{L,\max} = 0.95 \cos \Lambda_{1/4} \frac{(c_{l,\max})_{\text{root}} + (c_{l,\max})_{\text{tip}}}{2} = 1.621, \tag{4.4.1}$$

where $(c_{l,\max})_{\text{root}}$, and $(c_{l,\max})_{\text{tip}}$ are the maximum lift coefficient of the airfoil at the root and at the tip, respectively. It must be possible to take off and land on a 6,000 ft runway while complying with FAA (FAR-25) regulations [11]. Under normal conditions, the aircraft must be able to take off using only 60% of the runway. Additionally, landing must be achievable within 60% of the runway length without relying on engine braking.

Condition	Take-off @ sea level +18 °F	Landing @ sea level +18 °F
$C_{L,\max,\text{clean}}$ (-)	1.62	1.62
$C_{L,\max,\text{required}}$ (-)	1.85	2.03
$\Delta C_{L,\max}$ (-)	0.229	0.411

Table 4.4.4: Comparison of Maximum Lift Coefficients under Different Conditions.

The calculations follow DATCOM 1978 [40]. The increase in the maximum lift coefficient due to trailing-edge

flaps is obtained using correction factors applied to baseline airfoil data:

$$\Delta c_{l,max,f} = K_1 K_2 K_3 (\Delta c_{l,max})_{base}, \tag{4.4.2}$$

where K_1, K_2, K_3 are correction factors and $(\Delta c_{l,max})_{base}$ is the maximum increase in the lift coefficient for a flap with a 25% flap chord. Their respective value is given by: $K_1 = 1$, $K_2 = 0.95$, $K_3 = 1$, and $(\Delta c_{l,max})_{base} = 1.621$ [29].

The 3D lift coefficient increase is determined from its 2D counterpart, considering the wing sweep and flap area:

$$\Delta C_{L,\text{max,flaps}} = \Delta c_{l,\text{max,flaps}} \frac{S_{\text{flaps}}}{S} K_\Lambda, \tag{4.4.3}$$

where S_{flaps} is the flaps surface and $K_\Lambda = 0.83$ is an empirical correction factor for taking into account the wing sweep Φ_{25°.

A two-slot Fowler flap has been selected as the high-lift device, as it offers the best compromise between aerodynamic performance and mechanical complexity. A single-slot flap, even with a leading-edge slat, does not meet the recommended landing performance requirements. Although a triple-slotted flap could further improve takeoff and landing capabilities, the increased mechanical complexity, weight, and cost make it less attractive for this design. Finally, a deflection angle of 20° has been applied for takeoff and 40° for landing, resulting in an effective increase in wing surface area of approximately 25% and 35%, respectively.

4.5 Fuselage

4.5.1 Cabin design

To meet the customer needs, the cabin dimensions have been defined to accommodate all the services present in this ultra-premium jet. The balance between space and efficiency has been carefully studied, resulting in a cabin with dimensions exceeding those of jets in the same category, such as the Bombardier Global 7500, thus offering a higher level of comfort and commodities. Thanks to these optimizations, the cabin dimensions are approaching those of Boeing Business Jets while benefiting from a MTOW reduction of more than 45 %, thereby improving the aircraft's overall efficiency. The final dimensions of the fuselage are visible in Fig. 4.5.1.

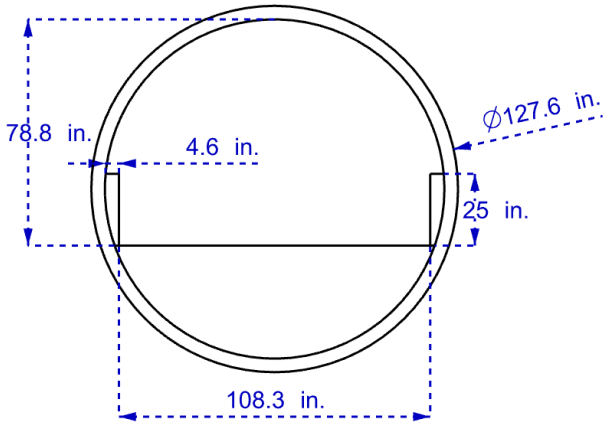

Figure 4.5.1: Fuselage centerline diagram.

The cabin, with a total length of 59.04 ft (with 6.56 ft of baggage compartment in the tail), provides sufficient space to be divided into several distinct sections, each with a specific ambiance and function. This layout is designed to maximize passenger comfort while meeting their various needs during the flight, as illustrated in Fig. 4.5.2. For the exit door, according to the FAA regulations, the required number of emergency exits is determined by the aircraft's seating capacity. For aircraft with fewer than 60 passengers, having a single emergency exit is fully compliant with the legislation. In the need emergency, this single exit is sufficient to ensure a safe and efficient evacuation. Thus, the use of a single emergency exit being the main door, is fully in accordance with the FAA guidelines [1].

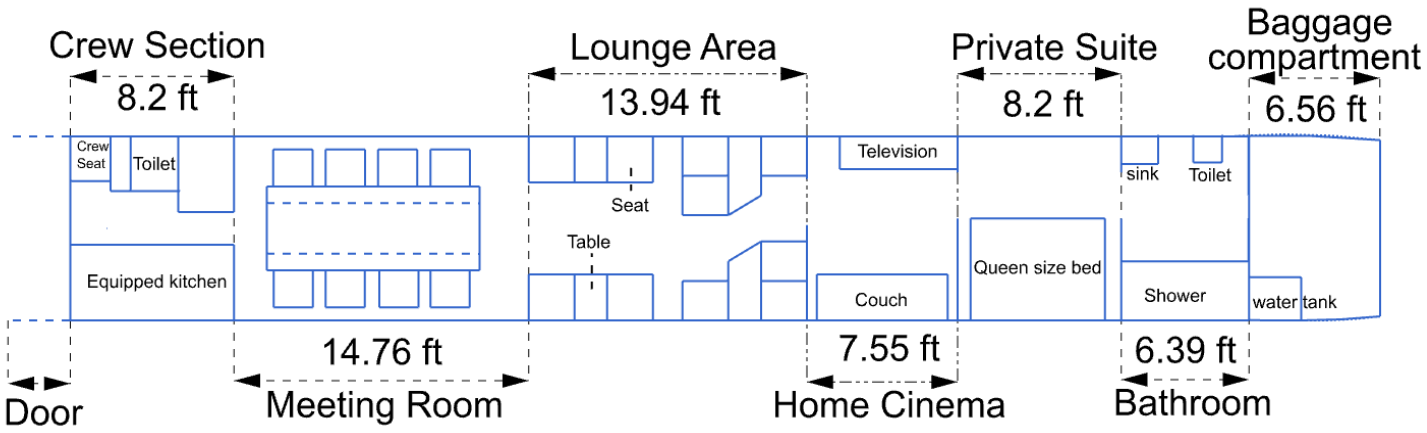

Figure 4.5.2: Layout Of Passenger Accommodations (LOPA).

- **First Section, Meeting Room:** The front section is dedicated to meetings and presentations, equipped with multiple high-definition screens displaying various types of information. When not being used for meetings,

the table and chairs can be folded away, freeing up space for other activities or passage.

- **Second Section, Lounge Area:** The next area is a comfortable lounge equipped with ten large reclining seats that can be converted into beds for optimal rest. Adjustable tables are also available, allowing passengers to work or dine as needed.
- **Third Section, Home Cinema:** A home cinema is set up with a three-seater convertible sofa and a large screen. This section provides a quiet, dedicated space for passengers to relax.
- **Fourth Section, Private Suite:** The private suite includes a Queen-size bed, a television, and built-in storage, offering an intimate space for rest or work in complete privacy.
- **Fifth Section, Bathroom:** Room with a spacious shower, toilet, and sink, all adapted for passengers with reduced mobility.
- **Crew Section:** At the front of the cabin there is a dedicated crew area includes a kitchen for preparing meals at any time for the passengers, a designated crew seat is also available. Additionally, a restroom is accessible to both the crew and passengers in meetings, allowing them to avoid crossing the entire aircraft to reach the main bathroom.
- **Baggage compartment:** A part of the tail is dedicated to the luggage storage and contain also a 15.8 ft^3 of water tank connected to the shower and a water heater to keep the water at the desired temperature. As with the rest of the cabin, this section is equipped with an air-conditioning system to keep baggage at the desired temperature.

4.5.2 Fuselage dimensions

The dimensions of the fuselage depend on the cabin, the nose and the tail. These last two depend on 2 factors which influence their length. For the nose, the length/diameter ratio N_F has to be greater than 1.5 due to pressurization, it was decided to set it at $N_F = 2$ limiting as possible the drag divergence Mach number. The tail length/diameter ratio A_F is generally between 1.8 and 3.5 and has been fixed here at $A_F = 3$. This gives rise to the final dimensions of the fuselage visible on Fig. 4.5.3.

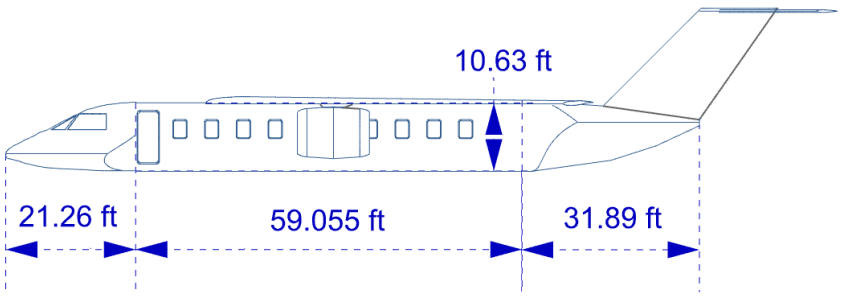

Figure 4.5.3: Side view of the *Infinity Jet*.

The nose profile has a classic shape, inspired by existing aircraft such as Bombardier Global 7500. But the upper section has been redesigned to have better performance at the well suited for transonic flow, reducing drag. The upper section follow a Von Karman profile and can be seen on Fig. 4.5.4

The tail upsweep angle has been set at 13° as it is commonly set to ensure proper maneuverability during take off.

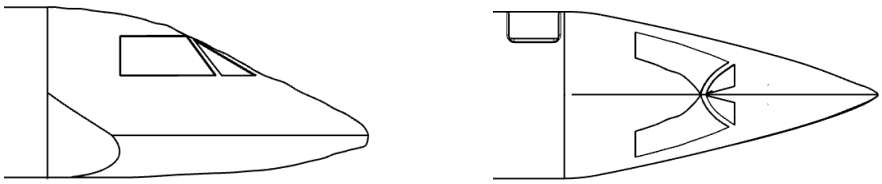

(a) Side view **(b)** Upper view

Figure 4.5.4: Nose view of the infinity jet

4.6 Landing gear

4.6.1 Configuration

The landing gear of the jet follow a tricycle configuration. A diagram of this configuration can be seen in Fig. 4.6.2. This choice is based on a rear main landing gear made up of two gear and a front gear. This design has several advantages, first of all in term of stability but also in terms of safety and ease of maneuvering. Moreover, this system is particularly adapt on take off and landing situation on small and narrow tracks which is the case in certain missions of the jet.

A fix landing gear having significant impact on jet's performance, the landing gear is retractable. To better distribute loads and reduce the stress on each tire, it was decided to equip the three landing gear with two tires each. This configuration ensures a more balanced weight distribution, reducing the risk of tire failure and improving the

reliability and durability of the landing gear.

4.6.2 Landing gear position

In private jets, the clearance between the ground and the fuselage generally varies from 0.66 to 4.92 ft, allowing passengers to embark and disembark without the need for external stairs, using only the built-in door. Due to the relatively large fuselage diameter of this private jet, the clearance height is set at 4.59 ft.

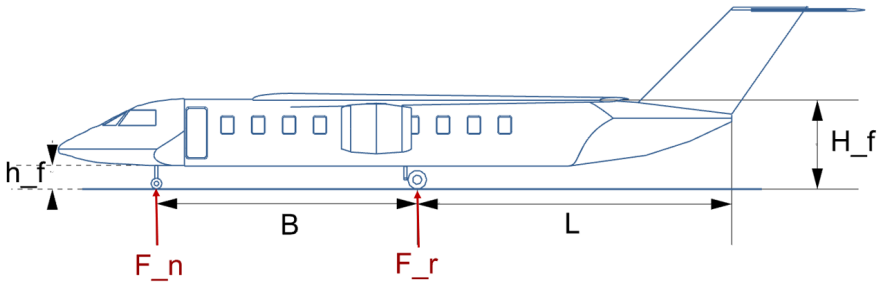

Figure 4.6.1: Landing gear configuration

From this height and with the tail sweep angle fixed at $\gamma = 13°$, the distance between the aft end of the jet and the rear landing gear can be determined, $L = 65.93$ ft. Looking at Fig. 4.6.2, L_β the distance separating the rear landing gear from the center of gravity (at MTOW) has been determined knowing the length of the plane, L, and the length between the nose and the center of gravity $L_{CG} = 38.93$ft. The results obtained is: $L_\beta = 7.345$ ft.

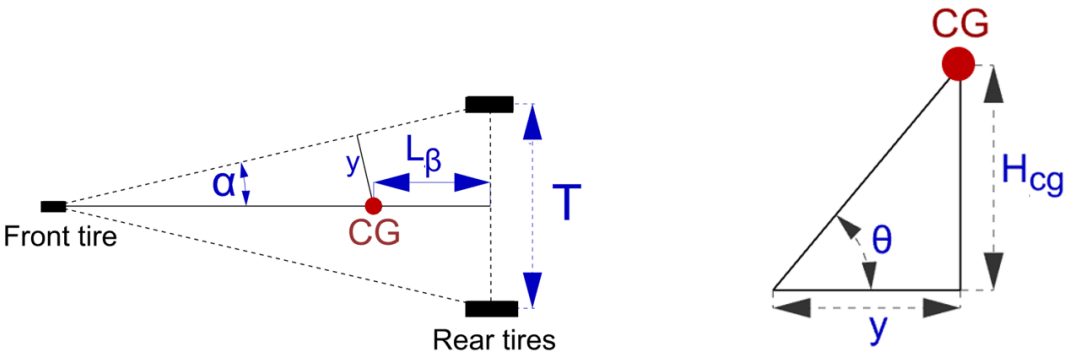

(a) Top view, nose of the plane being on the left

(b) Side view

Figure 4.6.2: Landing gear configuration

It has been assumed that the static force at the nose gear carries 17 % of the total weight and the static force at main gear carries 83 % of the total weight of the plane. Based on this assumption, the force that the main landing gear need to support is $F_r = 0.83W$ with W being the total mass of the plane. Knowing that, B the distance between

the nose gear and the main gear at MTOW has been determined:

$$B = \frac{L_\beta W}{W - F_R} = 36.725 \text{ ft.} \tag{4.6.1}$$

The angle θ visible on Fig. 4.6.2 b) takes generally a value between 35° and 55°. The value of $\theta = 37°$ has been chosen thus ensuring a sufficient turning radius on the ground while preventing the aircraft from turning over. Knowing this value, y, α and the distance between two rear gear T in Fig. 4.6.2 have been obtained. The different results are summarized in Tab. 4.6.1.

Parameter	Value	Parameter	Value
Upsweep angle γ	13°	Length rear wheelbase T (ft)	13.438
Height of landing gear (ft)	4.59	Distance rear gear -end of jet L (ft)	65.93
Distance CG - rear gear, L_β (ft)	7.345	Length nose - rear gear B (ft)	43.2
y (ft)	10.65	α (°)	17.279
Fuselage height (ft)	15.22		

Table 4.6.1: Parameters of the landing gear calculated with plane at MTOW

It should be noted that in the present calculation, the main landing gear track width exceeds the fuselage width. While mechanically more complex, this configuration is not uncommon in aviation, particularly for high-wing aircraft. The retraction mechanism will followed existing configurations, as seen on aircraft such as the ATR 72, Bombardier Dash 8 Q400, or the C-27J Spartan [46, 43, 42].

4.6.3 Tires and brakes

Tires

To prevent potential overload issues and reduce the frequency of maintenance, a safety margin of 25 % is applied to each load that the tires must support. The main landing gear support 83% of the weight split between four tires while the two nose tires support the 17% remaining.

It has been decided to purchase tires from Good Year. After consulting the manufacturer's datasheets, it follows that the appropriate tires for the nose gear are 21x7.25-10, while for the main gear 36x11.0-18 tires will be used [53].

Parameter	Nose tires	Main tires
Maximum static loads [lbf]	12000	35800
Tire diameter [in]	21	36
Rim diameter [in]	10	18
Tire width [in]	7.25	11

Table 4.6.2: Tyre specifications

Brakes

A disk brake system has been chosen due to superior performance and reliability in a wide range of conditions. The missions assigned to this jet include landings and takeoffs on runway with highly variable characteristics, ranging from cold to hot climates and from dry to slippery surfaces. Disc brakes are particularly well-suited for these conditions, as they efficiently manage heat dissipation during landing. This is especially important for missions such as the *Napa Economic Mission* to Mexico City where the aircraft will operate on dry runway with temperature reaching up to 85°F.

Disc brakes also reduce the risk of deformation and excessive wear, ensuring maximum safety. Additionally, they are easier to access for maintenance, as they are located outside the wheel, unlike drum brakes which are placed inside and therefore more difficult to access.

4.7 Material selection

The different parts of the aircraft are subject to various constraints and selection of suitable materials is significant. Several key constraints have been considered due to the unique operational environment. The main considerations are:

- Strength and durability
- Weight minimization
- Cost-effectiveness
- Corrosion resistance
- Fatigue resistance

The wings, fuselage, tail, nose, and empennage will be constructed from CFRP, using HexTow® IM7 fibers 12K in a HexPly® 8552 epoxy matrix. This laminated composite is designed to approach quasi-isotropic behavior

through fiber orientation, ensuring optimized stiffness and strength along load paths, making it ideal for aerospace applications. IM7 fibers offer an ideal balance of strength, stiffness, and cost, making them a standard in commercial and business aviation. The 8552 matrix includes thermoplastic particles to improve impact resistance, but requires pre-impregnation due to its high viscosity.

A minimum cured thickness of 0.0591 in is set to maintain a proper fiber volume fraction (56–60%). Below this value, machining tolerances affect resin content, leading to dry zones or resin-rich area, both of which reduce mechanical performance. The Tab. 4.7.2 summarizes the mechanical properties of CFRP [19].

Property	Value	Property	Value
Tensile strength (ksi)	104	Poisson's ratio (-)	0.316
Tensile modulus (ksi)	7977	Density (lb/in^3)	0.0567
Shear strength (ksi)	18.1	Price (USD/lb)	160

Table 4.7.1: Mechanical, physical properties and price of HexPly® 8552 IM7 12K.

The landing gear will be made of high-strength, corrosion-resistant steel, chosen for its durability and ability to withstand heavy loads during takeoff and landing without permanent deformation. While heavier than CFRP, steel offers excellent reliability and cost-effectiveness. To enhance its resistance to corrosion, a protective surface treatment will be applied. The Tab. 4.7.2 summarizes the mechanical properties of HSCR steel[41].

Property	Value	Property	Value
Tensile strength (ksi)	295	Density (lb/in^3)	0.280
Tensile modulus (ksi)	225	Price (USD/lb)	6

Table 4.7.2: Mechanical, physical properties and price of HSCR steel.

5 Aircraft analysis

5.1 Aerodynamics

The aerodynamics of the *Infinity Jet* has been calculated using empirical correlations during the conceptual design. A more detailed analysis is conducted in this section in order to obtain more accurate results. The lift analysis is conducted using *DARTFlo* (Discrete Adjoint for Rapid Transonic Flow) which is an open-source C++/Python, unstructured finite-element, full potential solver developed by Adrien Crovato at the University of Liège [9]. The wing being the main lifting surface of the jet, the study on *DARTFlo* will be limited to it and compared with the empirical results. All simulations conducted in the lift analysis sections using Darflo and empirical methods were performed under the conditions shown in Table 5.1.1. It is important to understand the assumptions *DARTFlo* make in order to properly interpret the results. *DARTFlo* solves the full potential equation assuming an inviscid flow, and therefore neglects the boundary layer. As a result, shock waves may not appear at the same locations and with a higher strength than in a viscous flow.

Mach	Altitude	Flight configuration
0.9	42650 ft	Cruise

Table 5.1.1: Conditions of flight during *DARTFlo* simulations

In the second part, a detailed drag study evaluating the contributions of the different part of the plane has been conducted following Torenbeek methodology [39] in order to estimate the drag during cruise, take-off and landing configuration.

5.1.1 Lift analysis

In order to ensure reliable results, a convergence study on *DARTFlo* has been conducted with respect to both domain size and mesh resolution. The evolution of the lift and drag coefficients with a mesh refinement and an increasing number of element is shown in Fig. 5.1.1, where satisfactory convergence is observed.

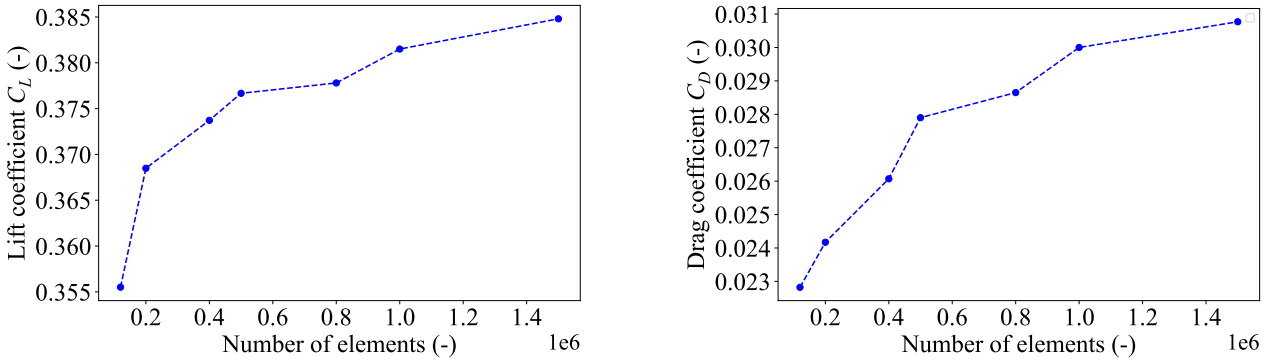

(a) Wing lift coefficient C_{L_w}

(b) Wing drag coefficient C_{D_w}

Figure 5.1.1: Evolution of wing lift and drag coefficient computed at conditions listed in Tab. 5.1.1, at $\alpha = 0°$ with mesh refinement.

For the results presented below, a mesh composed of approximately 800,000 elements was used, including around 300,000 elements on the wing surfaces. A tolerance of 5% in the computed values of c_l and c_d was considered acceptable. The mesh is of the Delaunay type, with element size on the wing set to $\frac{c_{\text{MAC}}}{100}$ (with c_{MAC} the mean aerodynamic chord worth 8.72 ft) and a stretching factor of 1.2 applied throughout the domain. To ensure numerical stability and avoid inaccuracies, a mesh coarsening of up to seven times the wing mesh element size is introduced near the trailing edge of the wing tip. This refinement strategy helps avoiding artificial singularities, as *DARTFlo* assumes infinite velocity at the wing tip's trailing edge in order to solve the governing equations.

Lift produced by the wing

The lift generated by the wing can now be evaluated as a function of the aircraft's angle of attack. This variation is illustrated in the graph 5.1.2 and compared to empirical estimations

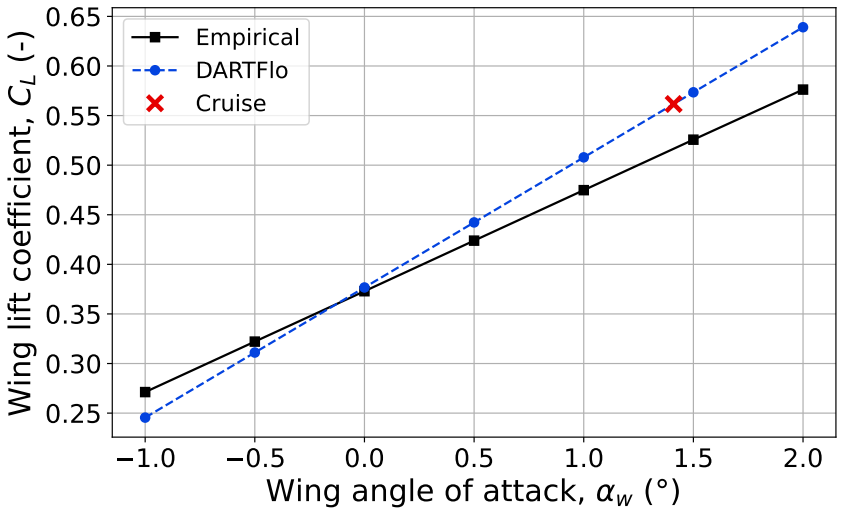

Figure 5.1.2: Evolution of the wing lift coefficient with the angle of attack computed at conditions listed in Tab. 5.1.1

Looking at Fig. 5.1.2, it can be seen that the results between *DARTFlo* and the empirical correlations are not far apart. At cruise, the difference of both lift coefficients are only about 7% suggesting that the wing is designed based on accurate estimations. Looking at Tab. 5.1.2, the main difference lies in the slope of the curve where the empirical results tend to underestimate it. It can be explain by the fact that shocks are not take into account in the empirical calculations. However, in transonic flight at Mach 0.9 shock waves are present and *DARTFlo* takes them into account in its calculation, explaining this difference.

The $C_{L_{\alpha w}}$ is therefore updated and the value $C_{L_{\alpha w}} = 7.52(\text{rad}^{-1})$ is used for stability and structure calculations using this new more accurately calculated value since DARTFlo models better the physics of the problem.

	Empirical	*DARTFlo*
Lift coefficient slope, $C_{L_{\alpha w}}$	6.21 (rad^{-1})	7.52 (rad^{-1})

Table 5.1.2: Lift coefficient slope with *DARTFlo* and empirically

Moment coefficient of the aerodynamic center of the wing

The moment coefficient at the aerodynamic center was first estimated empirically and is summarized in Tab. 5.4.6. However, when using the empirically estimated position of the aerodynamic center for the *DARTFlo* simulation, it was observed that the moment coefficient was not independent of the angle of attack, as theoretically expected, with

variation of value exceeding 35% difference along the angle of attack.

This significant variation contradicts the definition of the aerodynamic center and indicates that the empirical location was not sufficiently accurate. It is therefore necessary to recalibrate the position of the aerodynamic center with *DARTFlo*. The evolution of the moment coefficient at the aerodynamic center with respect to α is shown in Fig. 5.1.3. As the moment coefficient varies by less than 4%, this variation is considered negligible, and $C_{m,AC}$ is therefore assumed to be constant at this new position.

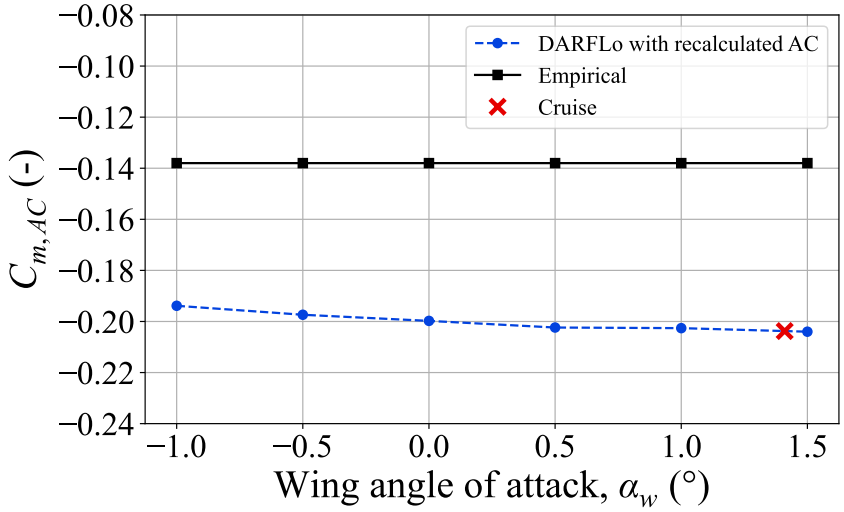

Figure 5.1.3: Moment coefficient at the aerodynamic center with respect to the wing angle of attack, computed under the conditions listed in Tab. 5.1.1, using both the empirical and the updated position of the aerodynamic center calculated with *DARTFlo*.

The *DARTFlo* AC position and its corresponding moment coefficient are summarized in Tab. 5.1.3. These updated values have been used throughout the subsequent analyses, replacing the initial empirical estimate. As with the computation of $C_{L_{\alpha w}}$, the use of *DARTFlo* provides a more accurate representation of the physics of the problem.

AC cord (ft)	X_{AC} (ft)	Y_{AC} (ft)	$C_{m,AC}$ (-)
9.76	4.06	24.49	-0.204

Table 5.1.3: Updated characteristics of the aerodynamic center calculated with *DARTFlo*

Lift distribution on the wing

The lift coefficient distribution along the wingspan has been also computed using *DARTFlo*. Several spanwise sections has been extracted, and for each of these slices, the pressure coefficient distribution along the airfoil has

been obtained. From these values, the local lift coefficient has been determined by integrating the pressure difference between the intrados and extrados of the airfoil at each section.

The distribution of the lift and the lift coefficient along the span are shown in Fig. 5.1.4. It is compared to the ideal elliptical distribution, which represents the theoretical optimum for minimizing induced drag. The resulting distribution deviates from the ideal case on both graphs, which is expected since the aircraft does not have an elliptical platform and is not operating at the optimal lift-to-drag ratio, as discussed in Sect. 4.1.2 and Sect. 5.1.2. Under such conditions, the lift distribution adjusts to other aerodynamic constraints, leading to a non-elliptical, yet still efficient, shape. Nevertheless, the distribution remains fairly close to the ideal case, mainly due to the wing taper ratio of 0.3, which helps achieving an elliptical-like distribution even without an elliptical planform. As shown in Fig. 5.1.4 b), the wing having a variable chord along the span due to the taper ratio, the distribution of the empirical lift coefficient and with *DARTFlo* do not follow an elliptical shape, unlike the empirical lift distribution.

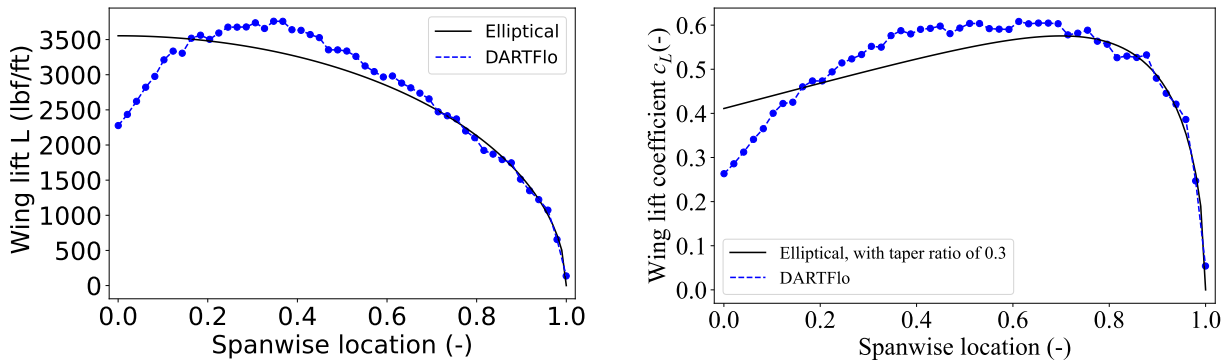

(a) Wing lift along the span

(b) Wing lift coefficient c_{L_w} along the span

Figure 5.1.4: Wing lift distribution along the span computed at conditions listed in Tab. 5.1.1 at $\alpha = 1.42°$.

5.1.2 Drag analysis

The drag study has been evaluated using Appendices F and G of Torenbeek's book [39] for both cruise and low-speed configurations (corresponding to takeoff and landing). This analysis is based on several assumptions. First, flight speeds are limited to subcritical Mach numbers. Then some criteria are defined for the wing geometry in order to ensure wings with attached flow at small angles of attack and full leading edge suction. Airplane drag can be subdivided into the following components:

- **Vortex-induced drag:** This contribution corresponds to the pressure drag caused by the formation of wing tip vortices. Indeed, these vortices generate a downwash effect, which reduces the effective angle of attack and increases the total drag. In order to use the classical potential flow theory, each main airplane part is

considered as an isolated body.

- **Profile drag:** The profile drag is defined as the skin friction and pressure drag due to the boundary layer and limited regions of separation. This part is caused by the interaction between the air and the wetted area of the aircraft (which only includes the parts exposed to the flow). The components are considered to be smooth streamline bodies and some corrections are made. The calculation of the profile drag is made based on the friction coefficient C_F of a flat plate with the assumption of fully-turbulent boundary layer. This assumption is done by evaluating the evolution of the Reynolds number along the wing, which is $\geq 10^6$ [17]. Therefore, this parameter is given by the following formula:

$$C_F = \frac{0.455}{\log_{10}(Re)^{2.58}}, \tag{5.1.1}$$

  where C_F is the friction coefficient and Re is the Reynolds number.

- **Interference effects:** It corresponds to corrections used to represent the interaction of the flow field around the airplane parts. This contribution can be negative. Indeed, the interactions between the different parts of the airplane can result in a beneficial aerodynamic effect.

- **Drag due to protuberances, surface imperfections and other extras:** This contribution includes several sources of drag that cannot be represented in the categories mentioned previously.

Drag polar

The drag polar is a curve that represents the correlation between the drag and the lift of an aircraft. To compute the total drag, the component drag is computed for each aircraft part (mainly the wing, fuselage, tail, and nacelles). This parameter is given by: $C_{D_j} = A_j + B_j C_L + D_j C_L^2$. With the gross wing area S and the drag area of each component $(C_D S)_j$, the total drag can thus be given by the following formula:

$$C_D = \sum_j C_{D_j} = \frac{\sum (C_D S)_j}{S} = A + BC_L + DC_L^2, \tag{5.1.2}$$

where A, B and D are constants. By determining these constants, the drag polar has been represented in Fig. 5.1.5.

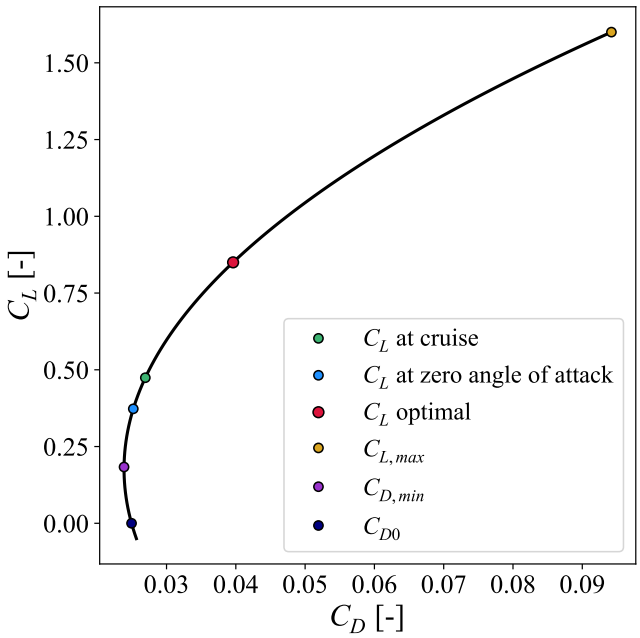

Figure 5.1.5: Drag polar representing the correlation between C_L and C_D in cruise conditions ($M = 0.9$).

The behavior of this curve is completely determined by the A, B, and D constants. The negative value of B is the reason why the minimum drag $C_{D_{min}}$ is less important than the zero-lift drag C_{D_0}.

From the drag polar, the Oswald efficiency number e can be found using a linear regression: $e = 0.80$. This correction factor represents the change in drag with lift of a three-dimensional aircraft, with respect to an ideal wing with the same aspect ratio and an elliptical lift distribution. This ratio decreases with the flight speed. For conventional aircraft flying in subsonic conditions, this factor ranges between 0.7 and 0.85 [29].

In Fig. 5.1.5, several points are represented. The green one represents the lift coefficient in cruise condition. This value does not match the optimal lift coefficient, which corresponds to the C_L value with the best lift-to-drag ratio. The evolution of this ratio is represented in Fig. 5.1.6. The distance between the two points can be explained by the important span. Indeed, the wing has a large surface in contact with the air flow, which contributes in the skin friction drag. Therefore, the profile drag increases and the lift-to-drag ratio becomes less important, as shown in Fig. 5.1.7a.

To get closer to the optimum, there are two solutions. First, by reducing the aspect ratio, the optimum value could correspond to the actual aircraft lift-to-drag ratio. However, it implies an airfoil change which would not correspond to the flight speed requirements. If the lift-to-drag curve is not modified, increasing the lift-to-drag to catch up the optimum would lead to stall conditions, which are not desired. Henceforth, the position of the actual lift-to-drag ratio appears to be interesting, but will be discussed in Sect. 7. For classic business jets, the value of

this ratio is around 15 [39]. In this specific configuration, $L/D = 18.2$, which is a non-negligible increase. As it can be observed in Fig. 5.1.6, the aircraft design does not fly in optimal conditions. It can be explained by the high aspect ratio that involves specific wing surface, chord, design lift coefficient, etc. and the flying conditions. A discussion about the aspect ratio will be detailed in Sect. 7.

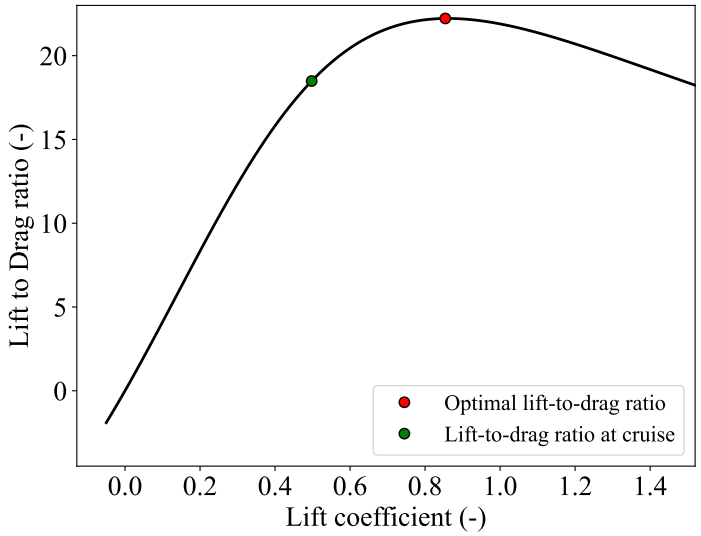

Figure 5.1.6: Evolution of the lift-to-drag ratio as a function of the lift in cruise conditions ($M = 0.9$).

Cruise

Based on the relations established earlier, the total drag coefficient C_D can be found with the lift coefficient C_L determined in Sect. 4.1.2. In Tab. 5.1.4, the lift and drag coefficients are given for cruise conditions.

	C_L (-)	C_D (-)
Cruise	0.49	0.027

Table 5.1.4: Lift and drag coefficients in cruise conditions ($M = 0.9$)

In Fig. 5.1.7a, the contribution of the various drag components has been represented. These results can be explained by the aircraft geometry. Since the wing span is more important than conventional airplanes, the implication of wing tip vortices becomes less significant. Moreover, the large span implies an important interaction between the wing and the air flow. As explained previously, the profile drag is thus increased and becomes the leading drag component. It can be noted that the interference drag has a negative contribution that is too small to not be negligible.

In Fig. 5.1.7b, the contribution of each aircraft part for the total drag is established. According to what has been explained, the wing drag is the most important source of drag. The fuselage and tail also have a non-negligible impact, in contrast to the nacelle.

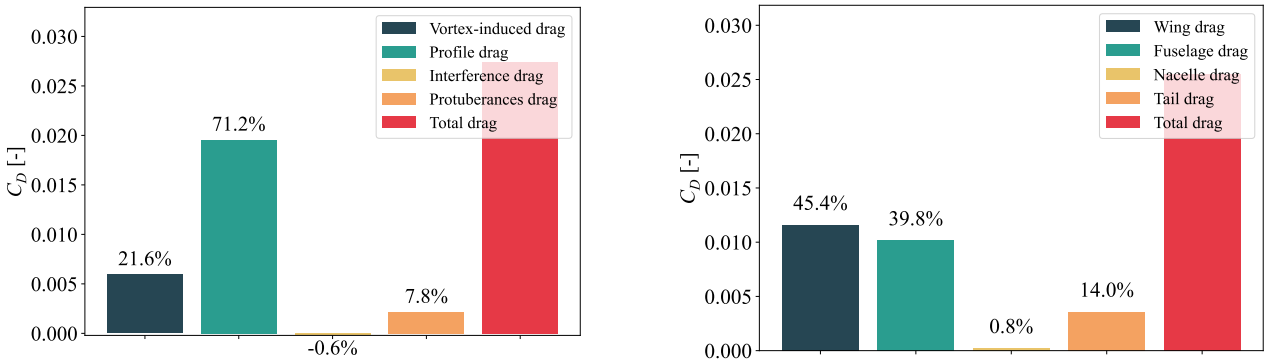

(a) Contribution of the drag components

(b) Contribution of the main aircraft parts

Figure 5.1.7: Contributions in cruise conditions ($M = 0.9$)

Performance configuration

Although the aerodynamic drag analysis was conducted with high precision and detail, a simplified but consistent drag model is required for performance estimation across all altitudes and Mach numbers. A common approach to account for the effects of air density on the parasite drag coefficient C_{D0} is to vary the constant term A of the parabolic polar law according to:

$$A(h) = A_{\text{ref}} \left(\frac{\rho(h)}{\rho_{\text{ref}}} \right)^n \tag{5.1.3}$$

This approximation reflects the dependence of C_{D0} on the Reynolds number, which decreases with altitude due to the drop in air density. This method has been used and validated in multiple academic sources, including Al-Obaidi & Moo (2017), Shahid et al. (2017), and the scaling strategies applied by NASA in high-altitude aerodynamic extrapolations [27, 37, 36].

The exponent n was then identified by fitting the computed C_{D0} values as a function of $\rho(h)$, yielding the best match with the observed drag variations. This allowed the corrected model for $A(h)$ to be defined with a data-driven exponent n.

In addition, drag polars were generated at a fixed altitude for several Mach numbers. These were used to derive Mach-dependent polynomial fits for the B and D coefficients of the drag polar:

$$C_D(CL, M) = A(h) + B(M) \cdot CL + D(M) \cdot CL^2 \tag{5.1.4}$$

Such Mach-dependent parametrizations of the polar are consistent with techniques employed in modern aerodynamic performance databases and predesign studies

Low-speed configuration

The low-speed configuration is divided into two distinct phases: takeoff and landing. As explained in Sect. 4.4.2, two-slot Fowler flaps are necessary to ensure the requirements. The sizing of these control surfaces realized in this previous section is needed to determine the flying parameters in the low-speed configuration.

The low-speed configuration induces an increase in both lift and drag. Indeed, the lift should be increased to meet takeoff requirements, and the drag should be sufficient to stop the aircraft momentum during the landing (the takeoff and landing requirements are discussed in Sect.1. In Tab. 5.1.5, the lift and drag coefficients are listed for both takeoff and landing.

	C_L(-)	C_D(-)
Takeoff ($M < 0.3$)	1.51	0.067
Landing ($M < 0.3$)	2.01	0.126

Table 5.1.5: Lift and drag coefficients in low-speed configurations ($M < 0.3$)

In Fig. 5.1.8, it can be observed that the vortex-induced drag becomes more important than the profile drag. This variation comes from the low-speed configuration and the increase in lift. Indeed, the lift augmentation creates a more important pressure difference between the upper and the lower surfaces, which involves more wing tip vortices. Moreover, since the aircraft is flying close to the ground, ground effect must be taken into account. The reduced distance between the wing and the ground alters the wingtip vortex structure, decreasing the induced drag. As a result, lift is increased and drag is reduced. However, the results obtained have shown that the ground effect has a negligible effect on coefficients (around 10^{-4}). Finally, in the low-speed configuration, two other types of drag are taken into account: the trim drag and the undercarriage drag that correspond to protuberances.

As can be observed in Tab. 5.1.5 and in Fig. 5.1.8, the variation of coefficients is more important in landing than in takeoff. It comes from the geometry of control surfaces that is different due to the respective requirements, especially for their angle of deflection and their respective area.

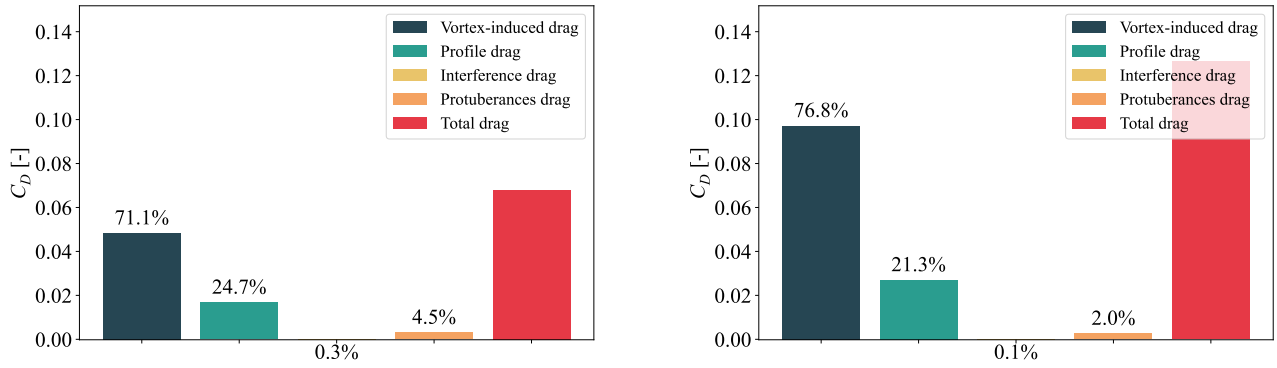

(a) Takeoff **(b)** Landing

Figure 5.1.8: Contribution of drag components in low-speed configuration ($M < 0.3$)

Comparison with *DARTFlo*

In this section, to ensure a meaningful and consistent comparison, only the drag of the wing from the drag study is considered, as *DARTFlo* only computes pressure drag of the wing. Contributions from other parts of the aircraft are excluded.

Looking at Fig. 5.1.9, it can be observed that the drag predicted by *DARTFlo* tends to overestimate the drag compared to the drag obtained with the empirical correlations. The difference comes from the assumptions and the drag components considered by both methods.

On one hand, *DARTFlo* makes the assumption of an inviscid flow, neglecting viscous effects, but it accounts for pressure drag, decomposed as wave drag and induced drag. However, it neglects viscous effects such as skin friction, which in reality would reduce shock strength and slightly mitigate pressure drag. On the other hand, empirical correlations used in Torenbeek's book make the assumption of a fully turbulent flow in order to estimate the profile drag while not explicitly accounting for wave drag.

It can also be seen that the drag predicted by *DARTFlo* exhibits a clear quadratic trend with respect to the angle of attack. This behavior is expected, as both induced and wave drag vary with the square of the lift coefficient ($C_D \propto C_L^2$). Under inviscid flow assumptions, wave drag is increasing without being reduced by the viscous effects that are not taken into account explaining that quadratic rise.

As a result, the empirical method may underestimate the drag due to the lack of wave drag modeling, while *DARTFlo* overestimates it by neglecting viscous effects that in practice reduce wave and induced drag, especially

near transonic speeds.

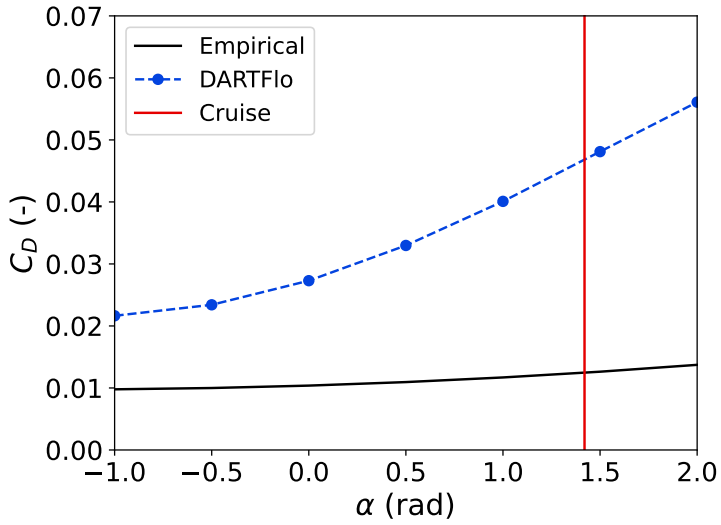

Figure 5.1.9: Evolution of the wing drag coefficient from *DARTFlo* and drag study with the angle of attack computed at conditions listed in Tab. 5.1.1.

Using Fig. 5.1.2 and 5.1.9, the Oswald efficiency number of the wing can be determined and compared with the one derived from the drag study. The results can be found in Tab. 5.1.6. In comparison with the empirical drag study, the value is significantly lower.

It can be explained by the overestimation of the shock intensity that comes from the assumption of inviscid flow. Indeed, dissipative mechanisms such as boundary layer effects, turbulence, and air viscosity are not captured. However, these phenomena help smooth out the flow and reduce pressure gradients, which can decrease the induced drag. As a result, the *DARTFlo* inviscid model attributes a lower aerodynamic efficiency to the wing, leading to a lower Oswald efficiency number.

In subsonic flow, for conventional aircraft with flaps retracted, the Oswald efficiency number typically ranges between 0.7 and 0.85 [29]. A lower coefficient, around 0.5, is more characteristic of supersonic speeds. Therefore, obtaining a value of $e = 0.3$ puts forward that *DARTFlo* may be overestimating shock effects and simulating conditions at a higher Mach number than expected in certain regions.

	DARTFlo	Drag study	Relative error
Oswald factor, e	0.314	0.83	60.75 %

Table 5.1.6: Comparison of Oswald efficiency number between *DARTFlo* and the drag study

In conclusion, the assumptions behind *DARTFlo* and the empirical drag estimation tend to lead to an overes-

timation and an underestimation of the actual drag, respectively. Despite its limitations, the drag study method is retained for the rest of this report, because the shock intensity given by the inviscid assumption associated with the consideration of the wave drag represents supersonic considerations and is overestimated.

Final selection

The Tab.5.1.7 resumes the different values computed in the Aerodynamics section. The last column of the table recalls which method is the more reliable and which value has been kept for the other studies.

	Empirical	DARTFlo	Retained value
$C_{L\alpha w}$ (rad^{-1})	6.21	7.52	*DARTFlo*
C_D at cruise (-)	0.027	0.04811	Drag study
C_{D_0} (-)	0.025	0.0176	Drag study
e (-)	0.83	0.314	Drag study
$C_{m_{AC}}$ (-)	-0.138	-0.204	*DARTFlo*
AC position (ft)	(4.66; 26.32; 0)	(4.06; 24.49; 0)	*DARTFlo*

Table 5.1.7: Summary of calculated aerodynamic values with DARTFlo and drag study with the final retained value.

5.2 Weight and Center of gravity

In this section, the weight and center of gravity of each component are evaluated. It is essential in order to determine further the stability. The weight of each component is computed using the CAD modeling, empirical relation of the Raymer's book [29], and manufacturer data. Similarly, the center of gravity (CG) of each component is calculated, with the position of some component being adjustable to meet stability requirements. In Tab. 5.2.1, x_{CG} is the longitudinal position starting from the nose of the aircraft and y_{CG} is the height of the center of gravity starting from the lower surface of the fuselage. Therefore, the Maximum TakeOff Weight (MTOW) and the center of gravity of the aircraft can be determined thanks to the CAD model.

Component	Weights (lb)	x_{CG} (ft)	y_{CG} (ft)
Fuel	45798	41	9
Wing	17991	38	10
Horizontal tail	1299	111	27
Vertical tail	1126.81	100	16
Propulsion	10018	34	5
Fuselage	14983	50	5
Nose landing gear	1391	3	0.5
Main landing gear	3932	17	0.5
Equipment	4675	42	6
Hydromechanical system of control surfaces	1474	75	5
Payload	3042	53	5
MTOW	113881	38.94	7.11

Table 5.2.1: Weight and center of gravity of each component of the aircraft (full payload and maximum fuel).

5.3 Stability

In order to ensure that the Infinity Jet can maintain safe and controllable flight through its missions, a detailed analysis of the stability was carried out. This step is of the uttermost importance as it verifies if the aircraft responds appropriately to disturbances and that it returns to steady flight without requiring excessive control effort.

The stability analysis is divided into two main parts. The static stability section focuses on the initial tendencies of the aircraft when it is disturbed from equilibrium. The dynamic stability section goes further by simulating how these disturbances evolve over time, and whether they damp out or grow.

Several configurations have been investigated to reflect real operating conditions, including :

- Clean cruise,
- Takeoff and Landing with flaps extended,
- One engine inoperative (OEI) scenario.

To carry out this analysis, the USAF DATCOM [40] handbook was used to compute aerodynamic derivatives.

The following sections summarize the methods, key results and interpretations of each configuration, supported by tables and figures.

5.3.1 Static stability

Static stability refers to the aircraft's initial tendency to return to its original flight condition after a small disturbance. If it tends to return to its original position without position input, it is said to be statically stable. This property is essential for ensuring the aircraft can recover from minor perturbations without requiring continuous corrective action. In the context of preliminary design, analyzing the static stability helps verify whether the aircraft configuration offers sufficient inherent stability in pitch, yaw and roll, which is influenced by the overall geometry, control surface sizing and center of gravity location.

Methodology

The static stability of the aircraft was assessed by computing stability derivatives using empirical methods from the USAF DATCOM [40]. These well-established techniques allow for the estimation of aerodynamic derivatives based on geometry and flow conditions. While they are simplified compared to high-fidelity simulations, DATCOM methods are particularly suitable for early design phases and provide results consistent with classical aerodynamic theory.

These derivatives quantify how the aerodynamic forces and moments vary with small changes in angles and rates, and they form the foundation for evaluating static stability.

For each of the studied configurations, the aircraft geometry and flight conditions were used to compute relevant coefficients. In particular, three derivatives, $C_{M\alpha}$, $C_{N\beta}$ and $C_{L\beta}$, were used as key indicators of static pitch, yaw and roll stability respectively.

The signs and the magnitudes of these derivatives were analyzed to determine whether the aircraft naturally tends to return to equilibrium after small disturbances, without considering time-dependent effects. These effects were considered for the dynamic stability.

Results and Discussion

In order to assess the static stability of the Infinity Jet, three key aerodynamic derivatives have been evaluated :

- $C_{M\alpha}$: the pitching moment coefficient derivative with respect to angle of attack. A negative value indicates longitudinal static stability, meaning the aircraft tends to naturally pitch down when perturbed upward.

- $C_{N\beta}$: the yawing moment coefficient derivative with respect to sideslip angle. A positive value indicates directional static stability - also referred as weathervane stability -, where the aircraft tends to align itself with the relative wind.

- $C_{L\beta}$: The rolling moment coefficient derivative with respect to sideslip angle. This derivative characterizes the dihedral effect, and a negative value shows lateral static stability, inducing a restoring rolling moment when the aircraft experiences a sideslip.

These derivatives provide a first-order approximation of the aircraft's inherent ability to return to equilibrium following small perturbations, without considering time-dependent effects or control inputs.

Before diving into the detailed estimation of these derivatives, it is useful to analyze the variation of the static margin, which provides a geometric interpretation of longitudinal static stability. The static margin, noted K_n, represents the distance between the center of gravity and the neutral point, normalized by the mean aerodynamic chord (MAC) :

$$K_n = h - h_0, \tag{5.3.1}$$

where h is the center of gravity location and h_0 is the neutral point. A positive static margin indicates a statically stable configuration. Since the longitudinal position of the CG varies with the missions requirements (payload) and the flight traveling (fuel consumption), the longitudinal stability must be evaluated in every configuration, from the most to the less stable case. In order to have both acceptable stability and maneuverability, this parameter is fixed between 5% and 30%.

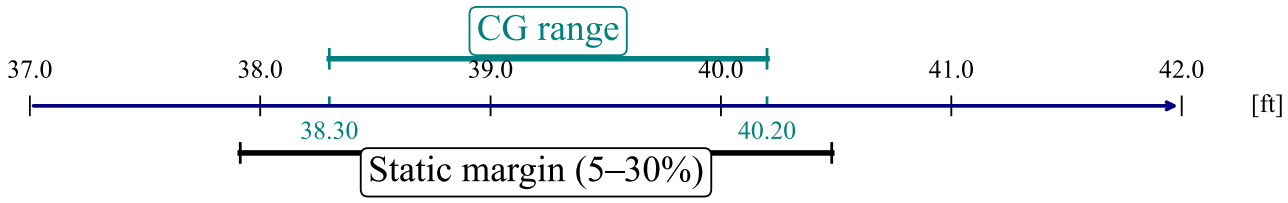

Figure 5.3.1: Longitudinal CG envelope and static margin limits

The Fig. 5.3.1 confirms that, geometrically, the *Infinity Jet* exhibits longitudinal static stability throughout its operational center of gravity range. While the static margin provides a useful geometric criterion for pitch stability, a more comprehensive assessment is captured by the $C_{M\alpha}$ expression.

The following expressions, based on the USAF DATCOM methodology, were used to estimate the key aerody-

namic derivatives.

- The pitching moment coefficient $C_{M\alpha}$ was calculated using :

$$C_{M\alpha} = (h - h_0)C_{L\alpha} - C_{L\alpha_t}V_H(1 - \frac{d\epsilon}{d\alpha}) \tag{5.3.2}$$

  where$C_{L\alpha}$ is the lift curve slope of the wing and the body, $C_{L\alpha_t}$ is the lift curve slope of the horizontal tail, V_H is the horizontal volume coefficient and $\frac{d\epsilon}{d\alpha}$ is the downwash gradient.

- The rolling moment coefficient $C_{l\beta}$ was determined from :

$$C_{L\beta} = -\frac{\pi}{4}\frac{AR}{1 + \frac{4}{AR}}\chi_{\text{eff}} \tag{5.3.3}$$

  where AR is the aspect ratio of the wing and χ_{eff} is the effective dihedral angle of the wing.

- The yawing moment coefficient $C_{N\beta}$ was estimated using :

$$C_{N\beta} = -C_{Y\beta}\frac{l_V}{b} \tag{5.3.4}$$

  where $C_{Y\beta}$ is the side force derivative with respect to sideslip, l_V is the moment arm from the center of gravity to the vertical tail and b is the wingspan. The side force derivative with respect to sideslip was found using :

$$C_{Y\beta} = -\frac{S_V}{S}C_{L_V} \tag{5.3.5}$$

  where S_V is the vertical tail area, S is the wing area and C_{L_V} is the lift curve slope of the vertical tail.

Stability derivative	$C_{M\alpha}$	$C_{N\beta}$	$C_{L\beta}$
Cruise	-2.05	0.17	–0.2
Landing	-1.61	0.16	-0.2
Takeoff	-1.56	0.16	–0.2

Table 5.3.1: Static stability derivatives in different flight configurations

The Tab. 5.3.1 summarizes the derivatives computed for three flight conditions : cruise, landing and takeoff.

In the clean cruise configuration, all three stability derivatives confirm that the aircraft is statically stable in pitch, yaw and roll. Indeed, both the $C_{M\alpha}$ and the $C_{L\beta}$ are negative while the $C_{N\beta}$ is positive, as was expected.

When analyzing the takeoff and landing configurations, the value of $C_{M\alpha}$ becomes slightly less negative. This indicates a slight reduction in longitudinal static stability. During these phases, the deployment of flaps increases the lift on the main wing and changes the downwash distribution over the horizontal tail. This altered downwash reduces the tail's stabilizing contribution, which weakens the restoring pitch moment. Despite this reduction, the derivative remains negative, meaning the aircraft still maintains a stable pitching behavior. The two other derivatives remain essentially unchanged, indicating that the directional and lateral stability are not significantly affected by flap deployment in this configuration.

5.3.2 Dynamic stability

In contrast to static stability, dynamic stability explores how the aircraft response after a disturbance evolves with time. It assesses whether oscillations grow, decay or persist, and how quickly the aircraft settles back into steady flight. This aspect is extremely important for ensuring passenger comfort, pilot workload, and compliance with handling quality standards.

The dynamic stability of the Infinity Jet was studied by modeling both longitudinal and lateral motions through state-space representations. The eigenvalues of the system matrices were analyzed to identify characteristic modes. In addition to this modal analysis, time-domain simulations were carried out to evaluate the aircraft's response to control surface inputs as well as its performance under asymmetric thrust conditions that can be encountered in the one engine inoperative (OEI) scenario.

These simulations provide further insight into the aircraft's damping characteristics, responsiveness and the efficiency of its control surfaces.

Methodology

To evaluate the dynamic stability of the Infinity Jet, both longitudinal and lateral-directional dynamics were modeled using linearized equations of motion in state-space form. These models incorporate key aerodynamic stability derivatives, computed using USAF DATCOM [40] empirical formulas based on the aircraft's geometry, aerodynamic configuration and flight conditions.

Two system matrices were constructed :

- A 4-state longitudinal matrix describing pitch-related motion, including forward velocity u, vertical velocity

w, pitch rate q and pitch angle θ.

- A 4-state lateral matrix describing yaw and roll-related motion, including sideslip angle β, roll rate p, yaw rate r and roll angle φ.

The eigenvalues of each matrix were analyzed to extract the natural modes of motion :

- Longitudinal : short period and phugoid modes,
- Lateral : Dutch roll, roll subsidence and spiral mode.

To complement the eigenvalue-based modal analysis, time-domain simulations were performed by applying step inputs on control surfaces :

- A 10° elevator deflection to study pitch dynamics,
- A 25° aileron deflection to study roll dynamics,
- A 5° rudder deflection to study yaw dynamics.

The amplitudes of these inputs were chosen in accordance with the guidelines found in MIL-F-8785C and MIL-STD-1797A [13][12]. While these standards are originally intended for military aircraft, they provide well-established references for evaluating flying qualities and control effectiveness. By using these values, the aim is not to certify the Infinity Jet according to military criteria, but rather to verify that its dynamic response under representative control inputs remains stable, predictable and consistent with good handling qualities.

Additionally, an asymmetric thrust condition was simulated to represent a one engine inoperative (OEI) case, particularly affecting yaw dynamics.

Finally, a sensitivity analysis was carried out to evaluate the robustness of the aircraft's dynamic behavior to variations in key stability derivatives. This ensured that the stability and handling qualities remain acceptable even under moderate modeling uncertainties.

Results and Discussion

The Tab. 5.3.2 summarizes the stability derivatives, found using empirical formulas from the USAF DATCOM[40], used in the longitudinal and lateral-directional models for the cruise flight condition.

Longitudinal Derivative	Value	Lateral-Directional Derivative	Value
C_{X_u}	–0.054	C_{Y_p}	0.13
C_{Z_u}	–0.4	C_{Y_r}	–0.34
C_{Z_q}	–17.26	C_{Y_β}	–0.41
C_{Z_w}	0.028	C_{L_p}	–9.3
$C_{Z_{\dot{w}}}$	–5.4	C_{L_r}	–0.34
$C_{Z_{\dot{\alpha}}}$	–10.82	C_{L_β}	–0.2
C_{M_q}	–42.5	C_{N_p}	–0.34
C_{M_w}	0.0077	C_{N_r}	–0.34
$C_{M_{\dot{w}}}$	0.1	C_{N_β}	0.17
C_{M_α}	–2.05	$C_{N_{\dot{\beta}}}$	–0.08
$C_{M_{\dot{\alpha}}}$	–26.64		

Table 5.3.2: Dynamic stability derivatives at cruise condition, sorted by axis and grouped by motion type

The Tab. 5.3.2's clarity has been improved. Also, the remaining derivatives were added. Using these derivatives, the state-space matrices describing the longitudinal and lateral-directional dynamics were constructed as follows.

$$A_{longitudinal} = \begin{bmatrix} \frac{X_u}{m} & 0 & 0 & -g \\ \frac{Z_u}{m-Z_{\dot{w}}} & \frac{Z_w}{m-Z_{\dot{w}}} & \frac{Z_q+mV}{m-Z_{\dot{w}}} & 0 \\ 0 & M_w + \frac{M_{\dot{w}}Z_w}{m-Z_{\dot{w}}} & M_q + M_{\dot{w}}\frac{Z_q+mV}{m-Z_{\dot{w}}} & 0 \\ 0 & 0 & 1 & 0 \end{bmatrix}, A_{lateral} = \begin{bmatrix} Y_\beta & Y_p + V & Y_r & g \\ L_\beta & L_p & L_r & 0 \\ N_\beta & N_p & N_r & 0 \\ 0 & 1 & 0 & 0 \end{bmatrix} \tag{5.3.6}$$

The state-space matrices include standard aerodynamic derivatives as well as the cruise speed V, the aircraft mass m and the gravitational constant g.

The longitudinal matrix A captures the dynamics related to forward motion and pitch, while the lateral matrix A reflects the behavior of sideslip, roll, and yaw.

The linearized system can therefore be written in the standard state-space form:

$$\dot{\mathbf{x}} = A\mathbf{x}$$

where **x** is the state vector.

For the longitudinal dynamics, the state vector is defined as:

$$\mathbf{x}_{\text{long}} = [u \quad w \quad q \quad \theta]^T$$

and for the lateral-directional dynamics:

$$\mathbf{x}_{\text{lat}} = [\beta \quad p \quad r \quad \phi]^T.$$

These equations describe the aircraft's natural motion in the absence of control input.

To evaluate the dynamic modes of the Infinity Jet, the eigenvalues of the state-space matrices were computed. These eigenvalues provide insight into the system's natural response characteristics: the real part indicates whether the mode is stable (negative values), and the imaginary part relates to its oscillatory behavior. In particular, the longitudinal dynamics reveal the short period and phugoid modes, while the lateral-directional dynamics exhibit Dutch roll, roll subsidence, and spiral modes.

The computed eigenvalues for both longitudinal and lateral systems are presented below.

Mode	Eigenvalue λ	Damping Ratio ζ	Natural Frequency ω_n or Time Constant τ
Longitudinal			
Short-period	$-2.52 \pm 1.3i$	0.89	2.83 rad/s
Phugoid[1]	-0.043	-	23.26 s
Phugoid[1]	0.034	-	29.24 s
Lateral-directional			
Roll subsidence	-4.93	-	0.2 s
Dutch roll	$-0.21 \pm 0.18i$	0.76	0.27 rad/s
Spiral	-0.036	-	27.62 s

Table 5.3.3: Eigenvalues and modal characteristics.

The Tab. 5.3.3 summarizes the dynamic modes of the aircraft based on the eigenvalue analysis of the linearized state-space model. The short-period and Dutch roll modes are characterized by complex eigenvalues, indicating

[1] These are not true phugoid modes, as they are non-oscillatory. The classical phugoid is a lightly damped oscillation.

oscillatory behavior. Their damping ratios and natural frequencies fall within typical observed ranges [33] [13]. The phugoid, roll subsidence and spiral modes are represented by real eigenvalues, indicating no oscillating behavior. For these modes, time constants ($\tau = \frac{1}{|Re(\lambda)|}$) are showed instead of natural frequencies.

While it is more common to observe a single complex phugoid mode, the presence of two distinct non-oscillatory eigenvalues -one stable and one slightly unstable- is not necessarily problematic. This behavior may result from sensitivity to trim conditions, numerical approximations or modeling assumptions [38]. Further investigation would be required to conclusively determine the physical nature of this unstable mode. Despite being labeled "phugoid" for classification purposes, these modes are aperiodic and do not represent true phugoid oscillations. Regardless, this unstable mode grows very slowly, allowing ample time for pilot intervention, and thus does not compromise flight safety under normal operating conditions.

The roll subsidence mode exhibits fast and stable damping, while the spiral mode is stable but converges slowly, both typical and acceptable characteristics for this type of aircraft. To further assess the aircraft's behavior, it is interesting to investigate the time-domain responses to step inputs in control surfaces, allowing us to evaluate dynamic stability and flying qualities more concretely.

To evaluate the aircraft's dynamic response to control inputs, a linearized state-space model was used with elevator, aileron, and rudder deflections as inputs. These derivatives can be found in Tab. 5.3.4.

Control Derivative	$C_{M_{\delta e}}$	$C_{L_{\delta a}}$	$C_{N_{\delta r}}$
Value	-2.43	0.34	-0.03

Table 5.3.4: Control derivatives corresponding to elevator (δ_e), aileron (δ_a), and rudder (δ_r) inputs.

Tab. 5.3.4 has been added.

$$B_{\text{longitudinal}} = \begin{bmatrix} 0 \\ 0 \\ M_{\delta_e} \\ 0 \end{bmatrix}, \qquad B_{\text{lateral}} = \begin{bmatrix} 0 & 0 \\ L_{\delta_a} & 0 \\ 0 & N_{\delta_r} \\ 0 & 0 \end{bmatrix}$$

With the inclusion of these control matrices, the full linearized system becomes:

$$\dot{\mathbf{x}} = A\mathbf{x} + B\mathbf{u}$$

where **x** is the state vector and **u** is the control input vector.

For the longitudinal model:

$$\mathbf{u}_{\text{long}} = [\delta_e]^T$$

and for the lateral-directional model:

$$\mathbf{u}_{\text{lat}} = [\delta_a \quad \delta_r]^T$$

where δ_e, δ_a, and δ_r denote the elevator, aileron, and rudder deflections, respectively.

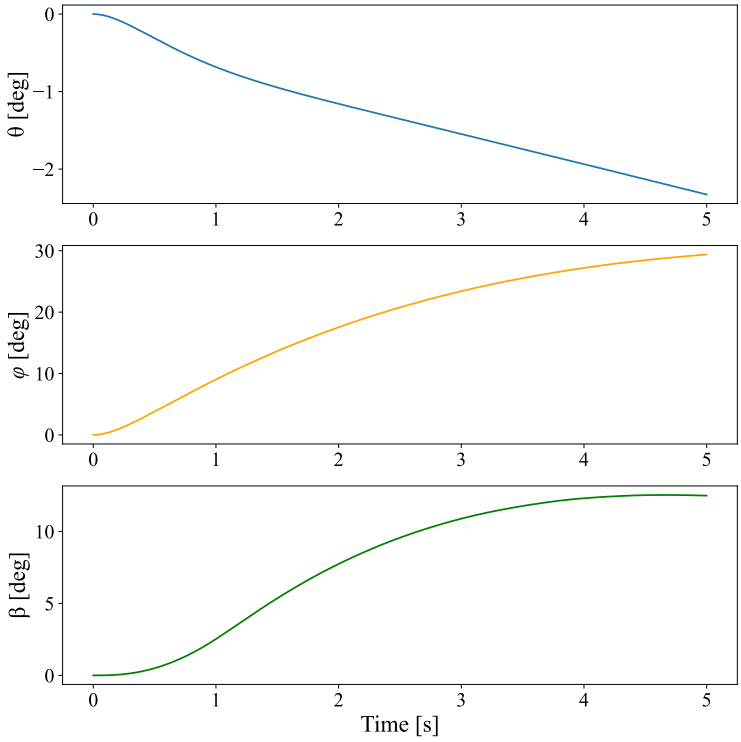

Figure 5.3.2: Pitch, Roll and Sideslip Responses to Elevator, Aileron and Rudder Step Inputs

ϕ => φ to avoid confusion with the twist angle on Fig. 5.3.2 and Fig. 5.3.3 The Fig. 5.3.2 shows the aircraft responses to different surface control inputs. The control surface deflections used in these simulations (10° for the elevator, 25° for the aileron and 5° for the rudder) were selected to produce noticeable responses. These magnitudes are consistent with values recommended in literature [33][10]. While MIL-F-8785C and MIL-STD-1797A provide guidelines for acceptable aircraft response characteristics, it is important to remember that these are tailored specifically to military aircraft operating under more responsiveness constraints [13][12]. In this context, although our aircraft does not fully meet all dynamic performance criteria set by the MIL specifications -particularly for the roll response-, it still demonstrates safe, well-damped behavior appropriate for a business jet.

Sensitivity Analysis of Stability Derivatives

The stability derivatives used in the linearized model were estimated using semi-empirical formulas from the USAF DATCOM [40]. These estimates, while widely used in preliminary design, involve simplifications and approximations. To assess the robustness of the dynamic modes to potential inaccuracies in these values, a sensitivity analysis was performed.

A small set of key aerodynamic derivatives was selected based on their dominant influence on the dynamic modes [38][33][10]:

- C_{M_α} – mostly affects short-period mode
- C_{M_q} – mostly affects short-period damping
- C_{N_β} – mostly affects Dutch roll and spiral
- C_{L_p} – mostly affects roll subsidence

Each derivative was varied individually by ±10% around its nominal value. The resulting eigenvalues were recalculated, and the most affected mode was recorded for each case. Table 5.3.5 summarizes the results.

Derivative	Variation	Affected Mode	Nominal Eigenvalue	Perturbed Eigenvalue
C_{M_α}	–10%	Short period	–2.52 ± 1.3i	–2.52 ± 1.32i
C_{M_α}	+10%	Short period	–2.52 ± 1.3i	–2.52 ± 1.28i
C_{M_q}	–10%	Short period	–2.52 ± 1.3i	–1.83 ± 1.96i
C_{M_q}	+10%	Short period	–2.52 ± 1.3i	–4.4 and –2.02[1]
C_{N_β}	–10%	Dutch roll	–0.21 ± 0.18i	–0.21 ± 0.17i
C_{N_β}	+10%	Dutch roll	–0.21 ± 0.18i	–0.21 ± 0.19i
C_{L_p}	–10%	Roll subsidence	-4.93	–4.37
C_{L_p}	+10%	Roll subsidence	-4.93	–5.48

Table 5.3.5: Effect of ±10% variation in selected stability derivatives on dominant eigenvalues.

The results in Tab. 5.3.5 highlight the sensitivity of the short-period mode to variations in C_{M_α} and particularly in C_{M_q}, which governs pitch damping. While perturbing C_{M_α} slightly shifted the natural frequency, changes in

[1] The short-period mode became overdamped, splitting into two distinct real eigenvalues.

C_{M_q} significantly affected the damping characteristics. A +10% increase in C_{M_q} caused the short-period mode to become overdamped, resulting in two separate real eigenvalues. While this behavior remains stable and even leads to faster decay, the loss of oscillatory dynamics implies a more sluggish and less responsive pitch feel, potentially degrading handling qualities. The Dutch roll and roll subsidence modes showed minor sensitivity to changes in C_{N_β} and C_{L_p}, confirming that the overall dynamic stability is robust to moderate uncertainty in these derivatives. The phugoid mode was not included in this sensitivity study, as it remained non-oscillatory in the nominal model and is known to be weakly sensitive to small variations in the dominant aerodynamic derivatives [10] [38]. The spiral mode, typically weakly stable and slow, was not significantly affected by the derivative variations tested and therefore was also not included in this study.

One Engine Inoperative (OEI) Condition

To evaluate the dynamic stability of the aircraft in asymmetric thrust conditions, a scenario with one engine inoperative (OEI) was simulated. The loss of one engine generates a yawing moment due to asymmetric thrust, modeled here as an additional contribution to the yaw rate derivative. The control input considered is still a 5° rudder step.

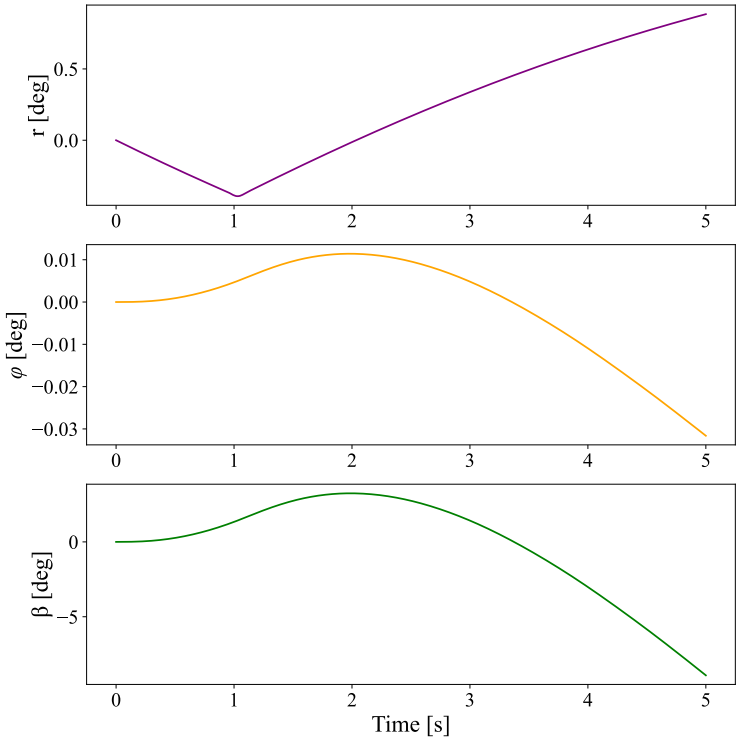

Figure 5.3.3: Yaw rate, Roll and Sideslip Responses to Rudder Step Input (OEI)

The Fig. 5.3.3 shows the aircraft's dynamic response in sideslip angle β, yaw rate r, and roll angle φ. The yaw rate was shown here rather than the pitch angle because the OEI scenario primarily affects the aircraft's lateral-directional dynamics. Despite the asymmetric thrust, the aircraft exhibits manageable behavior in the early seconds following engine failure. Indeed, the responses are evolving at a slow rate, allowing the pilot to adjust the flight conditions appropriately. These results suggest that the aircraft maintains stable flight characteristics in the OEI configuration.

5.4 Structure

The structural design phase is undertaken to ensure that the aircraft is capable of withstanding the various loads encountered throughout its operation. In this section, the key steps and methods by which the internal framework of the ultra-luxurious private jet is defined are described. The process is initiated with the evaluation of critical flight conditions through the construction of a Placard diagram and the establishment of the flight envelope. Once these parameters are determined, aerodynamic and structural loads are calculated, particularly for the wing root and the rear fuselage. Based on these loads, the primary structural elements such as spars, ribs, frames, stringers, and skin panels are sized using a comprehensive analytical approach. Finite element analysis is then performed to refine and validate the design, the results of the analytical part.

5.4.1 Placard diagram

The placard diagram of the *Infinity jet* can be seen on Fig. 5.4.1, it highlights the evolution of the aircraft velocity with respect to altitude. In order to build this diagram, the design cruise speed must first be identified. For each altitude, the available thrust is computed at maximum engine power, and the corresponding velocity at which thrust equals drag is determined. This velocity represents the upper bound of steady cruise performance, as the aircraft cannot maintain level flight at a higher speed under these conditions.

Above the design cruise altitude, the aircraft typically operates at a constant Mach number M_c. However, below this altitude, maintaining a constant drag profile becomes essential. Since aerodynamic drag varies with air density, the true airspeed must decrease at lower altitudes to preserve this equilibrium

It is also necessary to consider the design dive velocity V_D, which represents the maximum attainable speed during a steep descent. The associated dive Mach number M_D is defined as the minimum between:

$$M_D = \min(M_{D1}, M_{D2}) \ . \tag{5.4.1}$$

Here, $M_{D1} = 1.25M_c$ is a conventional regulatory limit, while M_{D2} corresponds to the Mach number reached after a 20-second dive at a 7.5° angle, followed by a 1.5-g pullout. This value is typically computed using a dynamic simulation of the aircraft's acceleration during the dive phase.

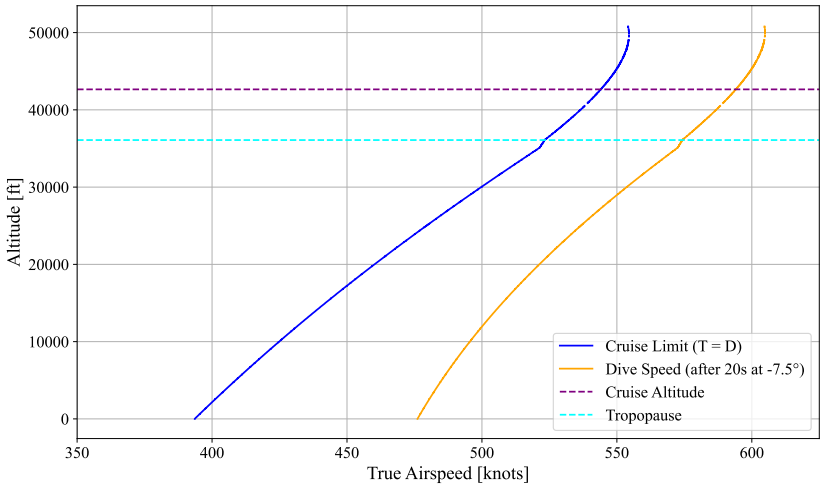

Figure 5.4.1: Infinity Jet's placard diagram illustrating the cruise speed boundary (V_C) defined by the equilibrium condition $T = D$, and the dive speed limit (V_D) derived from a 7.5° dive trajectory sustained for 20 seconds.

5.4.2 Flight envelope

The flight envelope illustrates the variation of the load factor as a function of the equivalent airspeed. Its construction was carried out in accordance with the Federal Aviation Regulations, specifically paragraphs §25.333 to §25.341, which define the requirements for maneuvering and gust loads applicable to transport category aircraft [1]. Fig. 5.4.2 presents the flight envelope of the Infinity jet at its cruise altitude of 42,650 ft. This envelope combines two distinct boundaries: the maneuver envelope, driven by controlled flight inputs, and the gust envelope, which reflects the structural response to atmospheric turbulence. The maneuver envelope is bounded by the maximum and minimum allowable load factors, which, in the case of the Infinity Jet, are governed by the Federal Aviation Regulation (FAR §23.337 for normal category airplanes) and depend on the aircraft's weight [1]. These values are defined as:

$$n_{\min} = -1, \qquad n_{\max} = 2.5, \tag{5.4.2}$$

The stall curves define the upper and lower limits of the maneuver envelope, corresponding to the maximum load factors before stall occurs in cruise (positive) and landing (negative) conditions. They are computed as a function

of equivalent airspeed using the following relation :

$$n = \frac{L}{W} = \frac{\rho_0 V_e^2 S C_{L,max}}{2W}, \tag{5.4.3}$$

where ρ_0 is the air density at sea level, V_e the considered equivalent airspeed, S the wing area, $C_{L,max}$ the maximum lift coefficient and W the weight of the Infinity jet. The gust envelope complements the maneuver envelope and accounts for the impact of sudden vertical gusts acting on the aircraft. It is constructed by introducing the equivalent gust velocity U_e, which is derived from statistical data and varies with both the flight altitude and the aircraft's speed. To model the structural response, two parameters are introduced: the airplane weigh ratio μ and the gust alleviation factor F :

$$\mu = \frac{2W}{\rho C_{L\alpha,plane} c g S}, \tag{5.4.4}$$

$$F = \frac{0.88\mu}{5.3 + \mu}, \tag{5.4.5}$$

$$n_{gust} = 1 + \frac{F C_{L\alpha,plane} U_e V_e S}{498W}, \tag{5.4.6}$$

where $C_{L\alpha,plane}$ is the lift curve slope, c the mean aerodynamic chord, g the gravitational acceleration.

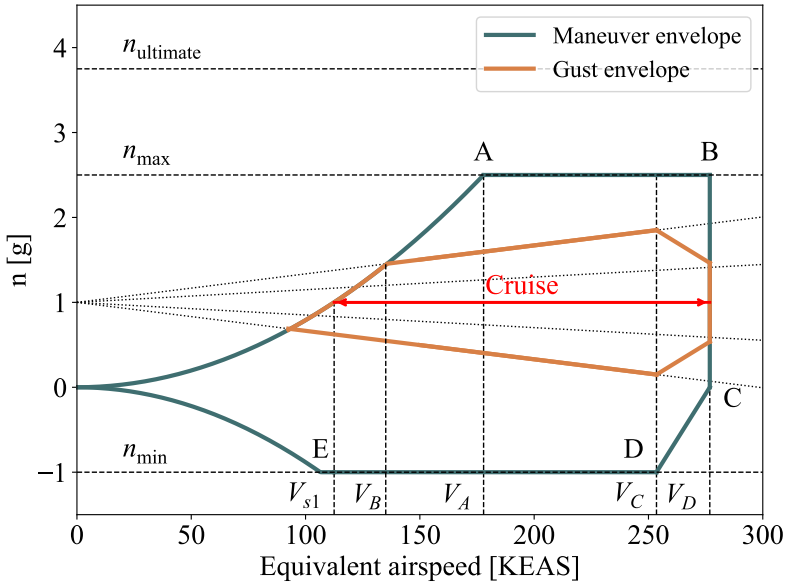

Figure 5.4.2: Infinity jet's maneuver envelope and gust envelope at the altitude 42,650 ft.

The flight envelope is characterized by a set of key reference speeds. V_A corresponds to maximum velocity at which maximum deflection of controls is authorized. This speed is computed from the stall speed V_{s1}. It's defined

as $V_{s1} = \sqrt{\frac{2W}{\rho_0 C_{L,max} S}}$ and $V_A = \sqrt{n_{max}} V_{s1}$. V_B is the equivalent minimum speed to enter in a just region. V_C represents the equivalent design cruise speed, while V_D corresponds to the equivalent maximum dive speed, beyond which the aircraft is not certified to operate. Two key design load factors are considered in the structural sizing of the aircraft. The first, referred to as the limit load factor n_{limit}, is equal to the maximum load factor n_{max} that the aircraft is expected to experience under normal operating conditions. Beyond this, the structure must also withstand the ultimate load factor $n_{ultimate} = 1.5 n_{limit}$ without failure for at least three seconds.

The most relevant flight data of the envelope are summarized in Tab. 5.4.1 and 5.4.2 below.

Parameter	Velocities V or load factor n	Value (KEAS)
Stall speed	V_{stall}	107.8
Turbulence penetration speed	V_B	135.1
Design maneuvering speed	V_A	177.9
Design cruise speed	V_C	256.1
Design dive speed	V_D	278.3
Minimum load factor	n_{min}	-1
Maximum load factor	n_{max}	2.5
Limit load factor	n_{limit}	2.5
Ultimate load factor	$n_{ultimate}$	3.75

Table 5.4.1: Summary of characteristic speeds and load factors.

Critical points	Velocities (KEAS)	Load factors (-)
A	177.9	2.5
B	278.3	2.5
C	278.3	0
D	256.1	-1
E	107.8	-1

Table 5.4.2: Critical points of the flight envelope.

5.4.3 Aerodynamic loads

This section focuses on identifying and quantifying the aerodynamic loads acting on the aircraft under the most critical flight conditions defined in the envelope. Based on the representative geometry of the aircraft with the relevant forces is represented in Fig. 5.4.3 and the critical points summarized in Tab. 5.4.2, the relevant forces and moments will be evaluated.The force L_{wing} represents the lift generated by the wing, applied at its aerodynamic center, while L_{tail} is the lift produced by the horizontal tail. D_{wing} and D_B denote the drag forces from the wing and rear fuselage, respectively. The term nW corresponds to the apparent weight due to load factor, acting downward at the center of gravity. T represents the engine thrust, oriented forward. Each distance d_i is the moment arm between the force i and the center of gravity, used for moment balance.

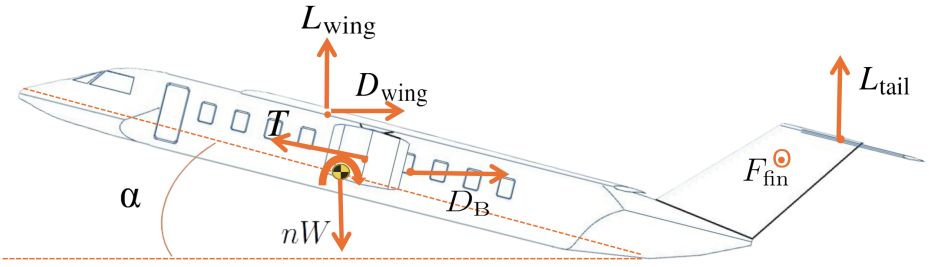

Figure 5.4.3: Aerodynamic loads.

The determination of aerodynamic loads relies on solving a system of two equations representing the aircraft's equilibrium in the vertical direction and in pitching moment. To solve this system, an iterative process is implemented. The governing equations are the following:

$$\begin{cases} nW = L_{\text{wing}} + L_{\text{tail}} + T\sin(\alpha - i_{\text{w}}), \\ I_\theta \ddot{\theta} = d_{\text{L}} L_{\text{wing}} + d_{\text{D}} D_{\text{wing}} + d_{\text{B}} D_{\text{B}} - d_{\text{tail}} L_{\text{tail}} - d_{\text{trust}} T + M, \end{cases}$$

where i_{w} is the incidence angle between the root of the wing and the fuselage axis, I_θ the moment of inertia of the fuselage around the center of gravity (computed through the CAD study), M the pitching moment (positive clockwise) and $\ddot{\theta}$ the pitching acceleration (calculated by FAR 25.331) :

$$\ddot{\theta} = \frac{39n}{V_e}(n - 1.5). \tag{5.4.7}$$

The iteration is performed over the angle of attack α, which influences both lift components. At each step, the

two equilibrium conditions are evaluated, and the system is solved. The only unknowns in this formulation are the wing lift L_{wing} and the tail lift L_{tail}. The load of the fin can be computed considering the maximum yaw angle ψ of 15° (from FAR 25 [11]) :

$$F_{\text{fin}} = \frac{1}{2}\rho_0 V_e^2 S_{\text{tail}} a_{\text{tail}} \psi, \tag{5.4.8}$$

where S_{tail} is the surface of the horizontal tail and a_{tail} the slope of the lift curve of the horizontal tail. The Tab. 5.4.3 summarizes the loads obtained for each critical point.

Point	V_e (KEAS)	α (°)	L_{wing} (lbf)	L_{tail} (lbf)	F_{fin} (lbf)	M_{fus} (lbf ft)
A	177.9	14.59	299 356	–36 779	24 142	318 016
B	278.3	3.00	295 350	–26 489	58 174	767 994
C	278.3	–3.43	3 604	–905	58 174	767 994
D	256.1	–6.34	–81 423	–22 561	47 915	632 101
E	107.8	–11.50	–45 168	–55 719	8 490	111 737

Table 5.4.3: Summary of forces and moments for each critical point.

5.4.4 Structural load

Wing

In this part, the structural loads acting at the wing root are evaluated for each critical flight condition. The analysis is conducted in a local reference frame, whose origin is set at the leading edge of the wing root. The x-axis is directed along the chord, the y-axis along the span, and the z-axis is oriented downward. To perform this evaluation, the following forces and moments are considered:

- The aerodynamic lift L_{wing} and drag D_{wing}, applied at the aerodynamic center $(x_{\text{ac}}, y_{\text{ac}}, z_{\text{ac}})$,
- The wing's structural weight W_{wing}, acting at its center of gravity $(x_{\text{cg}}, y_{\text{cg}}, z_{\text{cg}})$,
- The engine weight W_{eng}, applied at the engine's center of gravity $(x_{\text{eng}}, y_{\text{eng}}, z_{\text{eng}})$,
- The aerodynamic moment M_{wing}, acting around the aerodynamic center.

Since critical load cases are being analyzed, the fuel weight is neglected, as it generally offsets a portion of the lift and reduces the net structural loading on the wing. Because only half of the aircraft (i.e., a single wing) is being

considered in this analysis, all forces and weights are divided by two. This assumption is valid due to the symmetry of the win. The structural loads at the root are then obtained by enforcing equilibrium in both vertical forces and moments. The resulting system of equations is given below and the Tab. 5.4.4 summarized the results. The shear forces T_x, T_y and T_z are applied at the aerodynamic center of the wing profile ($\approx$ the quarter chord of the wing profile).

Point	T_x (10^3 lbf)	T_y (lbf)	T_z (10^3 lbf)	M_x (10^3 lbf ft)	M_y (10^3 lbf ft)	M_z (10^3 lbf ft)
A	–24.83	0.0	142.84	–3 973.91	–684.87	1 199.28
B	–0.65	0.0	142.82	–3 976.86	–699.04	381.09
C	3.45	0.0	1.28	–39.25	–41.33	86.12
D	–1.72	0.0	–39.15	1 099.89	152.62	215.31
E	–3.46	0.0	–20.68	601.91	89.26	156.57

Table 5.4.4: Reaction forces and moments at the wing root for each critical flight case.

$$
\begin{cases}
T_x = \left(-\dfrac{L_{\text{wing}}}{2} + \dfrac{nW_{\text{wing}}}{2} + \dfrac{nW_{\text{eng}}}{2}\right)\sin(\alpha - i_w) + \dfrac{D_{\text{wing}}}{2}\cos(\alpha - i_w), \\
T_y = 0, \\
T_z = -\left(-\dfrac{L_{\text{wing}}}{2} + \dfrac{nW_{\text{wing}}}{2} + \dfrac{nW_{\text{eng}}}{2}\right)\cos(\alpha - i_w) + \dfrac{D_{\text{wing}}}{2}\sin(\alpha - i_w), \\
M_x = \left(\dfrac{nW_{\text{wing}}}{2}y_{\text{cg}} - \dfrac{L_{\text{wing}}}{2}y_{\text{ac}} + \dfrac{nW_{\text{eng}}}{2}y_{\text{eng}}\right)\cos(\alpha - i_w) - \dfrac{D_{\text{wing}}}{2}y_{\text{ac}}\sin(\alpha - i_w) \\
M_y = \dfrac{1}{2}M_{\text{wing}} + \left(\dfrac{nW_{\text{wing}}}{2}x_{\text{cg}} - \dfrac{L_{\text{wing}}}{2}x_{\text{ac}} + \dfrac{nW_{\text{eng}}}{2}x_{\text{eng}}\right)\cos(\alpha - i_w), \\
\qquad - \dfrac{D_{\text{wing}}}{2}x_{\text{ac}}\sin(\alpha - i_w) \\
M_z = -\left(\dfrac{nW_{\text{wing}}}{2}y_{\text{cg}} - \dfrac{L_{\text{wing}}}{2}y_{\text{ac}} + \dfrac{nW_{\text{eng}}}{2}y_{\text{eng}}\right)\sin(\alpha - i_w) + \dfrac{D_{\text{wing}}}{2}y_{\text{ac}}\cos(\alpha - i_w).
\end{cases}
\tag{5.4.9}
$$

Rear fuselage

In this part, structural loads are assessed on the rear fuselage segment between the wing trailing edge (section AA') and the tail. The analysis includes empennage weight, fuselage self-weight, and aft-bay payload. Payload

masses were summed by component, converted into linear loads for each section, and the equivalent resultant forces placed at each section's midpoint. Figures 5.4.4, 5.4.5a and 5.4.5b respectively show the AA cross-section with concentrated loads, the idealized load model up to the tail, and the fuselage cross-sectional area.

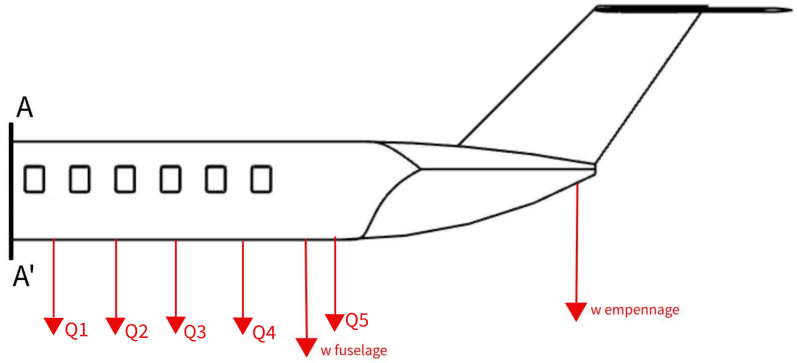

Figure 5.4.4: Representation of the rear fuselage including the studied section AA' and the weights.

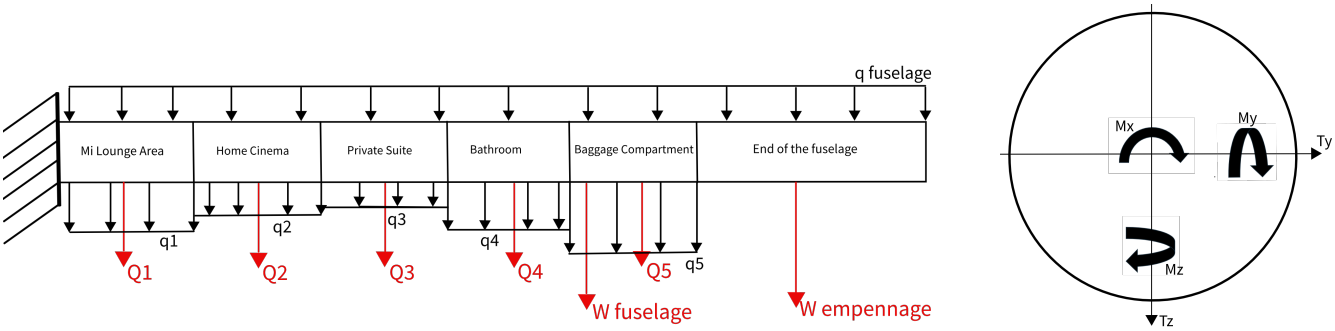

(a) **(b)**

Figure 5.4.5: Idealization of the rear fuselage with the weights distribution (a) and representation of cross section axis (b).

The equilibrium equations follow, and Table 5.4.5 summarizes the results :

$$\begin{cases} T_y = -F_{\text{fin}}, \\ T_z = -\left(SF_A - L_{\text{tail}}\right)\cos(\alpha - i_w), \\ M_y = BM_A - L_{\text{tail}} x_{\text{ac,tail}}\cos(\alpha - i_w), \\ M_z = -F_{\text{fin}} d, \\ M_x = -M_{\text{fus}}, \end{cases} \tag{5.4.10}$$

where d is the distance between the aerodynamic center of the tail and the cross-section, SF_A and BM_A are the shear force and bending moment due to self-weight and are calculated by equilibrium from the idealized representation

of the section under study, Fig 5.4.5a. The shear forces T_y and T_z are applied at the center of the fuselage section.

Point	T_y (10^3 lbf)	T_z (10^3 lbf)	M_x (10^3 lbf ft)	M_y (10^3 lbf ft)	M_z (10^3 lbf ft)
A	–23.12	–69.59	-304.54	3 572.88	–1 427.61
B	–56.58	–61.17	-746.89	2 960.97	–3 493.68
C	–56.58	–0.92	-746.89	62.87	–3 493.68
D	–47.92	–8.70	-632.10	1 078.25	–2 958.55
E	–8.49	–40.96	-111.74	3 274.47	–524.25

Table 5.4.5: Reaction forces and moments at the rear fuselage.

5.4.5 Structural design

The structural design is based on detailed analyses conducted at the wing root and the rear fuselage. Both regions are modeled using idealized structural layouts: the wing is composed of spars, ribs, stringers, and a load-bearing skin, while the rear fuselage integrates frames and stringers beneath the skin. In both cases, the stringers are modeled as booms carrying axial loads, whereas the skin is assumed to carry only shear stresses. The sizing of these components is carried out using the internal loadings obtained in Sec. 5.4.4, which defines the critical forces and moments acting on each structure. The structural design methodology applied in this section follows the Megson [23].

Wing

In order to apply the boom idealization method, the control surfaces are neglected in the current analysis. The wing root structure is assumed to consist of 43 stringers evenly spaced by approximately 5.91 in, and two main spars. These two spars divide the wing cross-section into three distinct cells. The first cell extends from the leading edge to the first spar, which is located near the aerodynamic center (approximately at a quarter of the chord). The second cell lies between the two spars, with the rear spar positioned just before the aileron region. Finally, the third cell, extending from the rear spar to the trailing edge, is assumed to carry no shear flow and is therefore not included in the torsional analysis. The idealized wing root section studied for the analysis is illustrated in Fig. 5.4.6.

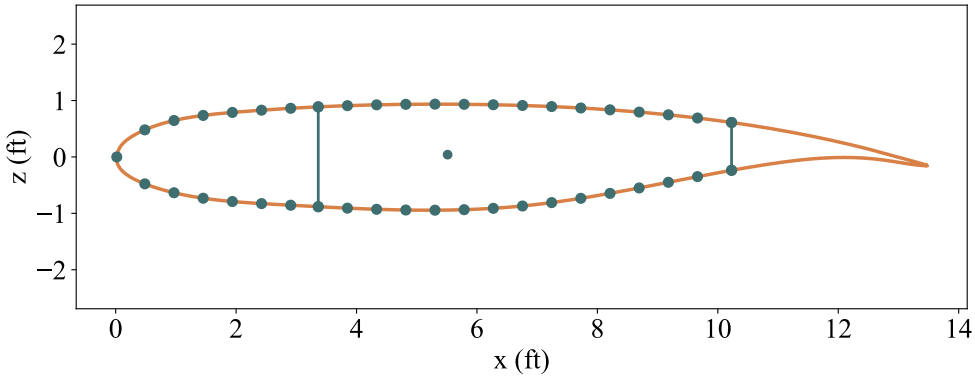

Figure 5.4.6: Representation of the idealized wing root section of the wing. The dots positioned along the perimeter correspond to the locations of the stringers (booms). The dot in the second cell indicates the location of the cross-section's centroid.

For this analytical sizing, a safety factor s = 1.5 is applied to determine the admissible limit stresses. These allowable limits are derived from the tensile and shear strengths of the CFRP material used (see Tab. 4.7.2). They represent the maximum stresses that can be applied without risking material failure :

$$\sigma_{\max} = \frac{\sigma_y^0}{s} = 69.33 \text{ ksi}, \quad \tau_{\max} = \frac{\tau_y^0}{s} = 12.07 \text{ ksi} . \tag{5.4.11}$$

The first step in the structural sizing consists in determining the minimum cross-sectional area $B_{\min}$ required for the stringers. This is achieved by computing the direct stress $\sigma_{yy,i}$ experienced by each stringer i, which is expressed as:

$$\sigma_{yy,i} = \frac{(I_{zz}M_x + I_{xz}M_z)z_i - (I_{xx}M_z + I_{xz}M_x)x_i}{I_{xx}I_{zz} - I_{xz}^2} . \tag{5.4.12}$$

Here, x_i and z_i are the coordinates of the i-th stringer relative to the centroid of the cross-section. The coordinates of the centroid at the wing root are obtained using the following expressions:

$$x_{\text{centroid}} = \frac{\sum_{j=1}^{N} B_j x_j}{\sum_{j=1}^{N} B_j} = \frac{\sum_{j=1}^{N} x_j}{N}, \qquad z_{\text{centroid}} = \frac{\sum_{j=1}^{N} B_j z_j}{\sum_{j=1}^{N} B_j} = \frac{\sum_{j=1}^{N} z_j}{N} , \tag{5.4.13}$$

where N is the number of stringers. Since all stringers are assumed to have the same area B, the centroid corresponds to the geometric center of the stringer distribution. In the Eq.5.4.12 the second moment of area I depend on the

cross-section area of the stringers B :

$$I_{xx} = \sum_{i=1}^{N} B_i z_i^2, \quad I_{zz} = \sum_{i=1}^{N} B_i x_i^2, \quad I_{xz} = \sum_{i=1}^{N} B_i z_i x_i. \tag{5.4.14}$$

The minimum area $B_{\min}$ is set to ensure that $|\sigma_{xx}| \leq \sigma_{\max}$ across all critical points. The most severe case occurs at point B, leading to $B_{\min} = 0.225$ in^2.

The skin thickness $t_{\min}$ is sized to withstand shear flows resulting from torsional and shear loads (M_y, T_x, and T_z) and is designed to resist to all critical point. The torsional shear flow is first evaluated by solving the governing system of equations related to the applied torque :

$$\begin{cases} M_y = 2A_1 q_{\mathrm{M},1} + 2A_2 q_{\mathrm{M},2} \ , \\ \frac{d\theta}{dy} = \frac{1}{2A_1 G} \oint_{\text{cell } 1} q_{\mathrm{M},1} \frac{ds}{t} \ , \\ \frac{d\theta}{dy} = \frac{1}{2A_2 G} \oint_{\text{cell } 2} q_{\mathrm{M},2} \frac{ds}{t} \ , \end{cases} \tag{5.4.15}$$

where A_i is the cell's area, G is the shear modulus, it can be computed from the tensile modulus and the poisson's ratio, $\frac{d\theta}{dy}$ is the rate of twist and $q_{\mathrm{M},i}$ shear flow in cell i due to torsion only. As the thickness is assumed to be constant, the system can be simplified as :

$$\begin{cases} M_y = 2A_1 q_{\mathrm{M},1} + 2A_2 q_{\mathrm{M},2} \ , \\ 0 = (\frac{\Pi_1}{A_1} + \frac{l_{\text{spar},1}}{A_2}) q_{\mathrm{M},1} - (\frac{\Pi_2}{A_2} + \frac{l_{\text{spar},1}}{A_1}) q_{\mathrm{M},2} \ , \end{cases} \tag{5.4.16}$$

where Π_i is the perimeter of the cell and $l_{\text{spar},1}$ is the length of the first spar in the $x - z$ plan.
The next step is to include the effect of the wing taper. This is done by defining the resultant shear forces in the webs and skin as $T_{x,\text{web}}$ and $T_{z,\text{web}}$, respectively :

$$T_{x,\text{web}} = T_x - \sum_{i}^{N} \sigma_{yy,i} Bi \frac{\delta x_i}{\delta y} \ , \quad T_{z,\text{web}} = T_z - \sum_{i}^{N} \sigma_{yy,i} Bi \frac{\delta z_i}{\delta y} \ , \tag{5.4.17}$$

where δx_i represents the change in the x-coordinate of stringer i between the wing root and tip. The same applies to δz_i and δy_i, corresponding to variations along the z- and y-axes, respectively.

Next, the shear flow induced by the applied shear forces is evaluated. Since the structure is statically indeterminate under such loading, one skin panel per cell is conceptually removed to create an open section. This allows the

computation of the base shear flow q_b within each cell :

$$\begin{aligned} q_{\mathrm{b}} &= -\frac{T_{x,\mathrm{web}} I_{xx} - T_{z,\mathrm{web}} I_{xz}}{I_{xx} I_{zz} - I_{xz}^2} \left(\int_0^s t_{\mathrm{D}} x \, ds + \sum_{i=1}^{N} B_i x_i \right), \\ &= -\frac{T_{z,\mathrm{web}} I_{zz} - T_{x,\mathrm{web}} I_{xz}}{I_{xx} I_{zz} - I_{xz}^2} \left(\int_0^s t_{\mathrm{D}} z \, ds + \sum_{i=1}^{N} B_i z_i \right) . \end{aligned} \tag{5.4.18}$$

Since the skin is assumed to carry only shear stresses, t_{D} is set to zero. The remaining unknowns are the shear flows at each cut ($q_{s,0,1}$ and $q_{s,0,2}$) and the rate of twist. These quantities are determined by matching the twist rate expressions derived independently for each cell :

$$A_1 \left(q_{s,0,2} \Pi_2 - q_{s,0,1} l_{\mathrm{spar},1} + \oint_{\mathrm{cell}_2} q_{\mathrm{b}} \frac{ds}{t} \right) - A_2 \left(q_{s,0,1} \Pi_1 - q_{s,0,2} l_{\mathrm{spar},1} + \oint_{\mathrm{cell}_1} q_{\mathrm{b}} \frac{ds}{t} \right) = 0 . \tag{5.4.19}$$

The last equation can be solved by introducing an additional equation derived from the equilibrium moment applied to the entire cross-section :

$$\begin{aligned} &\oint_{\mathrm{cell}_1} q_{\mathrm{b}} p_0 \, ds + \oint_{\mathrm{cell}_2} q_{\mathrm{b}} p_0 \, ds + 2 q_{s,0,1} A_1 + 2 q_{s,0,2} A_2 \\ &+ \sum_{i=1}^{N} \sigma_{yy,i} B_i \frac{\delta x_i}{\delta y} z_i - \sum_{i=1}^{N} \sigma_{yy,i} B_i \frac{\delta z_i}{\delta y} x_i = 0 , \end{aligned} \tag{5.4.20}$$

where p_0 represents the moment arm associated with the open-section shear flow. Once all shear flow components are determined, the total shear flow in each panel of the two cells is computed by summing the contributions from the open-section shear flow q_{b}, the redundant shear flow $q_{s,0}$, and the torsional shear flow q_{M} :

$$q_{\mathrm{total}} = q_{\mathrm{b}} + q_{s,0} + q_{\mathrm{M}} . \tag{5.4.21}$$

The minimum skin thickness is set by the panel experiencing the highest shear flow, which defines the critical case. The condition $q_{\mathrm{total}} \, / \, t \leq \tau_{\max}$ must be satisfied across all panels, for each critical point. This results in a minimum skin thickness of 0.1 in. The Tab. 5.4.6 summarizes the key structural design parameters of the wing and the Fig. 5.4.7 represent the geometry of one stringer for the wing. The parameters t_i correspond to the minimum thicknesses of the structural components i, while l_i denotes the distance between two adjacent components of type i. All dimensions comply with the minimum CFRP used thickness required to guarantee quasi-isotropic behavior.

Parameters	Value
B_{min} (in^2)	0.225
$t_{\text{skin, min}}$ (in)	0.1
$t_{\text{spars, min}}$ (in)	0.1
$t_{\text{ribs, min}}$ (in)	0.1
$l_{\text{root, stringers}}$ (in)	5.9
$l_{\text{tip, stringers}}$ (in)	1.75
l_{ribs} (in)	39.37

Table 5.4.6: Structural design parameters of the wing.

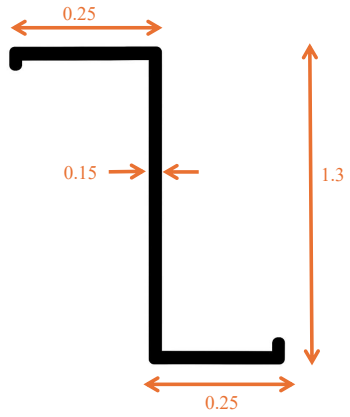

Figure 5.4.7: Stringer geometry for the wing (in).

Fuselage

The structural design of the fuselage follows the same approach as that used for the wing. The geometry is idealized as a circular cylinder, allowing the assumption of axial symmetry. There are 66 stringers uniformly distributed around each frame, and all are assumed to have the same cross-sectional area B. The cross-sectional layout used in this analysis is illustrated in Fig. 5.4.8.

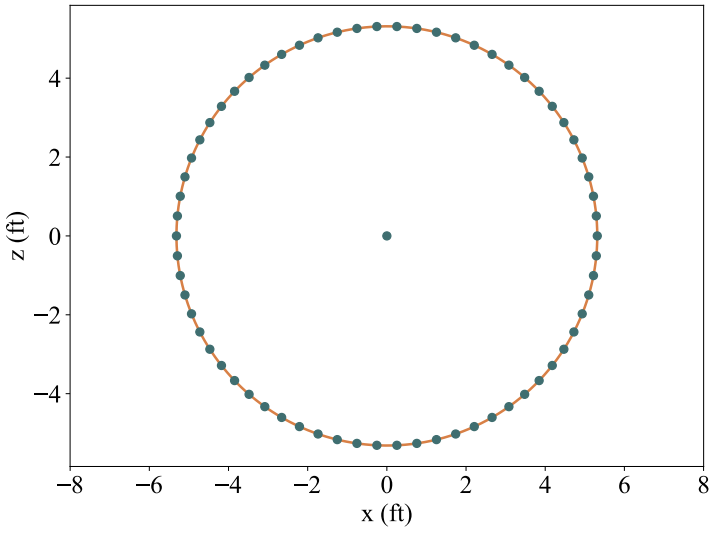

Figure 5.4.8: Representation of the idealized circular section of the rear fuselage, located directly aft of the wing. The dots positioned along the circumference correspond to the locations of the stringers (booms). The central dot indicates the location of the cross-section's centroid.

The fuselage structure is assumed to be made of the same CFRP as used for the wing components. As a result, the maximum allowable direct stress σ_{max} and shear stress τ_{max} are known from the material properties and can be

directly used for structural sizing.

As for the wing, the minimal cross-sectional area $B_{\min}$ must be determined based on the maximum direct stress experienced during critical loading conditions. Due to the circular and symmetric geometry of the fuselage, the centroid lies at the geometric center, and the cross-product of inertia vanishes: $I_{xz} = 0$. The axial stress in each stringer i therefore simplifies to:

$$\sigma_{xx,i} = \frac{M_y}{I_{yy}} z_i - \frac{M_z}{I_{zz}} y_i \ . \tag{5.4.22}$$

The minimum cross-sectional area $B_{\min}$ is determined by ensuring that the direct stresses in the stringers do not exceed the maximum allowable material stress. This condition, $|\sigma_{xx}| \leq \sigma_{\max}$ must be satisfied at all critical load cases along the flight envelope. Based on this criterion, the most demanding case was identified at point B, for which the maximum axial stress was observed. This yields a required minimum area of 0.04 in^2.

The computation of the skin thickness is simplified due to the circular and symmetric geometry of the fuselage. The required skin thickness in the rear fuselage is governed by the shear flow resulting from the combined effect of lateral and vertical shear forces, T_y and T_z, as well as the torsional moment M_x. The shear flow q in each panel i can be calculated using the following expression:

$$q^{i+1} - q^i = -\frac{T_y}{I_{zz} B_i} B_i y_i - \frac{T_z}{I_{yy}} B_i z_i + \frac{M_x}{2\pi \frac{D^2}{4}} \ , \tag{5.4.23}$$

where D is the diameter of the fuselage. The minimum required skin thickness is determined by identifying the panel subjected to the highest shear flow. This panel defines the critical loading scenario for the fuselage skin. The corresponding thickness is computed using $t = \frac{q}{\tau_{\max}}$. This maximum shear flow is observed at critical point B, which also corresponds to the most demanding case for the sizing of the stringer cross-sectional area. This results in a minimum thickness of 0.086 in. The Tab. 5.4.7 summarizes the key structural design parameters of the rear fuselage and the Fig. 5.4.9 represent the geometry of one stringer for the fuselage. The parameters $l_{\text{stringers}}$ is the distance between 2 stringers and l_{frames} between 2 frames. All dimensions comply with the minimum CFRP used thickness required to guarantee quasi-isotropic behavior.

Parameters	Value
B_{min} (in^2)	0.04
t_{min} (in)	0.086
$l_{stringers}$ (in)	6.3
l_{frames} (in)	39.37

Table 5.4.7: Structural design parameters of the fuselage

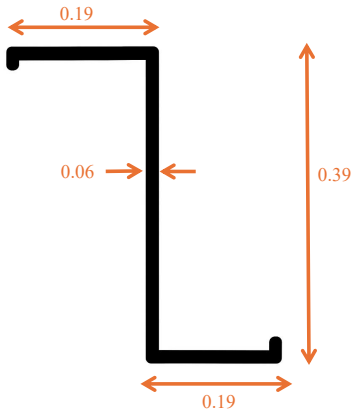

Figure 5.4.9: Stringer geometry for the fuselage (in)

5.4.6 Finite element analysis

In this section, a finite element analysis is carried out to validate and compare the results previously obtained through the analytical structural study for the wing and the rear fuselage.

Wing

Due to the geometric symmetry of the wing, only the half-wing is modeled in the finite element analysis. Consequently, applied loads are halved, and a fixed boundary condition is imposed at the wing root section. Structural components such as stringers and ribs are represented by 1D elements with assigned virtual cross-sectional areas, while the wing skin and spar webs are modeled using 2D shell elements with virtual thicknesses. A representation of the wing is shown in the Fig. 5.4.10

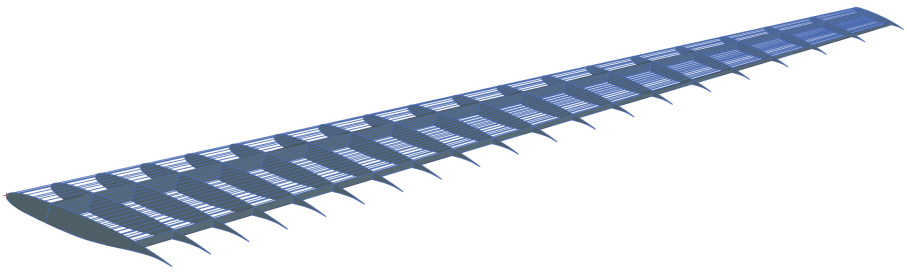

Figure 5.4.10: Representation of the wing.

The wing root is assumed fully constrained. Regarding applied loads, the analysis includes the weight of the wing in addition to aerodynamic loads (obtained by data from *DARTFlo*). All weight-related loads are scaled by the load factor corresponding to the most critical flight condition (n = 2.5). Based on the analytical study, flight

case B has been identified as the most critical loading condition for the wing, and it is therefore selected for the FEM computation performed in NX.

Following the analytical sizing outlined in Sec. 5.4.5, a finite–element analysis (FEA) of the half-wing was carried out in *Siemens NX 22*. The wing root was *fully clamped*, i.e. all six degrees of freedom were fixed. Aerodynamic lift and drag, obtained from the DARTFLo load build-up, were discretised as nodal forces and moments at every spar location along the span. Gravitational forces were applied to all structural masses and multiplied by a load factor of $n = 2.5$ to represent the most severe flight condition (case B).

With regard to the propulsion system, two modelling strategies were considered: *(i)* an explicit solid model of the engine–pylon assembly and *(ii)* a lumped point-load representation. The second approach was retained in order to reduce computational cost. Accordingly, the engine weight, scaled by the same factor $n = 2.5$, was introduced as a concentrated load at the engine centre of gravity on the lower surface of the wing.

Observations. The maximum vertical deflection occurs at the wing tip, as expected for a cantilevered beam subjected to distributed lift. The peak shear stress does *not* appear at the root but slightly outboard of the engine station. This behaviour is attributed to the large mass of the ultra-high-bypass-ratio (UHBR) engines, whose downward force partially counteracts the aerodynamic lift, thereby relieving the bending moment transmitted to the wing root. Consequently, positioning the engines beneath the wing is seen to be structurally advantageous.

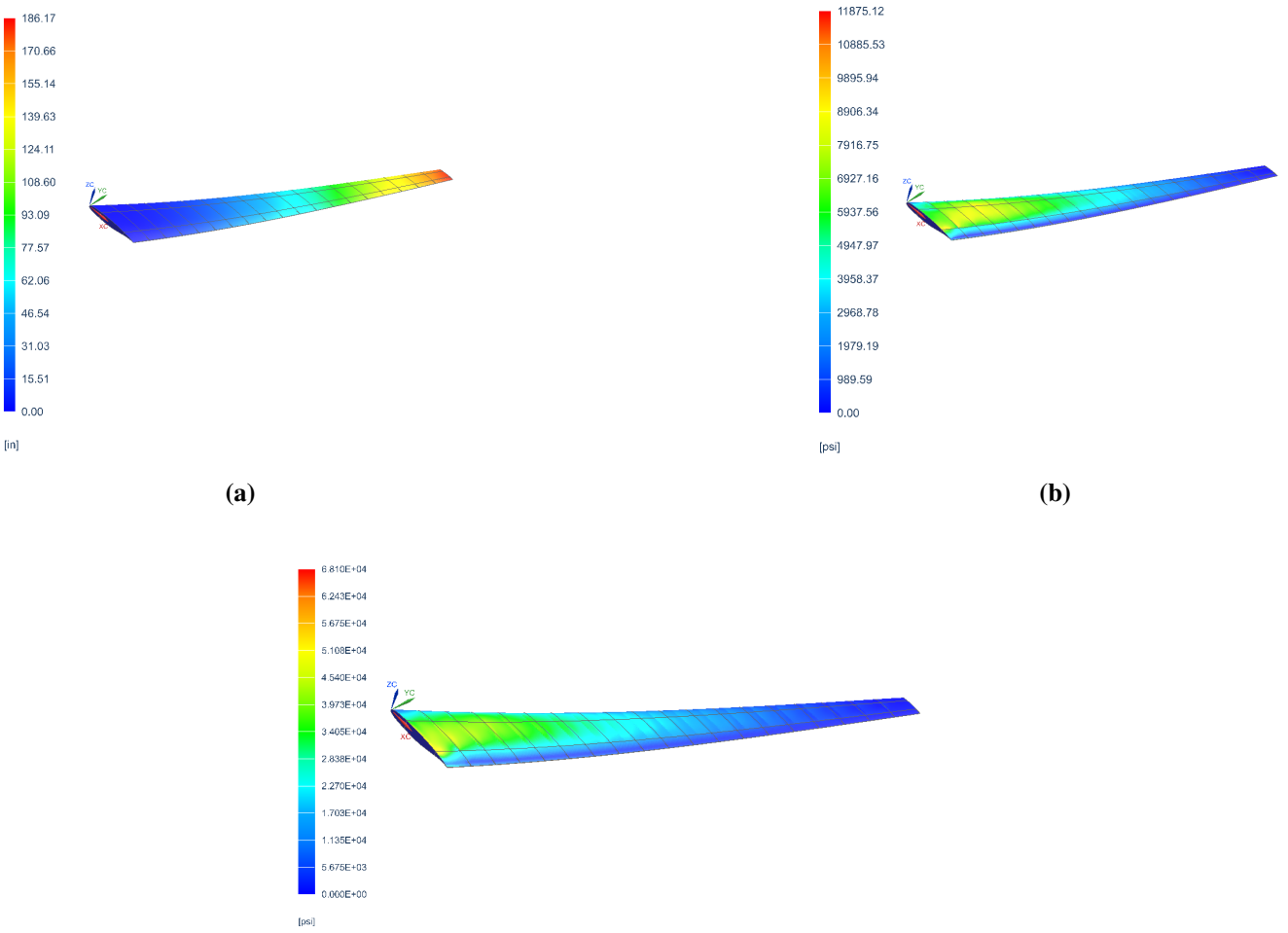

Figure 5.4.11: Results from the *Siemens NX* simulation of the wing. (a) Displacement distribution (in); (b) shear-stress distribution (psi); (c) σ_{yy} stress distribution (psi).

Parameters	Analytical	Finite element
Maximum deflection (in)	-	186.17
max($\lvert\sigma_{yy}\rvert$) (ksi)	66.12	64.130
max($\lvert\tau_{xy}\rvert$) (ksi)	12.07	11.875

Table 5.4.8: Results from the analytical study and the finite element analysis of the wing.

Rear fuselage

To validate the results obtained from the analytical structural sizing, a finite element analysis (FEA) is performed using Siemens NX. The model includes both 1D and 2D elements, where virtual thicknesses are applied to reduce computational time while preserving accuracy. A representation of the fuselage is shown in the Fig. 5.4.12.

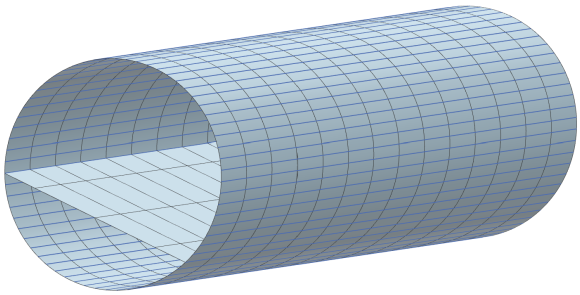

Figure 5.4.12: Representation of the rear fuselage.

The analysis focuses on critical flight condition B, previously identified as the most demanding scenario in the structural envelope. Multiple loads are considered: the fuselage's own weight, the mass of the payload (passengers and luggage) and tail assembly, the aerodynamic lift generated by the horizontal tail, and the fin load. All weight-related loads are scaled by the load factor of 2.5 corresponding to this critical case. The fuselage is clamped at the trailing edge of the wing to simulate fixed boundary conditions.

The horizontal tail lift is applied at its aerodynamic center, for each payload item are considered point materials, its mass is applied at the corresponding center of gravity on the floor of the cabin to accurately capture the discrete load contributions. The fin load is applied at its p attachment point, and the combined mass of the fin and horizontal tail is concentrated at their common center of gravity. Gravity loads on all masses are also multiplied by the 2.5 load factor to reflect the worst-case loading.

Since the horizontal tail and fin were not explicitly designed in this study, their lift, masses, and fin load are connected to the aft section of the fuselage using rigid links, ensuring the loads transmit correctly into the structure. Results show the deflection of the rear fuselage, as well as distributions of direct and shear stresses, the results are shown in the Fig. 5.4.13.

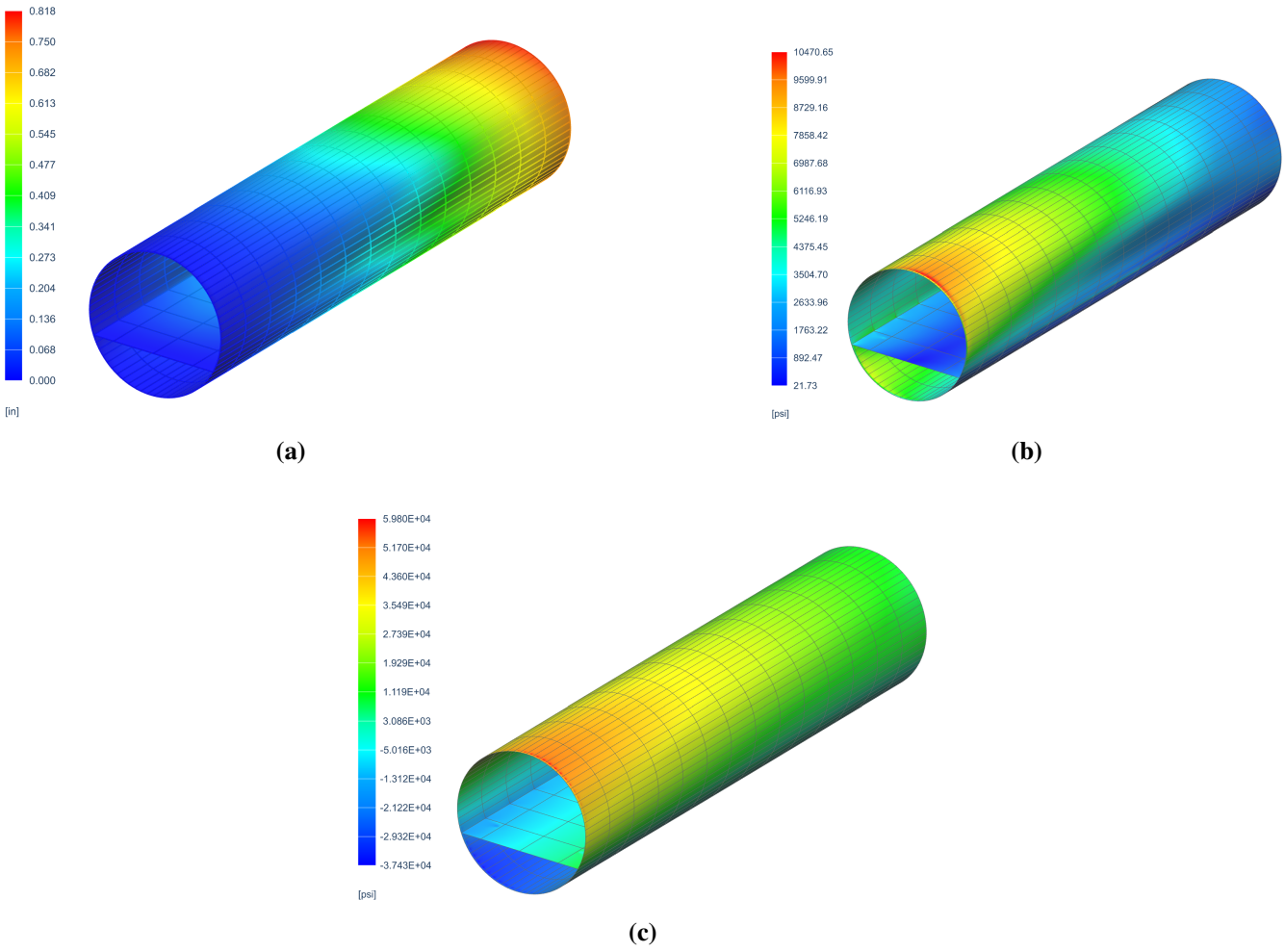

Figure 5.4.13: Results from simulation of *NX Siemens*, 5.4.13a represent the deplacement distribution (in), 5.4.13b represent the shear distribution (psi) of the fuselage and 5.4.13c represent the stress distribution (psi).

The stress distribution highlights that maximum stresses occur near the clamped section. The upper skin of the fuselage is in tension, while the lower skin is under compression. This is consistent with the physical behavior induced by the downward lift of the horizontal tail, which generates a moment compressing the lower side. The Tab. 5.4.9 compares the results obtained from the finite element analysis with those derived from the analytical approach.

Parameters	Analytical	Finite element
Maximum deflection (in)	-	0.818
max($\|\sigma_{yy}\|$) (ksi)	67.88	59.8
max($\|\tau_{xy}\|$) (ksi)	12.07	10.47

Table 5.4.9: Results from the analytical study and the finite element analysis.

The analytical approach slightly overestimates direct and shear stresses, primarily due to the assumptions like the idealization where stringers carry only axial loads and the skin handles only shear. Importantly, shear stresses remain below the material's strength, confirming the structure's safety and the deflection remains within acceptable limits, representing a small fraction of the total fuselage length. The difference between the analytical and finite element values can also stem from the concentrated load of each component applied at its center of mass in the finite element model.

5.5 Performance

5.5.1 Take-off

The take-off performance has been assessed under both nominal and One Engine Inoperative (OEI) conditions, in line with FAA Part 25 certification standards. The sequence includes four segments: ground roll, rotation, transition, and obstacle clearance, as illustrated in Fig. 5.5.1.

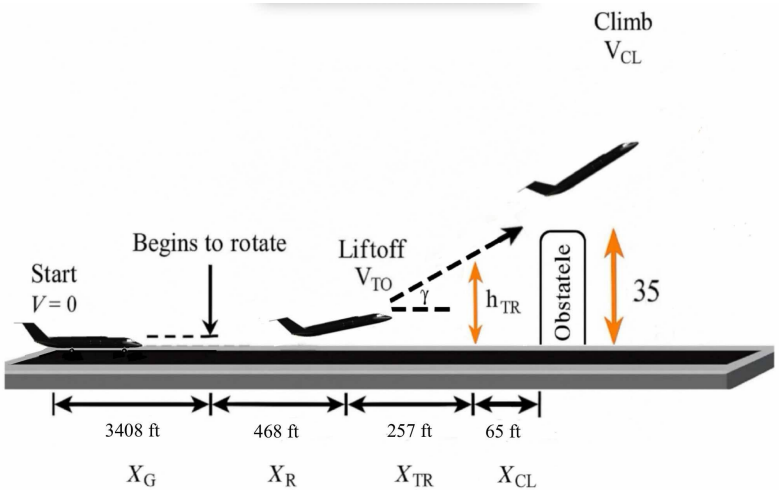

Figure 5.5.1: Distance travelled during the 4 phases of the take-off: Ground roll X_G, Rotation X_R, Transition X_{TR}, and Obstacle Clearance X_{CL}.

Double slotted flaps were deflected at 25°, providing a maximum lift coefficient of $C_{L_{max}} = 1.85$. The stall and take-off speeds were estimated as $V_{stall} = 212.73$ ft/s and $V_{TO} = 233.99$ ft/s respectively. The climb is performed at $V_{CL} = 255.28$ ft/s, with a trajectory angle of $\gamma = 10.33°$. The ground acceleration has been computed using the following expression [29]:

$$a = \frac{g}{W}\left(T - D - \mu(W - L)\right), \tag{5.5.1}$$

where T is the thrust, D the drag, L the lift, W the aircraft weight, μ the ground friction coefficient, and g the gravitational acceleration. Induced drag was corrected for ground effect and flap deflection.

The total take-off distance at sea level was found to be 4193.7 ft. All intermediate distances are shown in Fig.5.5.1.

A decision speed of $V_1 = 222.31$ ft/s has been calculated to ensure that, in case of an engine failure, the aircraft can safely abort or continue the take-off depending on the failure timing. The certified take-off field length (TOFL) under OEI conditions is 5231.1 ft, including a dual-engine segment up to V_1, followed by a single-engine segment and obstacle clearance. The climb-out with one engine is performed at a trajectory angle of 2.13°, in compliance with the minimum 1.38° angle imposed by FAR 25.121 [11].

5.5.2 Climb

The climbing performance of the aircraft has been assessed using both the angle of climb and the rate of climb, computed from the force balance in steady flight. The climb angle θ is derived from the following relations:

$$\begin{cases} L = W\cos\theta \\ T = D + W\sin\theta \end{cases} \quad \Rightarrow \quad \theta = \arcsin\left(\frac{T - D}{W}\right). \tag{5.5.2}$$

The rate of climb (ROC), a more direct indicator of performance, is expressed as:

$$ROC = V\sin\theta = \frac{TV - DV}{W}, \tag{5.5.3}$$

Both thrust and drag were calculated based on the aircraft polar curve, corrected for altitude and Mach number. The resulting contour maps of climb angle and ROC are shown below on Fig. 5.5.2. The optimal climb speed (black dashed line) has been extracted from these maps and used to estimate the minimum time to reach the cruise altitude. This time can be derived by integrating the inverse of the ROC curve:

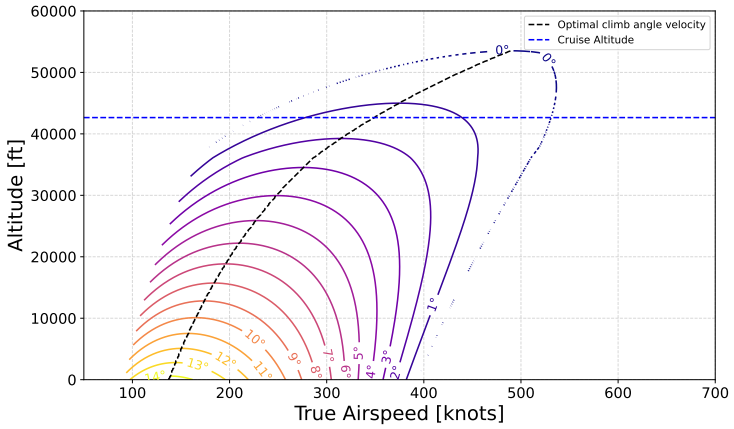

(a) Angle of Climb (°)

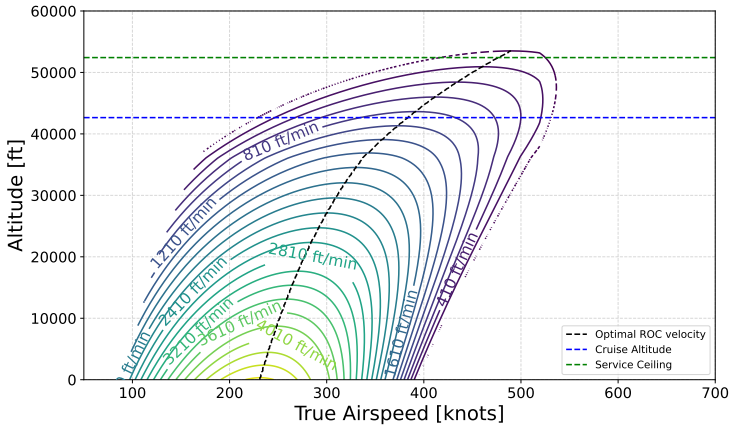

(b) Rate of Climb (ft/min)

Figure 5.5.2: Climb performance maps as a function of true airspeed and altitude.

$$\Delta t = \int_{h_1}^{h_2} \frac{1}{ROC(h)}\, dh, \tag{5.5.4}$$

Assuming that the aircraft maintains the optimal speed (max ROC), the integral is computed piecewise between discrete altitude steps. The horizontal distance covered during the climb was calculated using:

$$\Delta x = \int_{t_1}^{t_2} V_h(t)\, dt, \tag{5.5.5}$$

All key performance values extracted from the maps (maximum climb rate, service ceiling, absolute ceiling, climb gradient at cruise, etc.) are summarized in Tab. 5.5.1.

Parameter	Value	Parameter	Value
Maximum ROC	4,420 ft/min	Absolute ceiling	53410 ft
ROC at cruise altitude	760 ft/min	Service ceiling	52,418 ft

Table 5.5.1: Parameters of the rate of climb performance.

Under standard atmospheric conditions and with both engines delivering maximum thrust, the aircraft is able to reach the cruise altitude of 42,650 ft in approximately 18.9 minutes. During this climb, a horizontal distance of about 88.4 nm is covered, following the optimal ROC trajectory. This confirms the aircraft's capacity to climb rapidly and efficiently toward its cruise condition.

5.5.3 Turn

The turning performance of the aircraft has been evaluated under level, constant-speed conditions, following the methodology described by the Raymer [29]. In such maneuver, the horizontal component of the lift generates the centripetal force required to maintain the turn, while the vertical component balances the aircraft's weight. The system of equations governing the turn dynamics is given by:

$$\begin{cases} T - D = 0 \\ L\cos\kappa - W = 0 \\ L\sin\kappa - \dfrac{W}{g}\dfrac{V^2}{R_{\text{turn}}} = 0 \end{cases} \tag{5.5.6}$$

where κ is the bank angle, V is the true airspeed, and R_{turn} is the turn radius. These relations lead to the expression of the turn radius as:

$$R_{\text{turn}} = \frac{V^2}{g\sqrt{n^2 - 1}}, \tag{5.5.7}$$

with n the load factor.

The aircraft's turn performance is limited by stall at low speeds, and by available thrust at higher speeds due to increased drag induced by higher load factors. At a given altitude and speed, the aircraft can only perform a coordinated turn if enough excess thrust is available to counteract drag. The increase in turn rate is accompanied by a rise in load factor, which in turn increases drag and limits the operational envelope.

The turn performance has been evaluated at cruise altitude (42650 ft), and the resulting performance maps are shown in Fig.5.5.3.

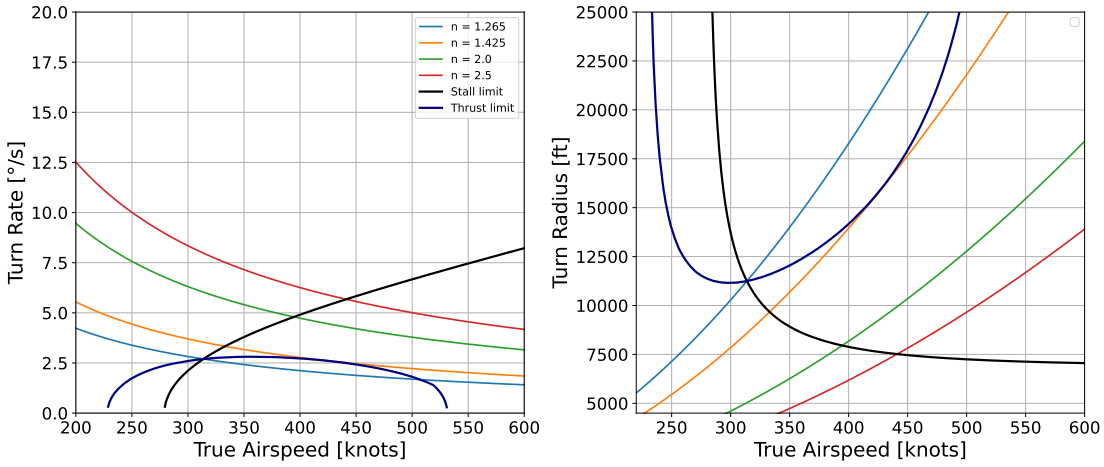

Figure 5.5.3: Turn performance (turn rate and turn radius) in cruise conditions (altitude = 42,650 ft)

At low airspeeds, stall occurs before the desired turn rate is reached. At high speeds, the available thrust becomes insufficient to sustain the turn at constant altitude. The permissible turn domain lies between these two boundaries.

Parameter	Value	Parameter	Value
Maximum turn rate $\dot{\psi}_{\max}$	2.813 deg/s	Maximum bank angle $\kappa_{\max}$	45.43°
Maximum load factor $n_{\max}$	1.425	Minimum turn radius $R_{\min}$	11,155 ft

Table 5.5.2: Relevant turning performance parameters in cruise conditions (altitude=42650 ft).

5.5.4 Glide performance

In the event of a total loss of thrust, the ability of the aircraft to safely glide toward the nearest suitable landing area becomes a critical safety metric.

The evaluation was performed for an altitude of 42,650 ft, with the aircraft weight adjusted to reflect a mid-mission condition (i.e., 50 % fuel burned). The best glide performance is achieved at the optimal glide speed, which minimizes the sink rate for a given horizontal distance.

The aircraft achieves a maximum lift-to-drag ratio (L/D) of 22.33 and maintains a shallow glide angle of only 2.56°, allowing a horizontal range exceeding 156.7 nmi. The descent time is about 24.8 minutes, and the associated sink rate is 1,721.8 ft/min. These values confirm the aircraft's ability to safely glide to an alternate airport under

emergency conditions.

5.5.5 Landing Performance Analysis

The landing performance of the aircraft can be divided in 4 phases: the approach, the flare, the free-roll phase, and the braking segment. This decomposition allows for accurate modeling and ensures compliance with certification requirements.

- **Approach Phase :** The approach segment starts at a 50 ft obstacle clearance height and follows a constant descent angle of 3°, in line with FAA guidelines. The approach speed is defined as $V_A = 1.3\ V_{\text{stall}}$, and the approach distance is computed using:

$$X_A = \frac{h_{\text{obstacle}} - h_F}{\tan(\gamma_A)} ,$$

  where h_F is the flare initiation height and γ_A the approach angle.

- **Flare Phase :** In the flare phase, the aircraft transitions from descent to touchdown by following a circular arc with radius:

$$R = \frac{V^2}{g\ n} ,$$

  where $n = 1.2$ is the load factor. The horizontal and vertical displacements during flare are given by:

$$X_F = R \sin(\gamma_A), \quad h_F = R(1 - \cos(\gamma_A)) .$$

- **Free Roll Phase :** After touchdown, a 2-second free roll is considered before the braking systems are fully applied. The free roll distance is computed as:

$$X_{FR} = V_{TD}\ t_{FR} ,$$

  where $V_{TD} = 1.15\ V_{\text{stall}}$ is the touchdown speed, and t_{FR} is the free roll delay (2 s).

- **Braking Phase :** Once braking begins, the aircraft decelerates until full stop. Assuming no reverse thrust (as required for certification), the deceleration is given by:

$$a = \frac{g}{W}(T - D - \mu(W - L)) .$$

On a dry, flat runway, and with braking devices deployed, the friction coefficient $\mu = 0.4$ is used. The total braking distance is then:

$$X_B = \frac{V^2}{2a} .$$

- **Certification Compliance :** According to FAA regulation 14 CFR Part 25.125(b), the aircraft must demonstrate landing within 60% of the available runway length, and reverse thrust must not be considered for certification purposes [11]. The results summarize in Tab. 5.5.3 confirm that, even without thrust reverse, the total landing distance remains below this threshold for all mission runways.

For example, the Aspen airport known for its high altitude and low temperatures presents more demanding landing conditions due to reduced friction. Nevertheless, the performance analysis confirms safe landing capability on all target runways, all of which exceed 6000 ft in length.

The Tab. 5.5.3 summarizes each landing segment in feet (no reverse thrust considered):

Phase	Distance (ft)
Approach	919.35
Flare	69.47
Free roll	423.38
Braking	2161.47
Total (raw)	3573.66
Certified (×1.67)	5953.72

Table 5.5.3: Landing distance breakdown according to FAA 14 CFR Part 25 (no reverse thrust).

5.5.6 Range Analysis

The range of an aircraft is directly influenced by how its total weight is allocated between payload and fuel, under the constraint of a fixed maximum take-off weight (MTOW). To meet the design goal of achieving 8000 nautical miles, it is essential to understand how fuel and payload allocations affect range. To evaluate this relationship, the classical Breguet equation was used:

$$R = \frac{V}{\mathrm{SFC}} \frac{L}{D} \ln\left(\frac{W_i}{W_f}\right) . \tag{5.5.8}$$

In this equation, R is the range, V is the cruise speed, SFC is the specific fuel consumption, L/D is the lift-to-drag ratio and W_i/W_f is the ratio of the initial to the final cruise weight. The expression highlights the importance of

aerodynamic efficiency and fuel weight on mission range. The payload range diagram during cruise can be seen on Fig. 5.5.4.

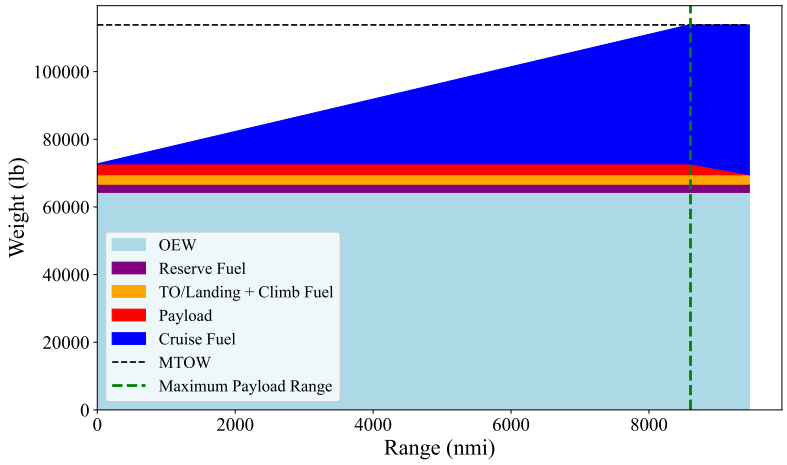

Figure 5.5.4: Payload range diagram at Mach 0.9 cruise speed.

The Fig. 5.5.4 shows the evolution of aircraft weight components with increasing cruise range. The Operating Empty Weight (OEW) includes the aircraft structure, systems, fixed equipment and crew.

The maximum payload corresponds to the *NAPA Economic Mission* (see Tab1.0.1 for more details), which models a representative flight from Napa to Mexico City. The mission includes 8 passengers with baggage and 12 cases of wine. The payload remains constant up to the maximum payload range (indicated by the vertical dashed line), beyond which it is gradually reduced to allow for additional cruise fuel.

Fixed fuel components including takeoff, climb, landing, and reserve are treated as constant. The cruise fuel component increases with range while keeping the total weight within MTOW limits. The key parameters of weight and range are summarized in Tab. 5.5.4 below.

Parameter	Value
Maximum Take-Off Weight (MTOW) (lb)	113813.64
Operating Empty Weight (OEW) (lb)	64306.95
Maximum Payload (lb)	3205.52
Maximum Payload Range (nmi)	8590.36
Maximum Range (nmi)	9455.05

Table 5.5.4: Key aircraft weights and range performance metrics.

To investigate the effect of increased cruise speed on range performance, a second payload range analysis was performed at Mach 0.92 using the same aircraft configuration and is presented in Fig. 5.5.5.

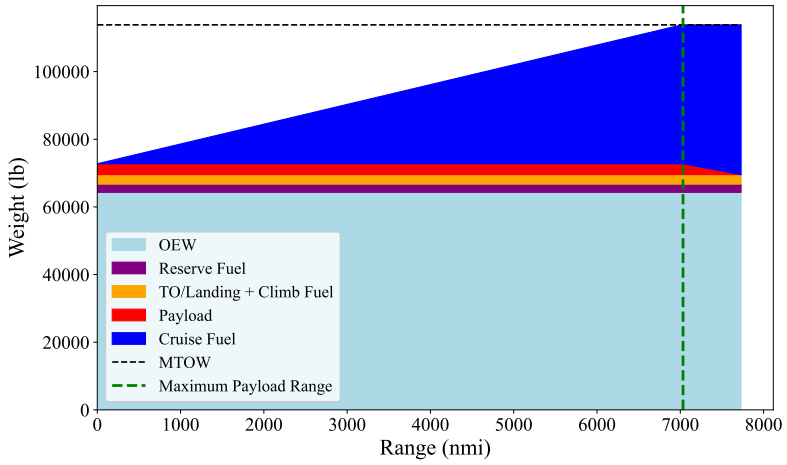

Figure 5.5.5: Payload range diagram at Mach 0.92 cruise speed.

Fig. 5.5.5 shows that, while the range requirement of 8000 nautical miles is no longer fulfilled at Mach 0.92, the aircraft still reaches a maximum range very close to it. It is important to notify that the design objective of the *Infinity Jet* was to create a highly versatile aircraft capable of performing ultra long range missions exceeding 8000 nm while maintaining fuel efficiency. This balance between range and consumption was a key driver in the choice of a target cruise Mach number. The choice has been made to target a slightly lower cruise speed of Mach 0.9. This choice was made intentionally, as flying at Mach 0.92 significantly increase fuel consumption, compromising range and other performance for long-distance missions.

However, for shorter missions such as those under 7000 nautical miles, including the Aspen Economic and Napa Economic missions it is entirely feasible to cruise at Mach 0.92. In these cases, the time savings gained from the higher cruise speed can be advantageous, especially when fuel consumption is less critical due to the shorter flight length. That said, operating at this higher speed does come with the trade-off of increased fuel burn.

5.5.7 Fuel consumption

The total mission fuel was divided into five components : takeoff fuel, climb fuel, landing fuel, reserve fuel and cruise fuel. The reserve fuel was calculated based on the Federal Aviation Regulations (FAR) [1], which require the aircraft to be capable of flying an additional 45 minutes at cruise conditions after completing the planned mission. While the fixed components are relatively small and consistent across missions, the cruise fuel varies significantly

with range.

The cruise and the reserve fuel are found using Breguet's equation 5.5.8. The remaining components are based on estimations coming from Roskam [33] :

$$W_{\text{TO}} = W_{\text{landing}} = 0.0035 W_i \ , \tag{5.5.9}$$

$$\frac{W_{\text{climb}}}{W_{\text{TO}}} \approx \frac{1}{100}\left[\frac{\text{cruise altitude}}{31600} + \frac{1}{2}M^2_{\text{cruise}}\right]. \tag{5.5.10}$$

Repartition of the fuel consumption for maximum range mission are summarized on Fig.5.5.6 and Tab. 5.5.5.

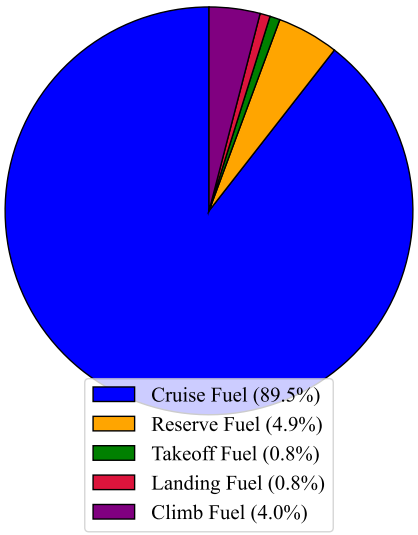

Figure 5.5.6: Fuel distribution for a maximum range mission.

Fuel Component	Weight (lb)
Takeoff Fuel Weight (W_{TO})	398.35
Landing Fuel Weight (W_{landing})	398.35
Climb Fuel Weight (W_{climb})	1997.09
Reserve Fuel Weight (W_{reserve})	2424.23
Cruise Fuel Weight (max range)	44288.68
Total Fuel Weight (max range)	49468.71

Table 5.5.5: Fuel components for a maximum range mission.

In order to assess the viability of a mission at a cruise Mach of 0.92 and a range of 7000 nautical miles, the total fuel consumption has been evaluated. The analysis revealed that such a mission would require 27.59% more fuel compared to the baseline configuration of cruise Mach at 0.9. This result validates the initial design decision to target a cruise Mach of 0.9, as it ensures optimal fuel efficiency while enabling missions exceeding 8000 nautical miles of range.

6 Cost and Life Cycle Assessment

6.1 Cost Analysis

The cost analysis of the Infinity Jet includes both acquisition and operational aspects, providing an overview of the aircraft's financial viability through its life cycle.

The flyaway cost represents the production cost per aircraft, excluding non-recurring investments. It includes airframe manufacturing, propulsion systems, avionics, and interior outfitting. Based on Raymer's methodology [29] and assuming full-rate production of 100 aircraft, it was estimated at $44,998,272 per unit. A non-recurring cost (NRC) was added to cover tooling, certification and engineering, assumed to be distributed over a production of 100 aircraft. This NRC cost is amortized by distributing them evenly across the total planned production, effectively adding a fixed share of NRC to the cost of each unit. This cost amounts to approximately 35,998,618$. Applying a 15% profit margin leads to a target selling price of 52,161,997$ per unit.

These estimations are based on an expected operational profile of 500 flight hours per year for 25 years. The direct operating cost (DOC) was calculated at 5,515.22$/hour, including fuel, crew, maintenance, and other operating expenses. The fuel cost calculation assumes the use of Jet A fuel, which is standard for business jet operations.

These values are summarized in Tab. 6.1.1.

Cost Category	Amount (USD)
Flyaway Cost	44,998,272
Non-Recurring Cost (NRC)	35,998,618
Unit Cost (incl. NRC share)	45,358,258
Target Selling Price (15% profit)	52,161,997
Total Direct Operating Cost (DOC)	5,515.22 per flight hour

Table 6.1.1: Key costs and direct operating cost per flight hour.

These values were derived based on typical cost breakdowns, found mainly in Gudmundsson's methodology [16]. The detailed breakdown of non-recurring costs and direct operating costs is indicated in Tab. 6.1.2.

NRC Breakdown	Amount (USD)	DOC Breakdown	Amount (USD)
Tooling Cost	4,499,827	Fuel Cost per hour	2,115.22
Certification Cost	13,499,482	Crew Cost per hour	1,200
Engineering Cos	17,999,309	Maintenance Cost per hour	1,500
		Insurance Cost per hour	400
		Landing & Navigation Fees /hour	300

Table 6.1.2: Detailed breakdown of Non-Recurring Costs and Direct Operating Costs.

A break-even analysis was performed to evaluate the overall profitability of the program. Assuming a total production of 100 aircraft, the cumulative profit becomes positive after the sale of 6 units, marking the break-even point. This includes the amortization of all non-recurring costs such as tooling, certification and engineering. Beyond this threshold, each additional unit sold contributes directly to the profit margin. By the end of the production, the cumulative profit reaches approximately 680,373,876.42$, confirming the economic viability of the Infinity Jet.

6.2 Life Cycle Assessment

The life cycle assessment of the Infinity Jet focuses on the environmental impact of fuel consumption throughout the aircraft's operational life. Jet-A fuel was assumed, with a standard CO_2 emission factor of 6.97 lb per fuel lb. Assuming a yearly utilization of 500 flight hours during 25 years and knowing the fuel consumption through the

SFC, the yearly and cumulative CO_2 emissions can be estimated.

These results are summarized in 6.2.1.

LCA Metric	Jet-A CO2 emission factor	Yearly CO2 emissions	Lifetime CO2 emissions
Value	6.97 lb CO_2/lb fuel	4,513,455.77 lb	112,836,392.73 lb

Table 6.2.1: CO_2 emissions over the aircraft life cycle.

These results emphasize the importance of aerodynamic efficiency and weight optimization in reducing environmental impact. While business jets operate fewer hours than commercial airliners, their emissions per passenger can be relatively high, making fuel efficiency a critical design objective.

7 Trade-off study

In this section, several parameters will be reevaluated to show the robustness and the accuracy of the previous choices. This study concerns the main decisions made in the conceptual design: the aspect ratio, the engine, and the cruise speed.

7.1 Aspect ratio impact

One of the main characteristics of this business jet is its high aspect ratio. In Fig. 5.1.6, it can be observed that the *Infinity Jet* does not fly at the optimum. It comes from the important AR and span, and the flight conditions. Since the aircraft does not fully take advantage of this uncommon geometry, applying a lower aspect ratio for the aircraft could be a better solution in order to fly with the same key advantages at the optimum.

To verify this proposition, a more common aspect ratio of 12 has been applied to the current aircraft. As a result, several parameters have changed: the wing surface (assuming a constant span), the chord, the total weight, the fuel volume in the wing and then a new design lift coefficient has been found. The lift-to-drag ratio evolution of this new aspect ratio is represented in Fig. 7.1.1. Even if the cruise L/D is much closer to the optimum, it can be observed that its value is not as high as the one for the current AR.

Therefore, since the focus was given to the fuel consumption and the long range during the whole conception, the aspect ratio with the higher L/D is kept; the current AR is the one corresponding the most to the expectations, even if the *Infinity Jet* does not fly at the optimum.

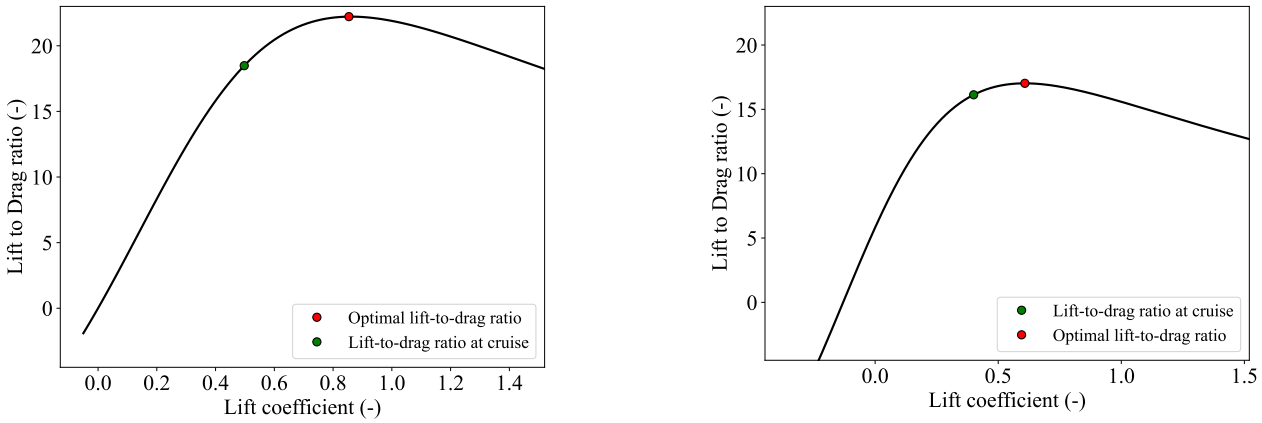

(a) AR = 15 **(b)** AR = 12

Figure 7.1.1: Evolution of the lift-to-drag ratio depending on the aspect ratio.

Similarly, a greater AR could be chosen in order to maximize the L/D, the range and minimize the fuel consumption. As before, the AR of the current aircraft has been changed ; its new value is 17.5 (+10% of the current value) with a new design lift coefficient. In Tab. 7.1.1, the evolution of some important parameters is represented as a function of the aspect ratio. An improvement is represented in green when a downgrade is represented in red. Even if the new aspect ratio gives some improvement, the increase of landing distance does not comply with the Code of Federal Regulations concerning the landing distance [11]. Therefore, the current aspect ratio of 15 is kept.

	AR=15	AR=17.5
L/D (-)	**18.21**	+ 4.39%
MTOW (lb)	**113 880**	- 4.36%
Range (nmi)	**9455.05**	+ 4.06%
Fuel consumption per distance (lb/nmi)	**4.68**	- 6.62%
Takeoff distance (ft)	**4175.7**	- 2.21%
Landing distance (ft)	**3573.66**	+ 4.13%

Table 7.1.1: Trade-off study of the aspect ratio (15, 17.5) concerning multiple parameters.

7.2 Engine selection impact

Another key design choice for the *Infinity Jet* is the use of an engine with a high bypass ratio. To assess whether the PW1900G is indeed the most optimal choice, it is valuable to consider an alternative engine with a lower bypass ratio resulting in a smaller and lighter engine. The goal is to evaluate whether the PW1900G truly represents the best trade-off between weight and specific fuel consumption (SFC), or if reducing the bypass ratio and thus the weight could lead to a more optimal configuration.

For this reason, in this section, the PW1900G has been replaced with the PW1700G, an engine from the same family, but lighter and equipped with a lower bypass ratio. It can be observed in Tab. 4.3.1 that the difference in engine weight is not negligible, with a 20% variation for only a 4% increase in SFC. When recalculating the aircraft's weight in these configurations, it has been found that the total weight decreases to 110123 lb, approximately, thanks to both the lower engine weight and the reduced fuel requirement.

However, the engine power is not sufficient. The aircraft cannot take off from the ground, as can be seen in the climb diagram represented in Fig. 7.2.1. In addition, the selected cruise altitude lies dangerously close to the aircraft's service ceiling, leaving little to no operational margin. Even with engines at full throttle, the aircraft would require more than 28.2 minutes to reach cruise altitude, making this configuration operationally unviable in most realistic mission profiles.

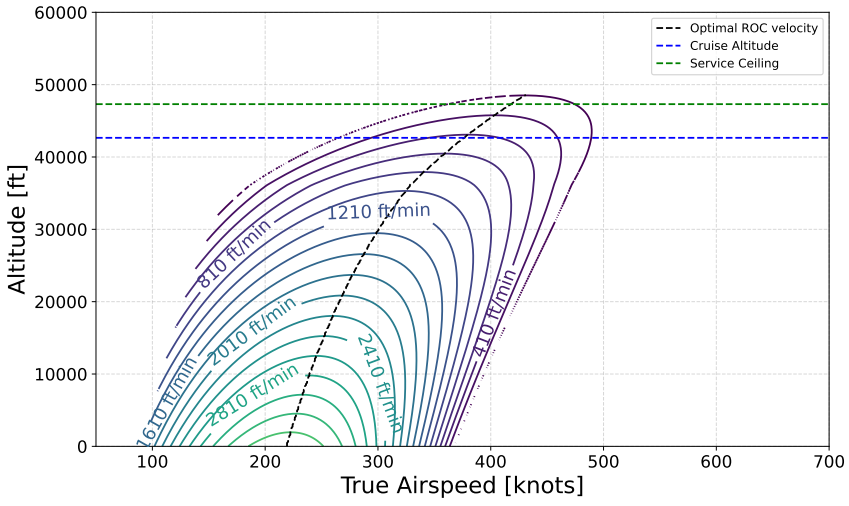

Figure 7.2.1: Climb diagram of the *Infinity jet* with the PW1700G engine.

8 Conclusion

The conceptual design phase was first conducted by the team, during which the aircraft geometry, mass distribution, and mission feasibility were iteratively refined. Key design decisions were derived from the initial requirements, and successive geometric refinements were applied until both stability and target performance metrics were achieved.

Subsequently, the preliminary design phase was undertaken, where each component was validated and enhanced using advanced methods and in-depth performance analyses. The structure was evaluated, and the aircraft's aerodynamics were reassessed with greater precision. Flight performance across various conditions was analyzed, and both dynamic and static stability were confirmed.

A clean-sheet concept was proposed to meet the AIAA's next-generation ultra-premium business jet challenge. It was defined by a high-wing configuration, high-bypass turbofans, and critically, a high-aspect-ratio wing (AR = 15). A cruise lift-to-drag ratio of 18.2 was achieved at Mach 0.9, and a maximum range of 9,455 nmi was realized; 1,455 nmi beyond the AIAA requirement, while field lengths of 4,194 ft for take-off and 3,573 ft for landing were maintained.

All required mission profiles were successfully validated, from transcontinental to shorter regional routes, ensuring unmatched operational flexibility. At a MTOW of 113,881 lb, it comfortably accommodates eight passengers and three crew members, featuring a full lounge, a separate meeting room, a cinema, a bedroom, and a luxurious bathroom. An estimated unit cost of USD 52,162,000 was established, preserving the jet's competitiveness within its segment.

In conclusion, a high-performance business jet that combines outstanding aerodynamic efficiency, structural integrity, and mission capability has been developed to satisfy the AIAA design challenge requirements. With the conceptual and preliminary design phases completed, the project is poised to proceed to detailed CFD and FEM simulations and potential prototyping.

References

[1] Federal Aviation Administration. *Title 14 – Code of Federal Regulations, Part 25: Airworthiness Standards – Transport Category Airplanes*. Tech. rep. U.S. Department of Transportation.

[2] AirfoilTools. *SC20714 Airfoil*. Accessed: 2025-04-25. 2025. URL: http://airfoiltools.com/airfoil/details?airfoil=sc20714-il.

[3] AirNav, LLC. *KASE - Aspen-Pitkin County Airport/Sardy Field*. https://www.airnav.com/airport/KASE. Accessed April 24, 2025. 2025.

[4] AirNav, LLC. *KVNY - Van Nuys Airport*. https://www.airnav.com/airport/KVNY. Accessed April 20, 2025. 2025.

[5] American Institute of Aeronautics and Astronautics. *Request for Proposal: Modern Regional Jet Family*. https://aiaa.org/get-involved/university-students/design-competitions/. Accessed April 20, 2025. 2025.

[6] Thomas Andrianne and Ludovic Noels. *Aeronautics Design Project (anglais)*. Cours, Université de Liège. 2025. URL: http://www.ltas-cm3.ulg.ac.be/classes.htm.

[7] Aspen Public Radio. *Moving the Runway at Aspen's Airport Could Conclude a Decades-long Debate over Expansion*. Accessed April 20, 2025. 2024. URL: https://www.aspenpublicradio.org/government/2024-04-15/moving-the-runway-at-aspens-airport-could-conclude-a-decades-long-debate-over-expansion.

[8] Aspen Times. *Aspen Airport to Begin Accepting Proposals for Runway, Terminal Designs*. Accessed April 20, 2025. 2025. URL: https://www.aspentimes.com/news/aspen-airport-to-begin-accepting-proposals-for-runway-terminal-designs/.

[9] Adrien Crovato. 'Steady Transonic Aerodynamic and Aeroelastic Modeling for Preliminary Aircraft Design'. PhD thesis. University of Liège, 2020.

[10] Bernard Etkin and Lloyd Duff Reid. *Dynamics of Flight: Stability and Control*. 3rd. John Wiley & Sons, 1996. ISBN: 978-0471034186.

[11] Federal Aviation Administration. *14 CFR § 121.195 - Landing limitations: Destination airport*. https://www.law.cornell.edu/cfr/text/14/121.195. Code of Federal Regulations, Title 14 – Aeronautics and Space. 2024.

[12] *Flying Qualities of Piloted Aircraft*. Tech. rep. MIL-STD-1797A. Military Standard. Washington, D.C.: U.S. Department of Defense, 1990.

[13] *Flying Qualities of Piloted Airplanes*. Tech. rep. MIL-F-8785C. Military Specification. Washington, D.C.: U.S. Department of Defense, 1980.

[14] GE Aerospace. *Passport Engine Datasheet*. Tech. rep. Product datasheet. GE Aerospace, 2023. URL: https://www.geaerospace.com/sites/default/files/2022-01/GEPassport-DataSheet.pdf.

[15] GE Aerospace. *Passport/CF34-10 Engine Options for B-52 Re-engining*. Tech. rep. Product datasheet. GE Aerospace, 2020. URL: https://www.geaerospace.com/sites/default/files/GE-and-B-52-re-engining-datasheet.pdf.

[16] Snorri Gudmundsson. *General Aviation Aircraft Design Applied Methods and Procedures*. 2014.

[17] Snorri Gudmundsson. *General Aviation Aircraft Design: Applied Methods and Procedures*. 2nd. Butterworth–Heinemann, 2014.

[18] Charles D. Harris. *NASA Supercritical Airfoils: A Matrix of Family-Related Airfoils*. Tech. rep. NASA TP-2969. NASA Langley Research Center, 1990.

[19] *HexPly® 8552 Product Data Sheet*. Tech. rep. Mid-toughened, high strength, damage-resistant, structural epoxy matrix. Hexcel Corporation.

[20] Renaldo V. Jenkins, Acquilla S. Hill and Edward J. Ray. *Aerodynamic Performance and Pressure Distributions for a NASA SC(2)-0714 Airfoil Tested in the Langley 0.3-Meter Transonic Cryogenic Tunnel*. Tech. rep. NASA TM-4044. NASA Langley Research Center, 1988.

[21] Johansson.S and Claesson.I. *Active Noise Control in Propeller Aircraft*. Tech. rep. Ronneby, Sweden: Department of Telecommunications and Signal Processing, Blekinge Institute of Technology, 2003.

[22] W.H. Mason. *Configuration Aerodynamics*. Chapitre 7: Transonic Aerodynamics of Airfoils and Wings. 2006.

[23] T.H.G. Megson. *Aircraft Structures for Engineering Students*. 7th. Butterworth-Heinemann, Elsevier, 2022. ISBN: 978-0-75066-7395.

[24] NASA Glenn Research Center. *Altitude Effects on Jet Engine Performance*. Available at https://www.grc.nasa.gov/www/k-12/airplane/thrsteq.html. 2002.

[25] NASA Langley Research Center. *Transonic Drag and Thrust Losses in High Bypass Engines*. NASA Technical Paper 1538. 1998.

[26] Ludovic Noels. *Aircraft Design: Conceptual Design*. Lecture notes, Faculté des Sciences Appliquées, Université de Liège. 2013-2014.

[27] M. Al-Obaidi and C.-S. Moo. 'Altitude effect on drag coefficient: An experimental and numerical analysis'. In: *Journal of Engineering Science and Technology (JESTEC)* (2017).

[28] Pitkin County. *Aspen/Pitkin County Airport Update – Civic Alerts*. Accessed April 20, 2025. 2024. URL: https://pitkincounty.com/CivicAlerts.aspx?AID=711&ARC=1268.

[29] Daniel P. Raymer. *Aircraft Design: A Conceptual Approach*. 5th. AIAA, 2012.

[30] Carl J. Recine et al. 'Analysis and Optimization of Baseline Single Aisle Aircraft for Future Electrified Powertrain Flight Demonstration Comparisons'. In: *Proceedings of the AIAA/IEEE Electric Aircraft Technologies Symposium (EATS)*. NASA Technical Report 20230006461. AIAA & IEEE. San Diego, CA, USA, June 2023. URL: https://ntrs.nasa.gov/api/citations/20230006461/downloads/EATS_Paper_Recine.pdf.

[31] Giovanni Recine et al. *Empirical Aircraft Thrust Models for Simulation (EATS)*. Tech. rep. NASA/TP–20230006461. NASA Ames Research Center, 2023. URL: https://ntrs.nasa.gov/api/citations/20230006461/downloads/EATS_Paper_Recine.pdf.

[32] Jan Roskam. *Airplane Design Part VI: Preliminary Calculation of Aerodynamic Thrust Forces and Moments*. DARcorporation, 1985.

[33] Jan Roskam. *Airplane Design, Part VI: Preliminary Calculation of Aerodynamic Thrust and Power Characteristics*. Lawrence, Kansas: DARcorporation, 1990.

[34] Mohammad H. Sadraey. *Aircraft Design: A Systems Engineering Approach*. 2013.

[35] Jan Henrik Schulz. *Entwicklung eines empirischen Triebwerksmodells für die Schnellabschätzung von Start- und Steigflugleistungen*. Hochschule für Angewandte Wissenschaften Hamburg. Available at https://www.fzt.haw-hamburg.de/pers/Scholz/arbeiten/TextSchulzDipl.pdf. 2007.

[36] Mark S. Selig. *Dynamic scaling of aerodynamic coefficients with altitude*. https://m-selig.ae.illinois.edu/. Accessed 2025.

[37] R. Shahid et al. 'Effect of altitude on aerodynamic drag using CFD analysis'. In: *ResearchGate* (2017). Available online.

[38] Brian L. Stevens, Frank L. Lewis and Eric N. Johnson. *Aircraft Control and Simulation: Dynamics, Controls Design, and Autonomous Systems*. 3rd. John Wiley & Sons, 2015. ISBN: 978-1118870983.

[39] Egbert Torenbeek. *Synthesis of Subsonic Airplane Design*. Kluwer Academic Publishers, 1982.

[40] U.S. Air Force. *U.S. Air Force Stability and Control DATCOM*. 1978.

[41] Gregory Vartanov. *High strength corrosion resistant steel for aircraft landing gears and structures*. Tech. rep. SAE international, 2021.

[42] Wikipedia contributors. *Alenia C-27J Spartan*. https://fr.wikipedia.org/wiki/Alenia_C-27J_Spartan. Accessed may 12, 2025.

[43] Wikipedia contributors. *ATR 72*. https://fr.wikipedia.org/wiki/ATR_72. Accessed may 12, 2025.

[44] Wikipedia contributors. *Boeing Business Jet*. https://fr.wikipedia.org/wiki/Boeing_Business_Jet. Accessed April 20, 2025.

[45] Wikipedia contributors. *Bombardier Global 7500*. https://fr.wikipedia.org/wiki/Bombardier_Global_7500. Accessed April 20, 2025.

[46] Wikipedia contributors. *Bombardier Q400*. https://fr.wikipedia.org/wiki/Bombardier_Q400. Accessed may 12, 2025.

[47] Wikipedia contributors. *Cessna CitationJet*. https://fr.wikipedia.org/wiki/Cessna_CitationJet. Accessed April 24, 2025.

[48] Wikipedia contributors. *Dassault Falcon 10X*. https://fr.wikipedia.org/wiki/Dassault_Falcon_10X. Accessed April 20, 2025.

[49] Wikipedia contributors. *Embraer Phenom 100*. https://fr.wikipedia.org/wiki/Embraer_Phenom_100. Accessed April 20, 2025.

[50] Wikipedia contributors. *Gulfstream G650/G700/G800*. https://en.wikipedia.org/wiki/Gulfstream_G650/G700/G800. Accessed April 20, 2025.

[51] Wikipedia contributors. *Mexico City International Airport*. https://en.wikipedia.org/wiki/Mexico_City_International_Airport. Accessed April 24, 2025.

[52] Wikipedia contributors. *Napa County Airport*. https://en.wikipedia.org/wiki/Napa_County_Airport. Accessed April 24, 2025.

[53] Good Year. *Aircraft tire Engineering Data*. Tech. rep. GoodYear.